Optical Control over Nuclear Spins

by

Haowei Xu

B.S., Physics, Peking University (2017)

Submitted to the Department of Nuclear Science and Engineering
in partial fulfillment of the requirements for the degree of

Doctor of Philosophy in Quantum Science and Engineering

at the

MASSACHUSETTS INSTITUTE OF TECHNOLOGY

February 2023

Author .....
Department of Nuclear Science and Engineering
December 1, 2022

Certified by .....
Ju Li
Battelle Energy Alliance Professor of Nuclear Science and Engineering
Professor of Materials Science and Engineering
Thesis Supervisor

Certified by .....
Mingda Li
MIT Class of 1947 Career Development Professor
Assistant Professor of Nuclear Science and Engineering
Thesis Reader

Accepted by .....
Ju Li
Battelle Energy Alliance Professor of Nuclear Science and Engineering
Professor of Materials Science and Engineering
Chair, Department Committee on Graduate Students

Optical Control over Nuclear Spins

by

Haowei Xu

Submitted to the Department of Nuclear Science and Engineering
on December 1, 2022, in partial fulfillment of the
requirements for the degree of
Doctor of Philosophy in Quantum Science and Engineering

Abstract

The blossom of quantum information science and technology in the past decades is facilitated by the development of various qubit platforms. A qubit system that simultaneously has long coherence time, fast operation, and large scalability is highly desirable. Particularly, nuclear spins have been considered as ideal quantum information carriers thanks to their exceptionally long coherence time exceeding minutes and even hours at room temperature. However, the application of nuclear spins is hindered by their small energy scales and weak interactions with external fields.

Light-matter interaction has attracted intense interest in recent years. The development in both classical and quantum optics provide unprecedented opportunities in the applications of optical approaches. In condensed matter physics/materials science, optical approaches provide great flexibility in characterizing material properties, driving excitations, and even triggering phase transitions in materials. Meanwhile, light-matter interactions are widely used in quantum science. For example, the spontaneous parametric down-conversion can be applied to create entangled photon pairs. If nuclear spins can be manipulated with optical approaches, then it would facilitate a number of potential applications.

However, an efficient interface between nuclear spins and optical approaches is still lacking and is in particular hindered by the formidable gap between nuclear spin frequencies ($10^3 \sim 10^6$ Hz) and optical frequencies ($\sim 10^{15}$ Hz). Previous works on optical control over nuclear spins rely on ancillary electron spins. In this thesis, we propose an opto-nuclear quadrupolar (ONQ) effect, whereby two-color optical photons can coherently couple with nuclear spins without the need for ancillary electron spins. Hence, several limitations due to the presence of the electron spins, such as shortened nuclear spin coherence time, can be eased. Besides, the frequencies of the optical lasers can be arbitrary in practice, so they can be fine-tuned to minimize the material heating effect and to match telecom wavelengths for long-distance communications.

Following the introduction to the mechanism, we suggest several applications of the ONQ effect. We will focus on the applications in quantum technologies, including using nuclear spins as the quantum memory to store the quantum information carried by optical photons, as the quantum transducer between microwave/radio frequency

and optical photons. We will also discuss how laser cooling of nuclear spin excitations can be realized via the ONQ effect.

Thesis Advisor: Ju Li
Title: Battelle Energy Alliance Professor of Nuclear Science and Engineering
Professor of Materials Science and Engineering

Thesis Reader: Mingda Li
Title: MIT Class of 1947 Career Development Professor
Assistant Professor of Nuclear Science and Engineering

Acknowledgments

Five years is a short time. I vividly remember when I met Prof. Ju Li for the second time, he gave me a problem to work on. I felt I did not have enough background knowledge to solve that problem and I expressed my hesitance, but Prof. Li told me: "Haowei, doing research is different from preparing for exams. The answers to all the questions in the exam can be found in textbooks, so you need to grasp all the knowledge before taking the exam. But for doing research, no one knows the answer, and sometimes no one knows what tools are needed for solving the problem, so you can start working on it with little background knowledge." These words truly inspired me. Gradually I also realized that working on a field that is new to me often leads to new ideas and inspirations in an old field that I have been working on, and I am always trying to find new problems beyond my current knowledge.

I would like to express my deepest gratitude to Prof. Li for his guidance and support during my whole Ph.D. study. His revolutionary ideas and endless passion for research in many different fields impressed me from the first day I worked with him. He always immediately provides profound insights to approach a problem when I discuss with him. He is also very encouraging and willing to listen and help.

I would like to sincerely thank Prof. Paola Cappellaro. She is more than a co-advisor of mine and this thesis would not have been possible without her close and constructive guidance. Her spirit to get to the bottom of every detail of a problem has encouraged me to be more meticulous in doing research.

I would like to express my gratitude to all the professors who have given me guidance and support, Prof. Mingda Li, Prof. Dirk Englund, Prof. Rafael Jaramillo, Prof. Jing Kong, and many others. What MIT impresses me the most is that all the professors are always helpful despite their tight schedules.

I had the pleasure of working with many group members. In particular, Dr. Jian Zhou taught me a lot on condensed matter physics and density functional theory calculations at the very beginning of my Ph.D., and we have been working together on many projects since then. Special thanks to Dr. Hua Wang, we have been working

together on various aspects of the nonlinear optical responses of electronic systems. I would like to extend my sincere thanks to Changhao Li and Guoqing Wang from Paola's group. We have been working closely on the optical control over nuclear spins and many other problems, which form an essential part of this thesis. Many thanks to Jiaojian Shi as an long-time experimental collaborator, his experimental skills on nonlinear optics always surprise me. Thanks should also go to many other group members and collaborators during my Ph.D. study.

Finally, I would like to thank my family. My parents are always supportive to me and give me the freedom to make every choice and decision in my life. Words cannot express my gratitude to Meihui Liu for her limitless encouragement and love in both good and hard times.

Contents

List of Figures

List of Tables

Chapter 1

Introduction

1.1 Nuclear Spins

The sophisticated manipulation of *electron charges* leads to the well-celebrated electronics [1], which has revolutionized the human civilization during the past century. The manipulation of *electron spins* leads to a plethora of applications in many fields ranging from spintronics and condensed matter physics to quantum information science and technology. Similar to electron charge and electron spin, *nuclear spin* is another fundamental quantum object in nature. However, the control over nuclear spins, while used in a few applications such as nuclear magnetic resonance (NMR), has been less developed and less influential. Moreover, nuclear spins are considered as sources of noises in many scenarios [2].

A major issue that hinders the application of nuclear spins is their small energy scale and weak interaction with the environment. The interactions involving electron charges and spins can easily exceed 1 eV and 1 meV, respectively. In contrast, in most situations the interactions involving nuclear spins are well-below 1 μeV $\approx$ 240 MHz. For example, the nuclear Zeeman interaction is only around 10 MHz when a nuclear spin is under a 1 T magnetic field. Also, the magnetic dipole interaction between two nuclear spins is only on the order of kHz even if they are as close as 1 Å.

Furthermore, for decades nuclear spins are usually controlled with magnetic fields, which are relatively hard to modulate. This hampers the application of nuclear spins

as well. The generation of strong magnetic fields usually requires bulky coils; The response time of strong magnetic fields is usually long (e.g. ms), leading to low temporal resolution; Besides, magnetic fields are hard to focus, resulting in low spatial resolution.

In many scenarios, electron spins are not controlled with magnetic fields, but instead with electric or optical fields [3, 4], which directly interact with the electron charge degree-of-freedom through electric dipole interaction. Then, certain mechanisms such as spin-orbit interaction ($\sim$ 10 meV) [5–7] can transmit the interaction from charge to spin degrees-of-freedom, and thus electric/optical fields can indirectly control electron spins. In the case of nuclear spin, an efficient electrical/optical interface is still lacking. While nuclei also have charge, which could potentially mediate the interaction between electric/optical fields and nuclear spins [1], the relevant energy scale ($\sim$ MeV) is too high for most practical applications.

In this era when quantum information science is blossoming, nuclear spins could be an ideal quantum information carrier, thanks to their exceptionally long decoherence time exceeding minutes or even hours at room temperature [8, 9]. It is thus highly desirable to have more sophisticated control over nuclear spins.

1.2 Optical Approaches

Since the advent of lasers in the 1960's [10], optical approaches have seen great success. Optical approaches usually have both high temporal resolution (on or below the order of fs [11]) and high spatial resolutions (hundreds of nm, only limited by the diffraction limit [12]). Optical laser can also be ultra-strong and non-contact, which provides additional flexibility. Thanks to these advantages, optical approaches find wide applications in many scientific and technological disciplines. For example, second-harmonics generation spectroscopy has been providing detailed information on the ionic and electronic structure of molecules and solid-state systems since the

[1] The spin-orbit interaction in nuclei is strong ($\sim$ MeV). It is actually an important ingredient in shell model and helps explain the magic number of nucleons.

very beginning of laser technology [13].

The fields of both classical and quantum optics are continuously evolving in recent years. The development in photonics design [14, 15] leads to unprecedented control over optical photons down to the single-photon level and ever-increasing interaction strength between light and matter. For quantum information science and technology, optical approaches also play crucial roles. In linear optics quantum computation [16, 17], photons are the fundamental building block of the qubit platform. In other qubit systems such as semiconductor defects [2, 18], trapped ions [19], and Rydberg atoms [20,21], optical approaches are used to initialize, manipulate, and/or readout as well. In condensed matter physics, various nonlinear optical (NLO) effects and their inherent relationship with crystalline structures, magnetic structures and particularly, electronic band topologies have attracted wide interest. For example, some NLO effects are closely connected to certain topological properties [22–25]. Meanwhile, the NLO responses can be enhanced in topological materials [26–28], thus topological materials can be efficient platforms of some applications such as photodetection in infrared to terahertz range.

1.3 Overview of The Thesis

In this thesis, we will discuss how optical approaches can be used to control nuclear spins. We will first introduce an opto-nuclear quadrupolar (ONQ) effect, which is a second-order NLO effect and could couple two-color optical photons and nuclear spins. We elucidate the mechanism and estimate the strength of the ONQ effect. Then we will discuss potential applications of the ONQ effect, ranging from material spectroscopy, to quantum technologies (quantum memory, quantum transduction, etc.), to the laser cooling of nuclear magnons. Along with the ONQ effect, we will also discuss the nuclear electric resonance (NER) [29–31], which can be considered as the linear version of the ONQ effect and enables the interaction between microwave electric fields and nuclear spins. An overview of this thesis is as follows:

- In Chapter 2, we introduce the nuclear spin Hamiltonian.

- In Chapter 3, we discuss how electron spins have been used to control nuclear spins via the hyperfine interaction.
- In Chapter 4, we explain the mechanism of the NER and the ONQ effect. We also estimate their interaction strength.
- In Chapter 5, we compare the NER and ONQ effects with other linear and nonlinear optical effects that could couple electric/optical fields with nuclear spins.
- In Chapter 6, we discuss potential applications of the NER effect.
- In Chapter 7, we demonstrate potential applications of the ONQ effect.
- In Chapter 8, we will discuss some miscellaneous topics relevant to the optical control over nuclear spins.

This thesis is based on two manuscripts in submission:

- Haowei Xu, Changhao Li, Guoqing Wang, Hua Wang, Hao Tang, Ariel Rebekah Barr, Paola Cappellaro, and Ju Li. Two-photon Interface of Nuclear Spins Based on the Opto-nuclear Quadrupolar Effect. *Physical Review X*, under revision.
- Haowei Xu, Guoqing Wang, Changhao Li, Hua Wang, Hao Tang, Ariel Rebekah Barr, Paola Cappellaro, and Ju Li. Laser Cooling of Nuclear Magnons. *Physical Review Letters*, under review.

Chapter 2

Nuclear Spin Hamiltonian

In this chapter, we introduce different types of interactions that nuclear spins participate in, which would be the foundations of the discussions in following chapters.

We first focus on the single nuclear spin Hamiltonian, which can be expressed as

$$\begin{aligned} H_N &= H_{\mathrm{Z}} + H_{\mathrm{hf}} + H_{\mathrm{Q}} \\ &= \gamma_N \sum_i \mathscr{B}_i I_i + \sum_{ij} A_{ij} S_i I_j + \sum_{ij} Q_{ij} I_i I_j. \end{aligned} \tag{2.1}$$

Here I (S) is the angular momentum operator of the nuclear (electron) spin, with $i = x, y, z$ the Cartesian indices. The three terms are the nuclear Zeeman interaction H_{Z}, the hyperfine interaction H_{hf}, and the nuclear quadrupole interaction H_{Q}, respectively.

2.1 Nuclear Zeeman Interaction

The first term in Eq. (2.1), H_{Z}, is the Zeeman interaction between nuclear spin and external magnetic field $\mathscr{B}$. γ_N is the gyromagnetic ratio of the nucleus under consideration. The origin of the H_{Z} is that the nucleus has a magnetic dipole $\boldsymbol{m}_N = g_N \mu_N$, where g_N is the g-factor and is usually on the order of 1. μ_N is the nuclear magneton,

$$\mu_N = \frac{e\hbar}{2m_p}, \tag{2.2}$$

where e is the electron charge, $\hbar$ is the Planck constant[1], while m_p is the mass of proton. One can see that

$$\gamma_N \equiv \frac{\boldsymbol{m}_N}{\hbar} \sim 10 \times \frac{2\pi \cdot \mathrm{MHz}}{\mathrm{T}}, \tag{2.3}$$

that is, the nuclear Zeeman interaction strength is on the order of 10 MHz when the external magnetic field is 1 T. This is significantly weaker than the strength of the Zeeman interaction of electron spin, which is around $10 \times \frac{2\pi \cdot \mathrm{GHz}}{\mathrm{T}}$.

The well-known nuclear magnetic resonance (NMR) technology relies on the nuclear Zeeman interaction H_Z - a DC magnetic field leads to the Zeeman splitting and Larmor precession, while an AC field drives the Rabi oscillation between different nuclear spin states. Notably, the weak nuclear Zeeman interaction [Eq. (2.3)] makes the manipulations of nuclear spins challenging. For example, for a typical nuclear spin under 1 T magnetic field, a 99 % fidelity of initialization to the ground state (using thermal cooling) requires a demanding temperature below 0.1 mK. Besides, a strong AC magnetic field of 0.1 T only leads to a Rabi frequency of 1 MHz, which is rather slow compared with e.g., electron spin or orbital transitions.

2.2 Hyperfine Interaction

The second term in Eq. (2.1), H_hf, is the hyperfine interaction between nuclear spins I and electron spin S, with A_{ij} the hyperfine tensor. Basically, the hyperfine interaction is the dipole-dipole interaction between the magnetic moments of the nucleus and the electron. The nucleus, which has a dimension on the order of femtometer, can be safely treated as a point localized at R_I. In comparison, the electron has relatively delocalized wavefunction $|\psi(r)\rangle$. For clarity, we assume the electron spin to be along z direction, and the distribution of the electron magnetic moment is determined by the spin density $\rho_S(r) \equiv \langle\psi(r)|S_z|\psi(r)\rangle$. The hyperfine interaction has two

[1]We will occasionally set $\hbar = 1$ hereafter

contributions [32]. The Fermi contact term is

$$[A_{\text{iso}}]_{ij} = \frac{2\mu_0}{3}\frac{\gamma_e\gamma_N}{\langle S_z\rangle}\delta_{ij}\int \delta(r)\rho_S(r+R_I)\mathrm{d}r. \tag{2.4}$$

And the dipolar term is

$$[A_{\text{ani}}]_{ij} = \frac{\mu_0}{4\pi}\frac{\gamma_e\gamma_N}{\langle S_z\rangle}\int \frac{\rho_S(r+R_I)}{r^3}\frac{3r_ir_j-\delta_{ij}r^2}{r^2}\mathrm{d}r. \tag{2.5}$$

Here γ_e is the electron gyromagnetic ratio, and μ_0 is the vacuum permeability. δ_{ij} is the Kronecker delta, while $\delta(r)$ is the delta function. One can see that $[A_{\text{iso}}]_{ij}$ is an isotropic tensor, while $[A_{\text{ani}}]_{ij}$ is anisotropic. $\langle S_z\rangle$ is the expectation value of S_z, and is used to normalize the hyperfine tensor.

To demonstrate the strength of the hyperfine interaction, here we roughly estimate the magnitude of A_{iso}. If an s-orbital electron is centered on the nuclear site , then one has $\rho_S(r=R_I) = C(\frac{Z}{a_0})^3$, where a_0 is the Bohr radius, Z is the atomic number of the nucleus. C is a constant dependent on the principle quantum number, and is typically on the order of $10^{-3}\sim 10^{-2}$ [5]. Then, one has

$$\begin{aligned} A_{\text{iso}} &= C\frac{2\mu_0}{3}\frac{\gamma_e\gamma_N}{\langle S_z\rangle}\left(\frac{Z}{a_0}\right)^3 \\ &\sim CZ^3\times 400\ \text{MHz}. \end{aligned} \tag{2.6}$$

One can see that A_{iso} can reach 1 GHz and above. In practice, usually the electron is not fully of s-orbital characteristics or not fully centered on the nuclear site, so A_{iso} could be smaller than the hand-waving estimation in Eq. (2.6). However, an A_{iso} on the order of hundreds of MHz is not rare, which is equivalent to an effective magnetic field of

$$\mathscr{B}^{\text{eff}} = \frac{A_{\text{iso}}}{\gamma_N} \approx [10\sim 100]\ \text{T}. \tag{2.7}$$

One can see that the hyperfine interaction can be a strong interaction for nuclear spins.

2.3 Nuclear Quadrupole Interaction

The third term in Eq. (2.1), H_{Q}, is the nuclear quadrupole interaction, with Q_{ij} the quadrupole tensor. The charge distribution in certain nuclei is not fully isotropic (not fully spherical). In the spirit of multipolar expansion [33], the dipole moments of nuclear charge are always zero, whereas the quadrupole moment $\mathscr{q}$ of some nuclei can be nonzero. When the nucleus resides in an electric field gradient (EFG) $\mathscr{V}_{ij}$, there would be a nuclear quadrupole interaction. Notably, the charge distribution of the nucleus is closely related to its angular momentum[2], and the quadrupole tensor can be expressed as [34, 35]

$$Q_{ij} = \frac{e\mathscr{q}\mathscr{V}_{ij}}{2I(2I-1)}, \tag{2.8}$$

and the EFG tensor is

$$\mathscr{V}_{ij} = \lim_{r \to R_I} \left(\partial_i \partial_j - \frac{1}{3}\delta_{ij}\nabla^2 \right) v(r), \tag{2.9}$$

where $v(r)$ is the electric potential at r. Note that the $\mathscr{V}_{ij}$ tensor is traceless by definition.

The magnitude of the quadrupole interaction is mainly determined by two factors: (1) the quadrupole moment $\mathscr{q}$ of the nucleus under consideration. $\mathscr{q}$ is typically on the order of $10 \sim 10^3$ mb [3]. Usually heavy nuclei have stronger anisotropy and hence larger $\mathscr{q}$; (2) the magnitude of the EFG tensor $\mathscr{V}$, which would be larger if the environment is highly anisotropic. Note that both $\mathscr{q}$ and $\mathscr{V}$ could be zero if the nucleus or the environment is highly isotropic with a e.g., tetrahedral symmetry [33, 36].

In solid-states or molecular systems, the intrinsic EFG $\mathscr{V}^{(0)}$ comes from the electric potential generated by surrounding electrons. The typical magnitude of such an electric potential is on the order of $\phi \sim 1$ V [4], while the typical length scale (i.e.,

[2] Recall that both the charge distribution and the angular momentum can be described by spherical harmonics.

[3] $1\ \mathrm{mb} = 10^{-31}\ \mathrm{m}^{-3}$

[4] Recall that the ionization energy hydrogen atoms is 13.6 eV.

wavelength) is on the order of $\lambda \sim 1$ Å [5]. Hence, one has

$$\mathscr{V}^{(0)} \sim \frac{\phi}{\lambda^2} \sim 1 \text{ V/Å}^2. \tag{2.10}$$

As we will show in Section 4.4, even larger $\mathscr{V}^{(0)} \sim 10$ V/Å^2 can be achievable.

2.4 Nuclear Spin-Spin Interaction

In previous sections, we discussed the single nuclear spin Hamiltonian. Nuclear spins could also interact with nearby nuclear spins, which can be expressed as

$$\mathscr{H}_{\text{nn}} = \sum_{\alpha\beta} I^\alpha \cdot \mathscr{J}^{\alpha\beta} \cdot I^\beta, \tag{2.11}$$

where the superscripts α, β are indices of the nuclear spins, and $\mathscr{J}^{\alpha\beta}$ describes the interaction between nearby nuclear spins. The summations over Cartesian indices are implied by the dot product. A major contribution to $\mathscr{J}^{\alpha\beta}$ is the dipole-dipole interaction between the magnetic moments of nuclei, which is

$$\mathscr{J}^{\alpha\beta} = -\frac{\mu_0 \gamma_\alpha \gamma_\beta}{4\pi r^3} \left[3(I^\alpha \cdot \hat{r})(I^\beta \cdot \hat{r}) - I^\alpha \cdot I^\beta\right], \tag{2.12}$$

where γ_α and γ_β are the gyromagnetic ratio of the two nuclei, respectively. r is the distance between the two nuclei, while $\hat{r}$ is the unit vector that connect the two nuclei. For typical nuclear spins, $\gamma_{\alpha(\beta)}$ is on the order of $10 \times \frac{2\pi \cdot \text{MHz}}{\text{T}}$, and the distance between nearest nuclear spins can be on the order of of 1 Å. This leads to

$$\mathscr{J}^{\alpha\beta} \sim 1 \text{ kHz}. \tag{2.13}$$

Note that besides the dipole-dipole interaction above, the nuclear spin-spin interaction could also result from e.g., the Ruderman–Kittel–Kasuya–Yosida (RKKY) interaction [37–40], which is mediated by conduction electrons in metals. Recently,

[5] Recall that the Bohr radius is 0.53 Å.

there are also recent proposals to modulate the nuclear spin-spin interaction via e.g., optical illumination [41, 42].

Chapter 3

Control over Nuclear Spins via Hyperfine Interaction

As discussed in Section 2.1, the control over nuclear spins is challenging, because the interaction between nuclear spins and the environment is rather weak. Traditional NMR technologies, while highly developed, suffer from several intrinsic limitations. For example, bulky coils are required to generate magnetic field on the order of Tesla; The Response time of magnetic field is usually long, so the temporal resolution is usually low; The microwave (MW) or radio frequency (RF) magnetic fields used to drive Rabi oscillations have long wavelength, and it is hard to focus magnetic fields, so high spatial resolution is difficult to achieve.

In recent years, novel approaches for controlling nuclear spins, especially single nuclear spin, are keenly explored. Besides a few works that utilize the nuclear quadrupole interaction, which can be modulated by electric field [29–31, 43] or phonons/mechanical waves [44,45], a number of works utilize the hyperfine interaction - If one changes the state of electron spins with external fields, then the hyperfine interaction can be modified accordingly, which can be used to manipulate the nuclear spins [46–57]. In this chapter, we discuss some typical mechanism/experiments that use hyperfine interaction to manipulate nuclear spins. We will also discuss some limitations of using hyperfine interaction to control nuclear spins.

3.1 Resonance Exchange between Nuclear and Electron Spin Polarizations

As discussed in Section 2.2, the hyperfine interaction $H_{\rm hf} = \sum_{ij} A_{ij} S_i I_j$ can be considered as an effective magnetic field $\mathscr{B}_i^{\rm eff} = \sum_i A_{ij} S_i$ acting on nuclear spin I_j, which could drive the Rabi oscillation of nuclear spins when either A or S_i is oscillating with a frequency resonant with nuclear spin transitions. An equivalent way to understanding this effect is that electron and nuclear spins can exchange polarizations, thanks to the hyperfine interaction. As an example, let's consider an $S = \frac{1}{2}$ electron spin and an $I = \frac{1}{2}$ nuclear spin, which can be described by $|m_S m_I\rangle$, where $m_S\,(m_I) = \uparrow, \downarrow$ denote the electron (nuclear) spin quantum number. Notably, if $|\uparrow\downarrow\rangle$ and $|\downarrow\uparrow\rangle$ are degenerate in energy, then the system can spontaneously transit between $|\uparrow\downarrow\rangle$ and $|\downarrow\uparrow\rangle$. In this case, if by certain control, the electron spin is preferably in $|\uparrow\rangle$ state, then the $|\uparrow\downarrow\rangle \rightarrow |\downarrow\uparrow\rangle$ transition would dominate the reverse $|\downarrow\uparrow\rangle \rightarrow |\uparrow\downarrow\rangle$ transition. Consequently, the nuclear spin would also be preferably in the $|\uparrow\rangle$ state, due to the hyperfine interaction with the electron spin.

One can see that resonance, or in other words, energy conservation, is a key condition for effective exchange between electron and nuclear spin polarization. Resonance can be achieved when two different states are intrinsically degenerate in energy, as in the case of the example above. Otherwise, the energy difference between the two states should be provided externally by e.g, a microwave magnetic field. In the following, we will discuss different approaches for realizing resonance.

3.1.1 Resonance in Rotating+Rotating Frame

A straightforward way for achieving resonance is to make the nuclear and electron spin have the same energy splitting. However, under the same static magnetic field $\mathscr{B}^0$, the energy splitting of nuclear spin in the laboratory frame $\Delta_I^{\rm lab} = \gamma_N \mathscr{B}^0$ is significantly smaller than that of electron spin $\Delta_S^{\rm lab} = \gamma_e \mathscr{B}^0$ by three orders of magnitude, as discussed in Section 2.1. To address this issue, Hartmann and Hahn proposed [58]

that one can apply two oscillating magnetic field $\mathscr{B}^{I,\text{osci}}$ and $\mathscr{B}^{S,\text{osci}}$, whose frequencies are on resonance with Δ_I^{lab} and Δ_S^{lab}, respectively. Then in the spirit of rotating frame approximation, the energy splitting of nuclear and electron spins are $\Delta_I^{\text{rot}} = \gamma_N \mathscr{B}^{I,\text{osci}}$ and $\Delta_S^{\text{rot}} = \gamma_e \mathscr{B}^{S,\text{osci}}$ in the rotating frame, respectively. By tuning the magnitude of $\mathscr{B}^{I,\text{osci}}$ and $\mathscr{B}^{S,\text{osci}}$, it is possible to achievement the resonance in the rotating frame ($\Delta_I^{\text{rot}} = \Delta_S^{\text{rot}}$), and the polarization of the electron and nuclear spins can be effectively exchanged. This is the so-called Hartmann Hahn (HH) double resonance.

3.1.2 Resonance in Rotating+Laboratory Frame

Besides HH double resonance, a closely related strategy to achieve resonance is to apply one oscillating magnetic field $\mathscr{B}^{S,\text{osci}}$ to drive only the electron Rabi oscillation. By tuning $\mathscr{B}^{S,\text{osci}}$, one can realize the resonance between electron spin splitting in the rotating frame and the nuclear spin splitting in laboratory frame ($\Delta_I^{\text{lab}} = \Delta_S^{\text{rot}}$). This strategy, so called Nuclear spin orientation via electron spin locking (NOVEL), has been widely studied in e.g. Refs. [51, 59–61]. Here we take $S = \frac{1}{2}$ and $I = \frac{1}{2}$ as an example to illustrate the mechanism of the NOVEL scheme. We assume that the $\mathscr{B}^0$ is along z direction, while $\mathscr{B}^{S,\text{osci}}$ is along x direction. In the rotating frame, the electron eigenstates are $|\pm\rangle_S = \frac{1}{\sqrt{2}}(|\uparrow\rangle_S \pm |\downarrow\rangle_S)$. The energy difference between $|+\rangle_S$ and $|-\rangle_S$ is $\Delta_S^{\text{rot}} = \gamma_e \mathscr{B}^{S,\text{osci}}$. If Δ_S^{rot} matches $\Delta_I^{\text{lab}} = \gamma_N \mathscr{B}^0$, then it is possible that electron spin oscillates between $|+\rangle_S$ and $|-\rangle_S$, while nuclear spin oscillates between $|\uparrow\rangle_I$ and $|\downarrow\rangle_I$. The nuclear spin oscillation frequency is proportional to the magnitude of the hyperfine tensor A. This process is illustrate in Figure 3-1.

Notably, the NOVEL scheme requires the hyperfine tensor A to be anisotropic. Besides, Δ_I^{lab} needs to be comparable with, or preferably larger than A, so that the hyperfine interaction would not over-influence the properties/dynamics of the nuclear spin [1]. This limits the Rabi frequency of the nuclear spin oscillation, which is proportional to A, since Δ_I^{lab} usually cannot exceed tens of MHz in experiments. Some detailed analysis on the NOVEL scheme can be found in Ref. [51].

[1] Note that the hyperfine interaction is time-dependent when the electron spin is oscillating in time

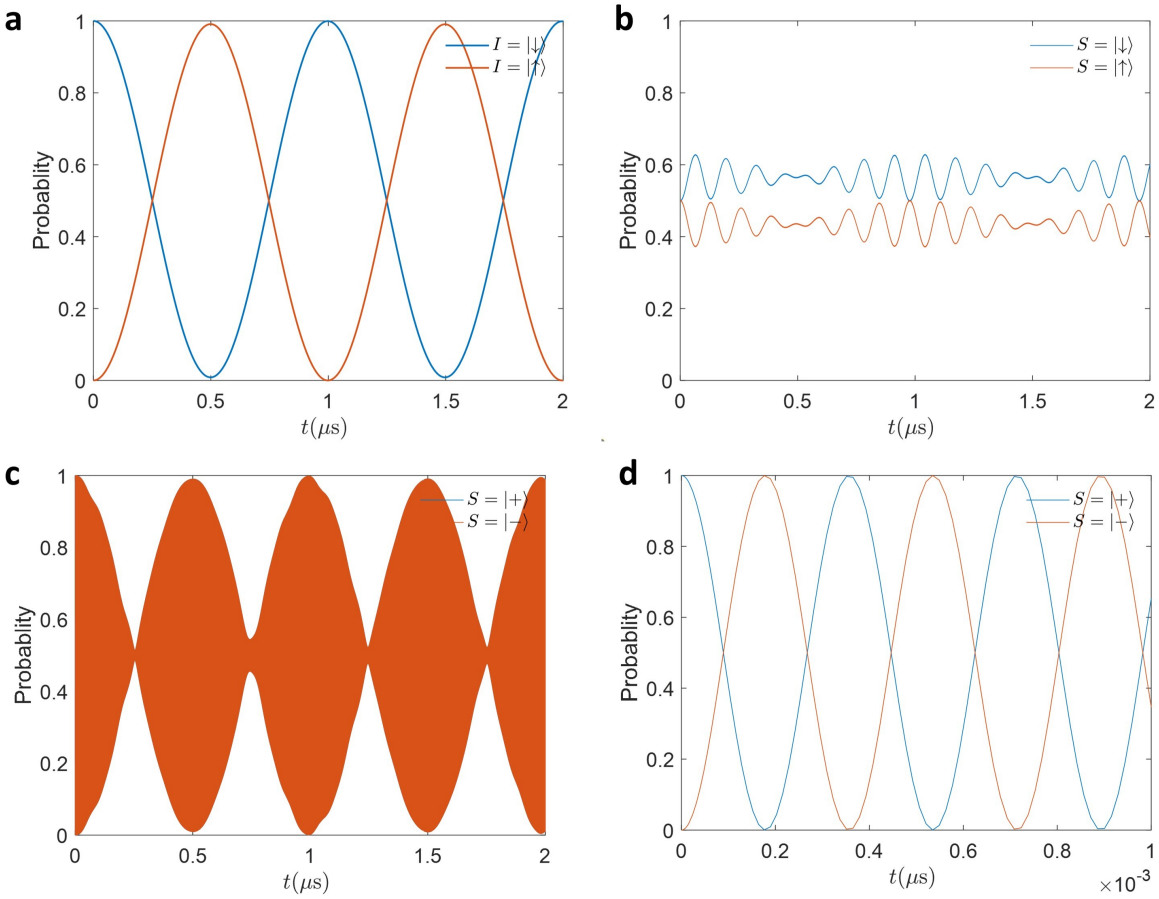

Figure 3-1: Numerical Simulation of the NOVEL scheme. (a) Time evolution of the nuclear spin polarization I. (b) Time evolution of the electron spin polarization in the basis of $|\uparrow\rangle$ and $|\downarrow\rangle$. (c) Same as (b), but in the basis of $|\pm\rangle$. (d) Same as (c), but zoomed in along x-axis to show the Rabi oscillation between $|\pm\rangle$. Here $S = \frac{1}{2}$, $I = \frac{1}{2}$. The external static magnetic field is $\mathscr{B}^0 \sim 0.1$ T. The hyperfine tensor is $A = [[2, 0, 2]; [0, 4, 0]; [2, 0, 2]] \times 2\pi \cdot$ MHz.

Table 3.1: Different schemes for achieving resonance between nuclear and electron spins.

Frame	Frequency Matching Condition	Specification
Rotating + Rotating	$\gamma_e \mathscr{B}^{S,\text{osci}} = \gamma_N \mathscr{B}^{I,\text{osci}}$	HH double resonance [58]
Rotating + Laboratory	$\gamma_e \mathscr{B}^{S,\text{osci}} = \gamma_N \mathscr{B}^{0}$	NOVEL [59]
Laboratory + Laboratory	$\gamma_e \mathscr{B}^{0} = \Delta_I^{\text{quad}}$	This work

3.1.3 Resonance in Laboratory+Laboratory Frame

Finally, the resonance between nuclear and electron spins in the laboratory frame can be achieved if the nuclear quadrupole interaction (Section 2.3) is considered. The nuclear spin splitting due to nuclear quadrupole interaction Δ_I^{quad} can reach hundreds of MHz to GHz in certain systems, which can match $\Delta_S^{\text{lab}} = \gamma_e \mathscr{B}^0$ by tuning $\mathscr{B}^0$. Compared with the Hartmann-Hahn double resonance and the NOVEL scheme, such a resonance in the laboratory frame has several advantages. For example, one does not need two oscillating magnetic fields, and one does not need anisotropic A.

In summary, efficient change between electron and nuclear spin polarizations can be realized, provided with the resonance between electron and nuclear spin splitting in either laboratory or rotating frames. This can be used to control nuclear spins via the mediation of electron spins. Three possibilities for achieving resonances are listed in Table 3.1.

3.2 Optical Control over Nuclear Spins via Hyperfine Interaction

Using electron spin as the media, optical photons can be indirectly coupled to nuclear spins (Figure 3-2). Indeed, optical photons can directly couple to electron orbital

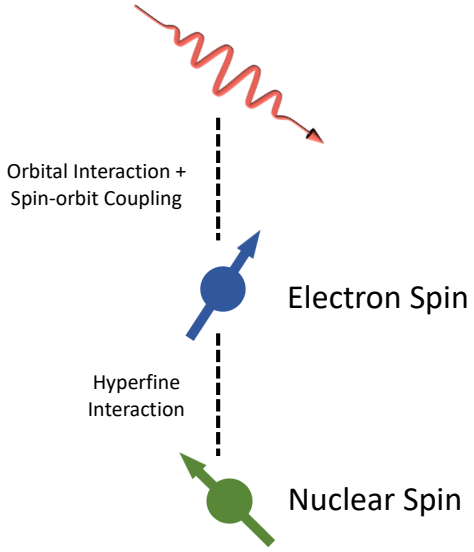

Figure 3-2: Illustration of the optical control over nuclear spins via hyperfine interaction. Optical photons modify the electron spin states via orbital dipole interaction, while the electron spin modifies the nuclear spin states via the hyperfine interaction.

dynamics via the electric dipole interaction. Then the electron spin dynamics can be influenced as well due to e.g., spin-orbit coupling. Finally, the electron spin controls the nuclear spin via the hyperfine interaction. Such optical control over nuclear spins has been demonstrated by several groups [52–57]. Here we briefly discuss the mechanisms of two typical experiments.

3.2.1 Dynamic Polarization

The dynamic polarization of single nuclear spins in the nitrogen vacancy (NV) center by optical pumping was demonstrated in Ref. [52]. The ^{15}N nuclei has $I = \frac{1}{2}$, and the eigenstates are denoted as $\{|\downarrow\rangle, |\uparrow\rangle\}$. The NV center has electron spin $S = 1$. Due to the zero field splitting (ZFS) [62], the electron spin eigenstates $\{|0\rangle, |+1\rangle, |-1\rangle\}$ are along the [111] crystal axis of the diamond (the NV symmetry axis). The $|-1\rangle$ state can be tuned off-resonance by an external magnetic field, and thus one can focus on the $\{|0\rangle, |+1\rangle\}$ subspace. The electron orbital ground and excited states are denoted as ^3A and ^3E, respectively. Notably, the ZFS for ^3A and ^3E are different. Therefore, if one applies a magnetic field $\mathscr{B}^0$ with proper magnitude along the NV

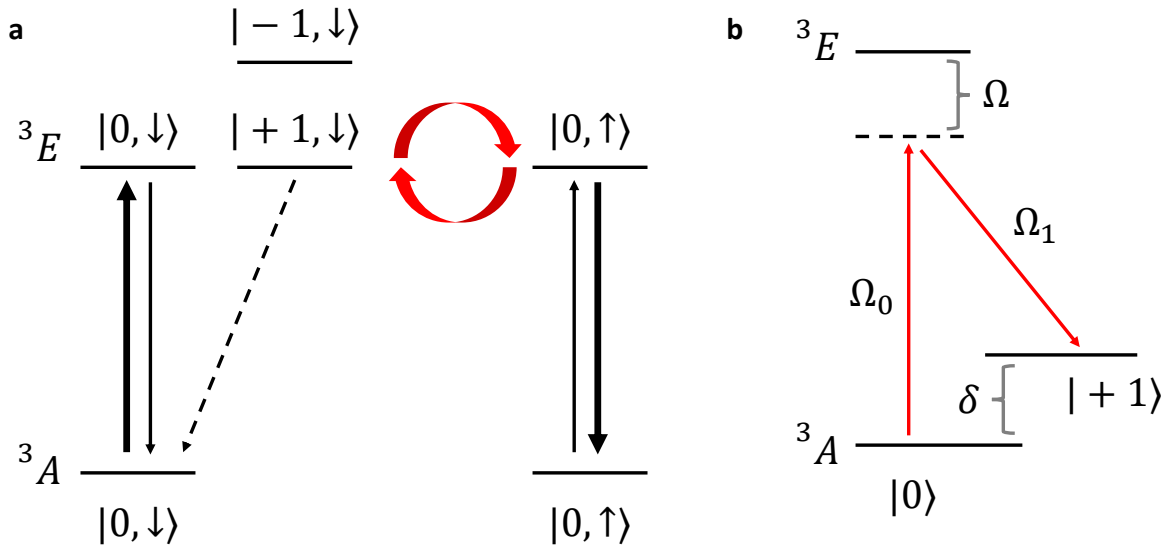

Figure 3-3: Two exemplary experiments on the optical control over nuclear spins via hyperfine interaction. (a) Dynamical polarization of single nuclear spin, adapted from Ref. [52]. (b) Optical control over nuclear spin via Raman scattering, adapted from Ref. [53].

symmetry axis, then the degeneracy between $|0\rangle$ and $|+1\rangle$ states can be achieved for either ^3A or ^3E, which are called ground or excited state level anticrossing (LAC). In Ref. [52], the excited state LAC is harnessed. Specifically, if one applies a magnetic field $\mathscr{B}^0 \approx 500$ G along the NV symmetry axis, then the electron spin eigenstates for ^3E become $|\pm\rangle \equiv \frac{1}{\sqrt{2}}(|0\rangle \pm |+1\rangle)$, while those for ^3A are still $\{|0\rangle, |+1\rangle\}$.

The simplified mechanism of the dynamical polarization of nuclear spins is illustrated in Figure 3-3(a). We assume that the nuclear spin is initially in $|\downarrow\rangle$ state, and the goal is to induce the $|\downarrow\rangle \rightarrow |\uparrow\rangle$ transition. By optically initializing the electron spins, one has the initial state as $|0,\downarrow\rangle$ on ^3A. Then, one applies a optical laser resonant with the $^3A \rightarrow {}^3E$ transition. Since optical transitions conserve spin polarization (angular momentum), one has $|0,\downarrow\rangle$ on ^3E after the optical excitation. However, due to excited state LAC, $|0\rangle = \frac{1}{\sqrt{2}}(|+\rangle + |-\rangle)$ is not the eigenstate on ^3E, and the electron spin would spontaneous oscillate between $|0\rangle$ and $|+1\rangle$. During this process, the electron and nuclear spin can exchange polarization, and the nuclear spins can undergo $|\downarrow\rangle \rightarrow |\uparrow\rangle$ transition, as discussed in Section 3.1. Using this scheme, a nuclear spin polarization higher than 98% is achieved at room temperature in Ref. [52].

3.2.2 Optical Raman Transitions

The dynamic polarization of single nuclear spins described above requires the electrons to do resonant interband transitions between orbital ground and excited states. In Ref. [53], off-resonant Raman techniques are used to realize the all-optical control over single ^{14}N nuclear spin ($I = 1$) in NV center. The simplified mechanism is illustrated in Figure 3-3(b). The energy splitting between the electron spin $|0\rangle$ and $|+1\rangle$ on the orbital ground state is denoted as δ. Two-color lasers with frequencies ω_1 and ω_2 are applied. ω_1 and ω_2 are detuned from the electron orbital transitions by Ω, and thus electrons can only undergo virtual transitions between the ground state and a virtual excited state. When $|\omega_1 - \omega_2| = \delta$, the electron can start from the ground state $|0\rangle$, virtually absorb a ω_1 photon, jump to the virtual excited state with a Rabi frequency of Ω_1, emit a ω_2 photon, and finally jump back to $|+1\rangle$ with a Rabi frequency of Ω_2. The effective transition frequency of such a Raman process is $\Omega_R = \frac{\Omega_1\Omega_2}{\Omega}$. Since optical transitions conserve total angular momentum of the nuclear and electron spins, the $|0\rangle \rightarrow |+1\rangle$ transition of electron spin must be accompanied by the $|1\rangle \rightarrow |0\rangle$ or $|0\rangle \rightarrow |-1\rangle$ transition of nuclear spins. This effect was observed in Ref. [53].

3.3 Limitations of using Hyperfine Interaction

While the control over nuclear spins via the hyperfine interactions have been widely studied, it suffers from several limitations, as listed below

- It requires the existence of nearby ancillary electron spins ($S \neq 0$), which is available only in certain defect systems or magnetic materials. This approach is not applicable in e.g., pristine non-magnetic materials;

- The decoherence time of electron spins are usually much shorter than that of nuclear spins. This sets restrictions on the operation times, that is, the operation must be completed before the decoherence of electron spins;

- The existence of electron spins also shortens the nuclear spin decoherence time. This is because the noise on electron spins can be transmitted to nuclear spins via the hyperfine interaction [48];

- The strength of the hyperfine interaction decays significantly with distance. Consequently, an ancillary electron can only control a relatively small number of nuclear spins [cf. Section 7.3.2];

- The interface between electron spins and optical photons is sensitive to the environment and can be strongly influenced by material inhomogeneities, electron-phonon coupling, etc. This would limit the fidelity of entanglement between remote spins.

Therefore, it is highly desirable to have optical mechanisms that can couple optical photons and nuclear spins without the need for ancillary electron spins.

Chapter 4

Electrical and Optical Control over Nuclear Spins

From Hamiltonian engineering point of view [cf. Eq. (2.1)], the NMR technique relies on modulating the nuclear Zeeman interaction (Section 2.1), while the techniques discussed in Chapter 3 rely on modulating the hyperfine interaction (Section 2.2). Both of these two interactions have been extensively studied. In contrast, the nuclear quadrupole interaction (Section 2.3) is relatively less explored for manipulating nuclear spins. Actually, the nuclear quadrupole interaction can lead to efficient coupling between electric/optical fields and nuclear spins, as we will demonstrate in this chapter.

In this chapter, we first introduce how electric fields can perturb the electric field gradient (EFG) around the nuclear spins, and hence the nuclear quadrupole interaction. The responses of nuclear quadrupole interaction to external electric fields can be analyzed perturbatively - The first order response corresponds the so-called nuclear electric resonance (NER) [29–31], which establishes an interface between microwave electric fields and nuclear spins; The second-order response is what we call the opto-nuclear quadrupolar (ONQ) effect, which could establish an interface between optical photons and nuclear spins. Using both analytical approaches [63, 64] and density functional theory (DFT) [65, 66] calculations, we estimate the strength of the NER and ONQ responses, which will be a crucial parameter for discussions in the following

chapters.

4.1 Modulating EFG with Electric Fields

As discussed in Sec. 2.3, the nuclear quadrupole interaction originates in the interaction between the nuclear quadrupole moment $\mathscr{q}$ and the EFG at the nuclear site $\mathscr{V}$. Notably, $\mathscr{q}$ is an intrinsic property of the nucleus under consideration, and is hard to modify unless nuclear orbital transitions (nuclear reactions), whose energy scales are typically on the order of MeV or above, are triggered. On the other hand, the EFG is relatively easier to modify. Hence, it is more practical to manipulate nuclear spins by modulating the EFG.

The intrinsic EFG generated by surrounding electrons can be on the order of $\mathscr{V}^{(0)} \sim 1\ \mathrm{V/\AA}^2$ [Eq. (2.10)]. In contrast, the EFG of an external electric field is usually rather small. For example, the EFG of a plane wave is approximately

$$\mathscr{V}_{\mathrm{ext}} \sim \frac{\mathscr{E}_{\mathrm{ext}}}{\lambda} \approx 10^{-4}\ \mathrm{V/\AA}^2, \tag{4.1}$$

which is smaller than $\mathscr{V}^{(0)}$ by almost five orders of magnitude. Here the wavelength of the plane wave is take as $\lambda = 500$ nm, and the maximum electric field strengh is taken as $\mathscr{E}_{\mathrm{ext}} = 1\ \mathrm{V/\AA}$, which is extremely strong. To put it in another way, the nuclear quadrupole interaction from $\mathscr{V}_{\mathrm{ext}}$ is

$$Q_{\mathrm{ext}} = \frac{e\mathscr{q}\mathscr{V}_{\mathrm{ext}}}{2I(2I-1)} \approx 10\ \mathrm{Hz}, \tag{4.2}$$

where we have set $\mathscr{q} = 10^3$ mb and $I = \frac{3}{2}$. Obviously, even if $\mathscr{E}_{\mathrm{ext}} = 1\ \mathrm{V/\AA}$, Q_{ext} cannot effectively influence the dynamics of nuclear spins, whose energy scale is typically above kHz.

Instead of directly using the EFG $\mathscr{V}_{\mathrm{ext}}$ of an external field, one can use the external electric field $\mathscr{E}$ to drive the orbital motions of electrons, so that there is a change $\Delta\mathscr{V}$ in the EFG generated by electrons. For example, if an electron is initially in s state, then the EFG $\mathscr{V}^{(s)}$ would be zero at the nuclear site, because s orbital is fully isotropic.

Under external electric field, the electron could jump to the a p state, whereby the EFG $\mathscr{V}^{(p)}$ would become non-zero. The change in EFG $\Delta\mathscr{V} = \mathscr{V}^{(p)} - \mathscr{V}^{(s)}$ would perturb the nuclear spins.

Here we give a hand-waving estimation of $\Delta\mathscr{V}$, while more rigorous estimation can be found in following sections. The energy difference between different electronic states (e.g., s and p orbitals) is usually on the order of $E_g \sim 1$ eV. If the external electric potential difference over the atomic scale $\lambda \sim 1$ Å is comparable with E_g, then the electrons could spontaneously jump between different states. In this case, one has $\Delta\mathscr{V} \equiv \mathscr{V}^{(p)} - \mathscr{V}^{(s)} = \mathscr{V}^{(p)}$. In other words, if the external electric field is $\mathscr{E} = \frac{E_g}{\lambda} \sim 1$ V/Å, then one could have $\Delta V \sim 1$ V/Å [cf. Eq. (2.10)], which is much larger than $\mathscr{V}_{\text{ext}}$ [cf. Eq. (4.1)], as we will elaborate on below.

Formally, the EFG $\mathscr{V}$ generated by electrons is a functional of electron density matrix ρ. External electric field $\mathscr{E}$ could modify electron density distribution. This effect can be described by perturbatively expanding the density matrix as

$$\rho = \sum_{\alpha} \rho^{(\alpha)}, \tag{4.3}$$

where $\rho^{(0)}$ is the equilibrium density matrix and $\rho^{(\alpha)} \propto \mathscr{E}^{\alpha}$ is the α-th order response to external electric field. The NER and ONQ effects correspond to $\rho^{(1)}$ and $\rho^{(2)}$, respectively.

4.2 First-order Responses: Nuclear Electric Resonance

In this section, we discuss the first-order response of the nuclear quadrupole interaction under an external electric field, corresponding to the NER. The mechanism of the NER is closely related to the so-called linear quadrupole Stark effect (LQSE) [67–69]. Recently, the NER has been demonstrated experimentally as well [29, 70]. We first derive the formula for $\rho^{(1)}$ from linear response theory.

4.2.1 Linear Response Theory

The full Hamiltonian of the electronic system can be separated as

$$H = H_0 + V, \tag{4.4}$$

where H_0 is the unperturbed Hamiltonian, while V is a perturbation, from e.g. the interaction between the electric field and the electrons. If $V = 0$, one has the equilibrium density matrix as

$$\rho_0 = \frac{1}{Z} e^{-\beta H_0}, \tag{4.5}$$

where Z is the partition function. Note that $[\rho_0, H_0] = 0$. When a time-dependent V is turned on, the density matrix ρ can be obtained from the equation of motion (von Neumann equation), which can be expressed as

$$\frac{\partial \rho}{\partial t} = -\frac{i}{\hbar}[H, \rho] - \frac{\rho - \rho_0}{\tau}. \tag{4.6}$$

The last term $-\frac{\rho-\rho_0}{\tau}$ is a dissipation term, and indicates that the system tends to return to ρ_0, due to the interaction with the external heat bath.

To solve Eq. (4.6), we first use a trick similar to the transformation between the Schrodinger picture and the interaction picture. Let $\tilde{\rho}(t) = e^{\frac{t}{\tau}} e^{i\frac{H_0}{\hbar}t} \rho(t) e^{-i\frac{H_0}{\hbar}t}$, then we have

$$\begin{aligned}
\frac{\partial \tilde{\rho}}{\partial t} &= \frac{1}{\tau} e^{\frac{t}{\tau}} e^{i\frac{H_0}{\hbar}t} \rho(t) e^{-i\frac{H_0}{\hbar}t} + i\frac{H_0}{\hbar} e^{\frac{t}{\tau}} e^{i\frac{H_0}{\hbar}t} \rho(t) e^{-i\frac{H_0}{\hbar}t} \\
&\quad + e^{\frac{t}{\tau}} e^{i\frac{H_0}{\hbar}t} \frac{\partial \rho(t)}{\partial t} e^{-i\frac{H_0}{\hbar}t} + e^{\frac{t}{\tau}} e^{i\frac{H_0}{\hbar}t} \rho(t) (-i\frac{H_0}{\hbar}) e^{-i\frac{H_0}{\hbar}t} \\
&= e^{\frac{t}{\tau}} e^{i\frac{H_0}{\hbar}t} \left\{ \frac{\rho}{\tau} + \frac{i}{\hbar}[H_0, \rho] - \frac{i}{\hbar}[H, \rho] - \frac{\rho - \rho_0}{\tau} \right\} e^{-i\frac{H_0}{\hbar}t} \\
&= -\frac{i}{\hbar}[\tilde{V}, \tilde{\rho}] + \frac{\rho_0}{\tau} e^{\frac{t}{\tau}},
\end{aligned} \tag{4.7}$$

where $\tilde{V}(t) = e^{i\frac{H_0}{\hbar}t}V(t)e^{-i\frac{H_0}{\hbar}t}$. Then we can integrate Eq. (4.7) to get

$$\begin{aligned}
\tilde{\rho}(t) &= \tilde{\rho}(0) - \frac{i}{\hbar}\int_0^t \mathrm{d}t'[\tilde{V}(t'), \tilde{\rho}(t')] + \frac{\rho_0}{\tau}\int_0^t \mathrm{d}t' e^{\frac{t'}{\tau}} \\
&= \rho_0 + \rho_0\left(e^{\frac{t}{\tau}} - 1\right) - \frac{i}{\hbar}\int_0^t \mathrm{d}t'[\tilde{V}(t'), \tilde{\rho}(t')] \\
&= \rho_0 e^{\frac{t}{\tau}} - \frac{i}{\hbar}\int_0^t \mathrm{d}t'[\tilde{V}(t'), \tilde{\rho}(t')] \\
&= \rho_0 e^{\frac{t}{\tau}} - \frac{i}{\hbar}\int_0^t \mathrm{d}t'\left[\tilde{V}(t'), \rho_0 e^{\frac{t'}{\tau}} - \frac{i}{\hbar}\int_0^{t'} \mathrm{d}t''[\tilde{V}(t''), \tilde{\rho}(t'')]\right] \\
&= \rho_0 e^{\frac{t}{\tau}} - \frac{i}{\hbar}\int_0^t \mathrm{d}t'\left[\tilde{V}(t'), \rho_0 e^{\frac{t'}{\tau}}\right] - \frac{i}{\hbar}\int_0^t \mathrm{d}t'\left[\tilde{V}(t'), -\frac{i}{\hbar}\int_0^{t'} \mathrm{d}t''[\tilde{V}(t''), \tilde{\rho}(t'')]\right] \\
&= \cdots
\end{aligned} \tag{4.8}$$

Iteratively putting $\tilde{\rho}(t)$ into the bracket yields

$$\tilde{\rho}(t) = \tilde{\rho}^{(0)}(t) + \tilde{\rho}^{(1)}(t) + \tilde{\rho}^{(2)}(t) + \cdots \tag{4.9}$$

with

$$\begin{aligned}
\tilde{\rho}^{(0)}(t) &= \rho_0 e^{\frac{t}{\tau}}, \\
\tilde{\rho}^{(n+1)}(t) &= -\frac{i}{\hbar}\int_0^t \mathrm{d}t'[\tilde{V}(t'), \tilde{\rho}^{(n)}(t')].
\end{aligned} \tag{4.10}$$

Then going back from $\tilde{\rho}(t)$ to $\rho(t)$ with $\rho(t) = e^{-\frac{t}{\tau}}e^{-i\frac{H_0}{\hbar}t}\tilde{\rho}(t)e^{i\frac{H_0}{\hbar}t}$, we have

$$\rho(t) = \rho^{(0)}(t) + \rho^{(1)}(t) + \rho^{(2)}(t) + \cdots \tag{4.11}$$

with

$$\rho^{(0)} = \rho_0, \tag{4.12}$$

and

$$\begin{aligned}
\rho^{(n+1)}(t) &= e^{-\frac{t}{\tau}} e^{-i\frac{H_0}{\hbar}t} \tilde{\rho}^{(n+1)}(t) e^{i\frac{H_0}{\hbar}t} \\
&= -\frac{i}{\hbar}\int_0^t \mathrm{d}t' e^{-\frac{t}{\tau}} e^{-i\frac{H_0}{\hbar}t} [\tilde{V}(t'), \tilde{\rho}^{(n)}(t')] e^{i\frac{H_0}{\hbar}t} \\
&= -\frac{i}{\hbar}\int_0^t \mathrm{d}t' e^{-\frac{t-t'}{\tau}} e^{-i\frac{H_0}{\hbar}(t-t')} [V(t'), \rho^{(n)}(t')] e^{i\frac{H_0}{\hbar}(t-t')} \\
&= \frac{i}{\hbar}\int_0^t \mathrm{d}t' e^{-\frac{t'}{\tau}} e^{-i\frac{H_0}{\hbar}t'} [V(t-t'), \rho^{(n)}(t-t')] e^{i\frac{H_0}{\hbar}t'}.
\end{aligned} \tag{4.13}$$

To deal with the time integration, one can use the Fourier transformation of $V(t-t')$

$$V(t-t') = \int \frac{\mathrm{d}\omega}{2\pi} V(\omega) e^{i\omega(t-t')}, \tag{4.14}$$

yielding

$$\begin{aligned}
\rho^{(1)}_{nm}(t) &= \left\langle n \middle| \rho^{(1)}(t) \middle| m \right\rangle \\
&= \frac{i}{\hbar}\int_0^t \mathrm{d}t' \left\langle n \middle| e^{-\frac{t'}{\tau}} e^{-i\frac{H_0}{\hbar}t'} [V(t-t'), \rho_0] e^{i\frac{H_0}{\hbar}t'} \middle| m \right\rangle \\
&= \frac{i}{\hbar}\int \frac{\mathrm{d}\omega}{2\pi} \langle n|[V(\omega), \rho_0]|m\rangle \, e^{i\omega t} \int_0^t \mathrm{d}t \exp\left(\frac{i}{\hbar}\left[(E_m - E_n) + \frac{i\hbar}{\tau} - \hbar\omega \right] t' \right) \\
&= \frac{i}{\hbar}\int \frac{\mathrm{d}\omega}{2\pi} V_{nm}(\omega)(f_m - f_n) e^{i\omega t} \frac{\exp\left(\frac{i}{\hbar}\left[(E_m - E_n) + \frac{i\hbar}{\tau} - \hbar\omega \right] t \right) - 1}{\frac{i}{\hbar}\left[(E_m - E_n) + \frac{i\hbar}{\tau} - \hbar\omega \right]} \\
&= \int \frac{\mathrm{d}\omega}{2\pi} e^{i\omega t} \frac{f_{nm} V_{nm}(\omega)}{E_{mn} - \hbar\omega + \frac{i\hbar}{\tau}},
\end{aligned} \tag{4.15}$$

where $|m\rangle$ and $|n\rangle$ are electronic states. $f_{mn} \equiv f_m - f_n$ and $E_{mn} \equiv E_m - E_n$ are the difference in the occupation number and the energy of $|m\rangle$ and $|n\rangle$. Meanwhile, $V_{mn} = \langle m|V|n\rangle$. Obviously, the first order perturbation in frequency domain is

$$\rho^{(1)}_{nm}(\omega;\omega) = \frac{f_{nm} V_{nm}(\omega)}{E_{mn} - \hbar\omega + \frac{i\hbar}{\tau}}. \tag{4.16}$$

4.2.2 Nuclear Electric Resonance

When we apply an external electric field $\mathscr{E}_p e^{i\omega_p t}$, which is oscillating in time with frequency ω_p, one has interaction as

$$V_{mn}(\omega_p) = \langle m| - e r_p \mathscr{E}_p |m\rangle = -e\mathscr{E}_p [r_p]_{mn}, \tag{4.17}$$

where $[r_p]_{mn} \equiv \langle m|r_p|n\rangle$ is the position operator of the electron. Then, one has

$$\rho^{(1)}_{mn}(\omega_p;\omega_p) = \frac{e f_{nm}[r_p]_{nm}}{E_{mn} - \hbar\omega_p}\mathscr{E}_p. \tag{4.18}$$

Here we ignored the $i\frac{\hbar}{\tau}$ term, which is not important when ω_p is far from E_{mn}. The oscillation in the electron density matrix leads to an oscillation in the EFG, which is

$$\begin{aligned} \Delta\mathscr{V}^{(1)} &= \mathrm{Tr}\left\{\rho^{(1)}\hat{\mathscr{V}}\right\} \\ &= e\mathscr{E}_p \sum_{mn} \frac{f_{nm}[\hat{\mathscr{V}}_{ij}]_{nm}[r_p]_{nm}}{E_{mn} - \hbar\omega_p}, \end{aligned} \tag{4.19}$$

where $\hat{\mathscr{V}}$ is the EFG operator and

$$[\hat{\mathscr{V}}_{ij}]_{mn} = \langle m|\hat{\mathscr{V}}_{ij}|n\rangle = \frac{1}{4\pi\varepsilon_0}\langle m|\frac{3r_i r_j - \delta_{ij}r^2}{r^5}|n\rangle. \tag{4.20}$$

Here ε_0 is the vacuum permittivity. Note that Eq. (4.20) is valid in the single-particle approximation and the exchange-correlation interaction between electrons is ignored.

The resultant perturbation in the nuclear quadrupole interaction is

$$H^{\mathrm{NER}} = \sum_{ij} \mathscr{C}^p_{ij}(\omega_p,\omega_p)\mathscr{E}_p I_i I_j \mathrm{e}^{i\omega_p t}, \tag{4.21}$$

where the response function $\mathscr{C}$ is defined as

$$\begin{aligned} C_{ij}^{p}(\omega_p, \omega_p) &= \frac{\partial Q_{ij}}{\partial \mathscr{E}_p} \\ &= \frac{e\boldsymbol{q}}{2I(2I-1)} \frac{\partial \Delta \mathscr{V}_{ij}^{(1)}}{\partial \mathscr{E}_p} \\ &= \frac{e^3\boldsymbol{q}}{2I(2I-1)} \sum_{mn} \frac{f_{nm}[\hat{\mathscr{V}}_{ij}]_{nm}[r_p]_{nm}}{E_{mn} - \hbar\omega_p}. \end{aligned} \tag{4.22}$$

One can see that H^{NER} oscillate in time with frequency ω_p. If ω_p matches the transition frequency Δ_{ge} between two nuclear spins states $|g\rangle$ and $|e\rangle$, then H^{NER} would be able to drive the resonant transitions between two $|g\rangle$ and $|e\rangle$, and the Rabi frequency is

$$f^{\mathrm{NER}} = \left| \sum_{ij} \langle g|I_i I_j|e\rangle \mathscr{C}_{ij}^{p} \mathscr{E}_p \right|. \tag{4.23}$$

Hence, one can use a microwave electric field to drive nuclear spin transitions. This is the so-called nuclear electric resonance (NER).

4.2.3 Features of the NER

Some features of the NER can be observed from Eq. (4.22). First, only electron orbital motions (described by $[r_p]_{mn}$) are explicitly involved, while electron spins do not appear. This suggests that electrons spins are not required for NER, in contrast to approaches based on the hyperfine interaction discussed in Chapter 3. Next, the frequency ω_p only appears in the denominator $\frac{1}{E_{mn}-\hbar\omega_p}$. Since ω_p needs to be resonant with nuclear spin frequencies, it should be in the microwave/radio frequency range, and is thus much smaller than E_{mn}, which is on the order of 1 eV in typical semiconductors. Consequently, the magnitude of $\mathscr{C}$ is almost independent of ω_q.

4.2.4 Analytical Estimation of the $\mathscr{C}$ tensor

The magnitude of the $\mathscr{C}$ tensor can be estimated using $\langle m|\frac{3r_i r_j - \delta_{ij} r^2}{r^5}|n\rangle \approx \frac{1}{a_0^3}$, and $\langle m|r_p|n\rangle \approx a_0$, where a_0 is the Bohr radius. Besides, although all (m, n) pairs con-

tribute to $\mathscr{C}$, the pair that satisfies $E_{mn} = E_g$, where E_g is the electron bandgap, makes the largest contribution. If we only consider this pair, then we have

$$\mathscr{C} \approx \frac{g_e e^3 \mathscr{q}}{2I(2I-1)} \frac{1}{4\pi\varepsilon_0 a_0^2} \frac{1}{E_g}, \tag{4.24}$$

where $g_e = 2$ is the electron spin degeneracy. For ^{75}As in zinc blende GaAs, one has $\mathscr{q} = 314$ mb, $I = \frac{3}{2}$, and $E_g \approx 1.4$ eV. This leads to $\mathscr{C} \approx 9.2 \times \frac{2\pi\cdot\text{MHz}}{\text{V/Å}}$ using Eq. (4.24).

4.3 Second-order Response: The Opto-Nuclear Quadrupolar Effect

In this section, we discuss the second order response of the nuclear quadrupole interaction to external electric fields. We first extend the linear response theory in Section 4.2.1 to the second order. Then we demonstrate that by applying two electric fields with different frequencies ω_p and ω_q, the nuclear quadrupole interaction could oscillate in the time with the difference-frequency $\omega_p - \omega_q$, which could be tuned to match nuclear spin frequency. This is the so-called ONQ effect. Finally, we give analytical estimation on the strength of the ONQ effect.

4.3.1 Quadratic Response Theory

Using Eqs. (4.13, 4.18), one can obtain the the second-order perturbation in the electron density matrix as

$$\begin{aligned}
\rho^{(2)}_{nm}(t) &= \left\langle n \middle| \rho^{(2)}(t) \middle| m \right\rangle \\
&= \frac{i}{\hbar} \int \frac{\mathrm{d}\omega'}{2\pi} e^{i\omega t} \int_0^t \mathrm{d}t' \exp\left(\frac{i}{\hbar} \left[(E_m - E_n) + \frac{i\hbar}{\tau} - \hbar\omega' \right] t' \right) \\
&\quad \times \sum_l \left(V_{nl}(\omega') \rho^{(1)}_{lm}(t-t') - \rho^{(1)}_{nl}(t-t') V_{lm}(\omega') \right) \\
&= \int \frac{\mathrm{d}\omega}{2\pi} \int \frac{\mathrm{d}\omega'}{2\pi} \frac{e^{i(\omega+\omega')t}}{E_{mn} - \hbar(\omega+\omega') + \frac{i\hbar}{\tau}} \sum_l \left(\frac{f_{lm} V_{nl}(\omega') V_{lm}(\omega)}{E_{ml} - \hbar\omega + \frac{i\hbar}{\tau}} - \frac{f_{nl} V_{nl}(\omega) V_{lm}(\omega')}{E_{ln} - \hbar\omega + \frac{i\hbar}{\tau}} \right)
\end{aligned} \tag{4.25}$$

Switching to the frequency domain, one has

$$\rho^{(2)}_{nm}(\omega+\omega';\omega,\omega') = \frac{1}{E_{mn}-\hbar(\omega+\omega')+\frac{i\hbar}{\tau}}\sum_l\left(\frac{f_{lm}V_{nl}(\omega')V_{lm}(\omega)}{E_{ml}-\hbar\omega+\frac{i\hbar}{\tau}}-\frac{f_{nl}V_{nl}(\omega)V_{lm}(\omega')}{E_{ln}-\hbar\omega+\frac{i\hbar}{\tau}}\right). \tag{4.26}$$

4.3.2 The Opto-Nuclear Quadrupolar Effect

When two electric fields $\mathscr{E}_{p(q)} = \mathscr{E}_{p(q)}e^{i\omega_{p(q)}t}$ are applied simultaneously, the electron cloud could have an orbital motion with frequency $\omega_p - \omega_q$, and the corresponding density matrix is [1]

$$\rho^{(2)}_{nm}(\omega_p-\omega_q;\omega_p,-\omega_q) = \frac{e^2\mathscr{E}_p\mathscr{E}_q}{E_{mn}-\hbar(\omega_p-\omega_q)}\sum_l\left\{\frac{f_{lm}[r_p]_{nl}[r_q]_{lm}}{E_{ml}-\hbar\omega_q}-\frac{f_{nl}[r_p]_{nl}[r_q]_{lm}}{E_{ln}-\hbar\omega_q}\right\}, \tag{4.27}$$

where the meaning of each term has been described in the previous section, and we have again ignored the $i\frac{\hbar}{\tau}$ term. Similar to that in the case of NER, the oscillating electron density matrix leads to an oscillating nuclear quadrupole interaction,

$$H^{\mathrm{ONQ}} = \sum_{ij}\mathscr{D}^{pq}_{ij}(\omega_p-\omega_q;\omega_p,-\omega_q)\mathscr{E}_p\mathscr{E}_q I_i I_j \mathrm{e}^{i(\omega_p-\omega_q)t}, \tag{4.28}$$

where $\mathscr{D}^{pq}_{ij}$ is a second-order response function, and can be expressed as

$$\begin{aligned}
&\mathscr{D}^{pq}_{ij}(\omega_p-\omega_q;\omega_p,-\omega_q)\\
&\equiv\frac{\partial^2 Q_{ij}}{\partial\mathscr{E}_p\partial\mathscr{E}_q}\\
&=\frac{e\boldsymbol{q}}{2I(2I-1)}\frac{\partial^2\mathscr{V}_{ij}}{\partial\mathscr{E}_p\partial\mathscr{E}_q}\\
&=\frac{e^4\boldsymbol{q}}{2I(2I-1)}\frac{1}{4\pi\varepsilon_0}\sum_{mnl}\frac{[\hat{\mathscr{V}}_{ij}]_{mn}}{E_{mn}-\hbar(\omega_p-\omega_q)}\left\{\frac{f_{lm}[r_p]_{nl}[r_q]_{lm}}{E_{ml}-\hbar\omega_q}-\frac{f_{nl}[r_p]_{nl}[r_q]_{lm}}{E_{ln}-\hbar\omega_q}\right\}.
\end{aligned} \tag{4.29}$$

Note that in Eq. (4.28) we omitted terms oscillating with ω_p, ω_q, and $\omega_p+\omega_q$, as they are far off-resonance with nuclear spin dynamics when $\omega_{p(q)}$ is in the optical range. A physical picture of the ONQ effect is that the electron wavefunction, and hence the

[1] Use $\omega=\omega_p$ and $\omega'=-\omega_q$ in Eq. (4.26)

EFG at the nuclear site, would oscillate in $|\omega_p - \omega_q|$ under the two-color laser [see a semi-classical illustration in Figure 4-1(a)], leading to the $|\omega_p - \omega_q|$ oscillation of H_{Q}.

The difference-frequency $\omega_p - \omega_q$ can be tuned to match nuclear spin frequencies. In the case of perfect resonance, the Hamiltonian in Eq. (4.28) could lead to an Rabi oscillation of nuclear spins between two states $|g\rangle$ and $|e\rangle$ with a Rabi frequency of

$$f^{\mathrm{ONQ}} = \left| \sum_{ij} \langle g|I_i I_j|e\rangle \mathscr{D}_{ij}^{pq} \mathscr{E}_p \mathscr{E}_q \right|. \tag{4.30}$$

4.3.3 Features of the ONQ Effect

From Eq. (4.29), one can see that the ONQ effect does not require electron spin as well. On the other hand, only the difference-frequency $\omega_p - \omega_q$ needs to be resonant with nuclear spin energy, while ω_p (ω_q) itself can be chosen freely in principle. Furthermore, as $\omega_{p(q)}$ only appears in the denominators such as $\frac{1}{E_{ml} - \hbar\omega_q}$, $\mathscr{D}$ is not sensitive to $\omega_{p(q)}$ when $\omega_{p(q)}$ is not close to the bandgap E_g. Therefore, there is relatively large flexibility in choosing $\omega_{p(q)}$. In practice, $\omega_{p(q)}$ can be chosen to match telecom frequency and/or minimize materials heating effect.

Notably, when $\omega_{p(q)} < E_g$, the electron can only do virtual transitions between three bands (m, n, l). In this case, the major contribution to the ONQ response comes from the (m, n, l) pair that satisfies $E_{mn}, E_{ml} = E_g$. On the other hand, when $\omega_{p(q)} > E_g$, electrons can do real interband transitions, and the (m, n, l) pair that satisfies $E_{ml} \approx \omega_{p(q)}$ (or $E_{nl} \approx \omega_{p(q)}$) would resonantly boost the ONQ response. In the following, we will only consider $\omega_{p(q)} < E_g$, because $\omega_{p(q)} > E_g$ leads to unwanted resonant absorption of the laser energy, which could damage the materials.

4.3.4 Analytical Estimation of the $\mathscr{D}$ Tensor

For a crude analytical estimation, one can again set $\langle m|\frac{3r_i r_j - \delta_{ij} r^2}{r^5}|n\rangle \sim \frac{1}{a_0^3}$, $\langle m|r_p|n\rangle \sim a_0$. Then, we only consider the (m, n, l) pair that satisfies $E_{mn} = E_{ml} = E_g$, which makes the major contribution to the total $\mathscr{D}$ tensor, according to the discussion above. While $\omega_{p(q)}$ is in the optical range and is usually comparable with E_g, the difference-

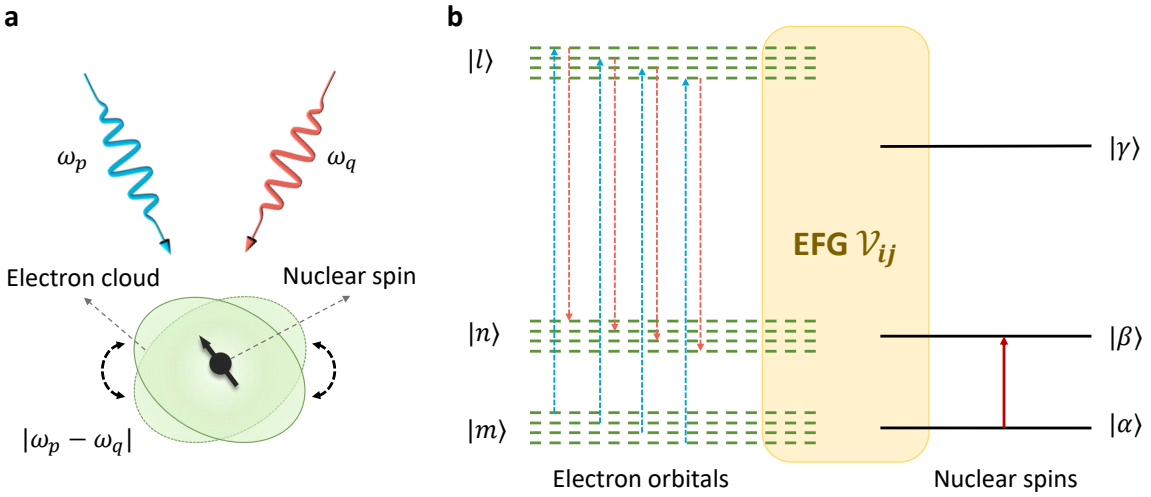

Figure 4-1: Illustration of the mechanism of the ONQ effect. (a) When two photons with respective frequencies ω_p and ω_q interact with the electron simultaneously, the electron cloud would vibrate with the difference-frequency $|\omega_p - \omega_q|$. Consequently, the nuclear quadrupole interaction would also oscillate in time with frequency $|\omega_p - \omega_q|$. (b) Energy level diagram of the ONQ effect. Under ω_p and ω_q-lasers (photons), electrons would do (virtual) transitions between three energy levels labelled by (n, m, l) and modulate the EFG at the nuclear site. Nuclear spins can transit between two different states if the frequency matching condition is satisfied.

frequency $\omega_p - \omega_q$ is in the MW range and can be neglected compared with E_g. Then, one has

$$\mathscr{D}(\omega_p - \omega_q; \omega_p, -\omega_q) \sim \frac{g_e e^4 q}{2I(2I-1)} \frac{1}{4\pi\varepsilon_0 a_0} \frac{1}{E_g(E_g - \hbar\omega_q)}. \tag{4.31}$$

For ^{75}As in zinc blende GaAs, one has $\mathscr{D} \approx 24 \times \frac{2\pi\cdot\text{MHz}}{(\text{V/Å})^2}$ when $E_g - \hbar\omega_q = 0.2$ eV.

Finally, from Eq. (4.31), one can see that $\mathscr{D}$ can be enhanced by using

- nuclei with large quadrupole moment,
- materials with small bandgap, and/or
- laser with a frequency close to (or even above) the bandgap.

4.4 DFT Calculations on the $\mathscr{C}$ and $\mathscr{D}$ Tensors

In the previous sections, we discussed the mechanism of the NER and the ONQ effects, which are respectively, the first- and second-order responses of the nuclear quadrupole

interaction under external electric/optical fields. In principle, these two effects are generic and should be present in any solid-state or molecular systems, unless forbidden by e.g., symmetries. For practical applications, of crucial importance is the strength of the responses under feasible experimental conditions.

In this section, we estimate the magnitude of the $\mathscr{C}$ and $\mathscr{D}$ tensor using density functional theory (DFT) [65, 66] calculations, to be compared with the analytical estimations in previous sections. The DFT calculations are performed using the Quantum Espresso package [71, 72]. Generalized gradient approximation (GGA) in the form of Perdew-Burke-Ernzerhof (PBE) [73] is used to treat the exchange-correlation interactions. Core and valence electrons are treated with projected augmented wave (PAW) method [74] and a plane wave basis, respectively. The first Brillouin zone is sampled by a k-mesh, and the convergence with respect to the k-mesh density has been tested. After the ground state wavefunctions are obtained, we apply a static electric field $\mathscr{E}$ along each Cartesian direction (x, y, and z) using the modern theory of polarization [75,76], and the change in the EFG tensors $\Delta\mathscr{V}$, and hence the change in the quadrupole tensor ΔQ can be obtained, from which we obtain the $\mathscr{C}$ and $\mathscr{D}$ tensors. Note that in this approach, $\mathscr{E}$ is a static field. As a result, what we obtain are the static response $\mathscr{C}(0;0)$ and $\mathscr{D}(0;0,0)$, i.e., $\omega_p = \omega_q = 0$.

4.4.1 Zinc blende gallium arsenide

We first take zinc blende gallium arsenide (zbGaAs) as an example. Ga has two abundant stable isotopes - ^{69}Ga (abundance 0.60) and ^{71}Ga (abundance 0.40) have $q = 171$ mb and $q = 107$ mb, respectively, and both of them have $I = \frac{3}{2}$. The only abundant isotope of As is ^{75}As, which has $q = 314$ mb and $I = \frac{3}{2}$. Notably, zbGaAs has tetrahedral symmetry, which enforces the EFG tensor at equilibrium (under no light illumination) to be fully isotropic, that is, $\mathscr{V}^{(0)} = \mathscr{V}_0\mathbb{I}$, where $\mathbb{I}$ is the identity matrix. On the other hand, the EFG tensor should be traceless by definition [Eq. (2.9)], and thus

$$\mathscr{V}_0 = 0, \tag{4.32}$$

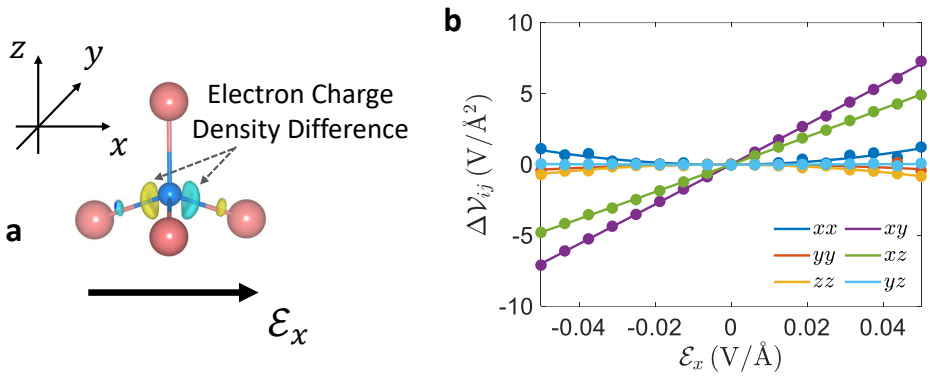

Figure 4-2: Estimation of the $\mathscr{D}$ tensor in zinc blende GaAs. (a) Yellow and green bubbles show positive and negative change in electron charge density when an electric field along x direction is applied. Pink and blue spheres are Ga and As atoms, respectively. (b) Change in EFG $\Delta\mathscr{V}_{ij}$ at the site of As nuclei in zbGaAs as a function of $\mathscr{E}_x$. Note that due to the $\mathscr{M}_x$ symmetry, some components of the $\mathscr{V}_{ij}$ tensor have zero first-order response, i.e., $\frac{\partial\mathscr{V}_{xx}}{\partial\mathscr{E}_x}\Big|_{\mathscr{E}_x=0} = 0$.

which means that the quadrupole interaction in zbGaAs is zero at equilibrium.

However, under external electric field, the electron wavefunction would redistribute in real space, which could break certain spatial symmetries (Figure 4-2a). Consequently, the response functions $\mathscr{C}$ and $\mathscr{D}$ are not necessarily zero. Indeed, $\mathscr{C}$ and $\mathscr{D}$ are third- and fourth-order tensors, which have more degrees of freedom that cannot be entirely forbidden by the tetrahedral symmetry [36]. In Figure 4-2b, we show the change in different components of the EFG tensor at the site of As nuclei as a function of $\mathscr{E}_x$. Interestingly, the first order responses $\frac{\partial\mathscr{V}_{ij}}{\partial\mathscr{E}_x}\Big|_{\mathscr{E}_x=0}$ is zero for certain components of the $\mathscr{V}$ tensor, such as $\mathscr{V}_{xx}$. This is because zbGaAs has mirror-x ($\mathscr{M}_x$) symmetry, which enforces

$$\begin{aligned} \frac{\partial\mathscr{V}_{xx}}{\partial\mathscr{E}_x}\Big|_{\mathscr{E}_x=0} &= -\frac{\partial\mathscr{V}_{xx}}{\partial\mathscr{E}_x}\Big|_{\mathscr{E}_x=0} \\ \Longrightarrow \frac{\partial\mathscr{V}_{xx}}{\partial\mathscr{E}_x}\Big|_{\mathscr{E}_x=0} &= 0. \end{aligned} \tag{4.33}$$

Furthermore, if the system has inversion symmetry and the nuclei under consideration lie at the inversion center, then the first-order responses $\mathscr{C}$ can be entirely forbidden. The second-order responses, on the other hand, are not constrained by mirror or

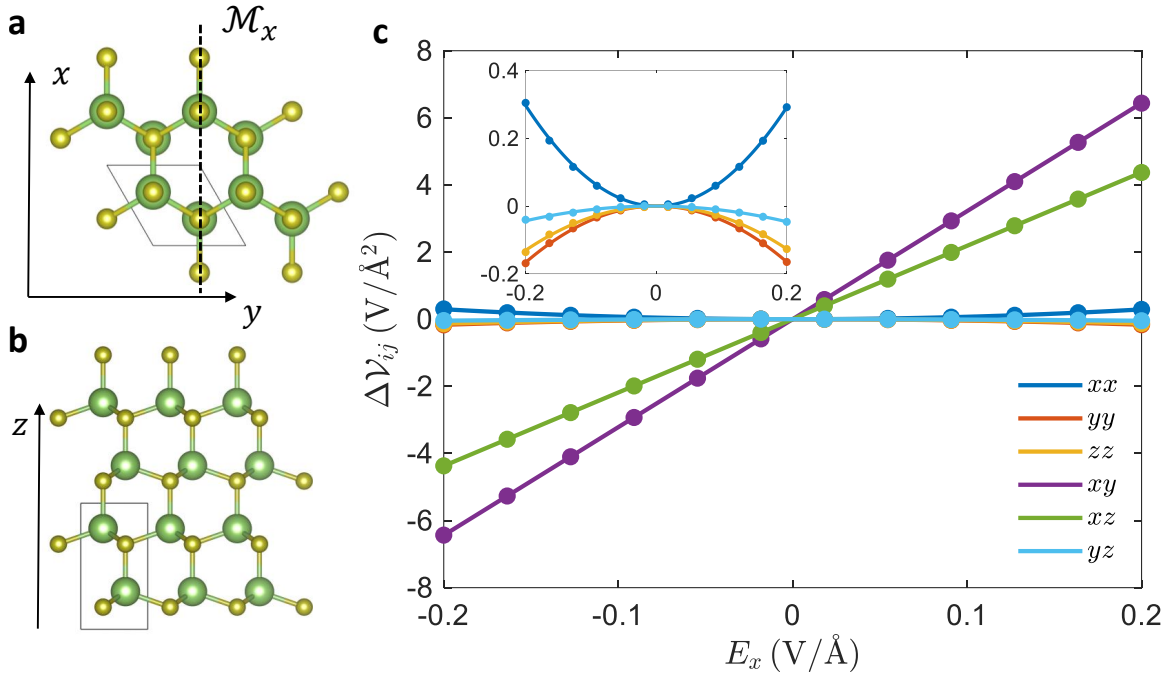

Figure 4-3: Estimation of the $\mathscr{D}$ tensor in wurtzite GaN. (a, b) Atomic structure of wurtzite GaN. The mirror symmetry $\mathscr{M}_x$ is labelled by the dashed line in (a). Green: Ga; Yellow: N. (c) change in EFG tensor $\Delta\mathscr{V}_{ij}$ of at the site of Ga nuclei as a function of $\mathscr{E}_x$.

inversion symmetries. By fitting the $\mathscr{V}_{ij}$ vs. $\mathscr{E}_x$ curves with second-order polynomials, one has

$$\begin{aligned} \mathscr{C} &\approx 4.9 \times \frac{2\pi \cdot \mathrm{MHz}}{\mathrm{V/\AA}} \\ \mathscr{D} &\approx 20.0 \times \frac{2\pi \cdot \mathrm{MHz}}{(\mathrm{V/\AA})^2} \end{aligned} \tag{4.34}$$

for ^{75}As in zbGaAs, which are in reasonable agreement with the analytical estimates in previous sections.

4.4.2 Wurtzite gallium nitride

Next, we study wurtzite gallium nitride (wGaN). Compared with zinc blende structure, wurtzite structure has slightly lower symmetry, which cannot entirely forbid $\mathscr{V}^{(0)}$ at equilibrium any more. Specifically, wGaN has P6$_3$mc symmetry, featuring a three-fold rotational symmetry along the z-axis and a $\mathscr{M}_x$ mirror symmetry. Here the z direction is the crystallographical c-axis of wGaN, while x-y plane is the crys-

tallographical a-b place, as shown in Figure 4-3(a,b). The equilibrium $\mathscr{V}^{(0)}$ tensor of wGaN is

$$\mathscr{V}^{(0)} = \begin{bmatrix} V & 0 & 0 \\ 0 & V & 0 \\ 0 & 0 & -2V \end{bmatrix}, \qquad V \approx 1.67 \text{ V/Å}^2. \tag{4.35}$$

Notably, the magnitude of $\mathscr{V}^{(0)}$ is relatively small. This is because although wGaN is in wurtzite structure, its deviation from the zinc blende structure is rather small - the lengths of inequivalent Ga-N bonds are respectively $l_1 \approx 1.974$ Å and $l_2 \approx 1.966$ Å, which are different by less than 1 %. Note that the zinc blende structure corresponds to $l_1 = l_2$.

Then we apply finite $\mathscr{E}_x$ in DFT calculations and the change in the EFG tensor $\Delta\mathscr{V}_{ij}$ as a function of $\mathscr{E}_x$ is shown in Figure 4-3(c). Again one can observe that some first-order responses are zero, thanks to the $\mathscr{M}_x$ symmetry. By fitting the $\Delta\mathscr{V}_{ij}$ - $\mathscr{E}_x$ curves with second-order polynomials, one has

$$\begin{aligned} \mathscr{C} &\approx 0.6 \times \frac{2\pi \cdot \text{MHz}}{\text{V/Å}}, \\ \mathscr{D} &\approx 0.2 \times \frac{2\pi \cdot \text{MHz}}{(\text{V/Å})^2}. \end{aligned} \tag{4.36}$$

4.4.3 Hafnium oxide

Next we study pristine HfO_2 crystal (space group $P2_1/c$). Hf is a heavy element with a large quadrupole moment. Specifically, ^{177}Hf (abundance 18.6 %) has $I = 7/2$ and $q = 3365$ mb, while ^{179}Hf (abundance 13.6 %) has $I = 9/2$ and $q = 3793$ mb. Notably, the spatial symmetry of HfO_2 [Figure 4-4(a)] is much lower than that of zbGaAs or wGaN, which is also manifested by the large EFG at equilibrium,

$$\mathscr{V}^{(0)} = \begin{bmatrix} -15.1 & -1.8 & -48.0 \\ -1.8 & -39.2 & 12.3 \\ -48.0 & 12.3 & 54.3 \end{bmatrix} \times \text{ V/Å}^2. \tag{4.37}$$

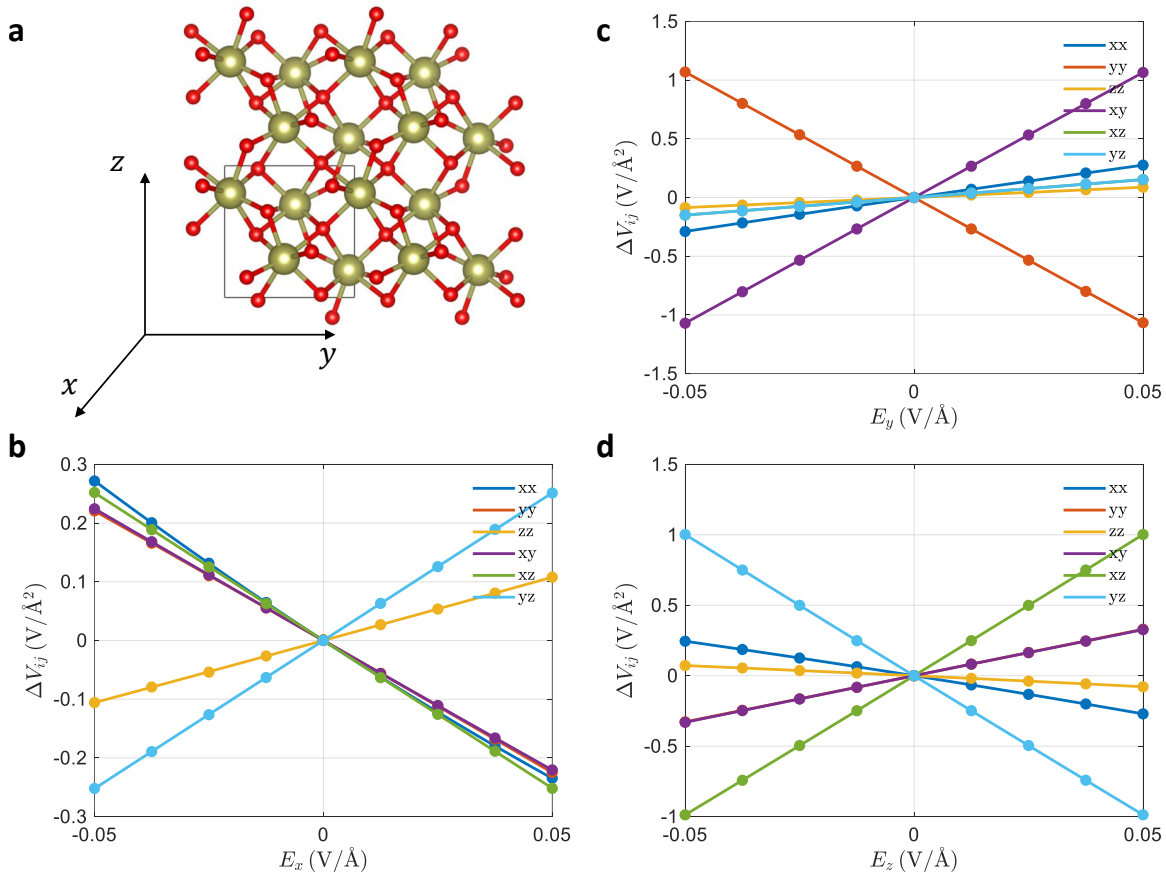

Figure 4-4: Estimation of the $\mathscr{D}$ tensor in HfO_2. (a) Atomic structure of HfO_2. Brown: hafnium; Red: oxygen. (b-d) An electric field $\mathscr{E}$ is applied along the (b) x, (c) y, and (d) z-direction and the change in EFG $\Delta\mathscr{V}_{ij}$ is calculated.

Combining the large EFG and the large quadrupole moment of Hf, the quadrupole interaction is found to be around 1 GHz for Hf. Static electric fields $\mathscr{E}$ along three dimensions are $\mathscr{E}$ are applied, and the change in EFG $\Delta\mathscr{V}_{ij}$ are shown in Figure 4-4(b-d). By fitting the raw data (solid points) with a polynomial (lines), the second-order response is found to be

$$\begin{aligned}\mathscr{C} &\approx 4.5 \times \frac{2\pi \cdot \mathrm{MHz}}{\mathrm{V/\AA}},\\ \mathscr{D} &\approx 2.3 \times \frac{2\pi \cdot \mathrm{MHz}}{(\mathrm{V/\AA})^2}.\end{aligned} \tag{4.38}$$

4.4.4 $\mathscr{D}$ at optical frequencies

As discussed before, the $\mathscr{C}$ and $\mathscr{D}$ tensors calculated with DFT are in the static limit $\omega_p = \omega_q = 0$. For the first order response, the frequency of the external electric field should be in the MW/RF range to achieve resonance with nuclear spins. Hence, ω_p should be much smaller than the bandgap of typical semiconductors, and one can safely treat $\omega_p \approx 0$. In other words, $\mathscr{C}(0;0)$ in the static limit can be considered as a good approximation of the true response function, which is $\mathscr{C}(\omega_p;\omega_p)$.

On the other hand, for the second-order response, the external fields are in the optical range, comparable with the electronic bandgap. In this case, the $\mathscr{D}$ tensors in the static limit calculated with DFT above should be considered as a lower bound for $\mathscr{D}$ tensors at optical frequencies $\mathscr{D}(\omega_p-\omega_q;\omega_p,-\omega_q)$. This is manifested in Eq. (4.29), where one can see that the magnitude of $\mathscr{D}$ should monotonically increase with ω_q for $\omega_q < E_g$. Physically, this is because the virtual interband transitions of electrons can be accelerated when the energy of the optical photons is closer to the bandgap. When $\omega_q > E_g$, electrons can do resonant interband transitions, and the responses can be significantly enhanced.

To further verify this point in DFT calculations, we use materials with narrower bandgaps. Naively, this would enhance the static responses because in this case ω_q would closer to E_g [see also Eq. (4.29)]. Figure 4-5(a) shows the second-order respons in EFG tensor, $\frac{\partial^2 V_{xx}}{\partial \mathscr{E}_x^2}$, as a function of the bandgap E_g for all wurtzite III-V materials

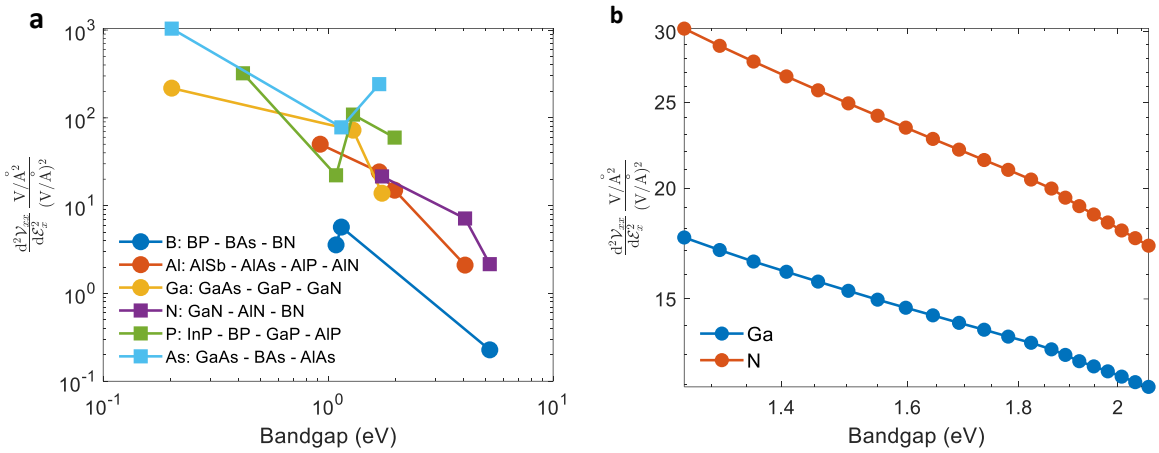

Figure 4-5: Magnitude of the second-order response in the EFG tensor $\frac{\partial^2 \mathscr{V}_{xx}}{\partial \mathscr{E}_x^2}$ against bandgap E_g. (a) $\frac{\partial^2 \mathscr{V}_{xx}}{\partial \mathscr{E}_x^2}$ against the bandgap E_g of all III-V semiconductors in wurtzite structure with $E_g > 0$ in DFT calculations. (b) $\frac{\partial^2 \mathscr{V}_{xx}}{\partial \mathscr{E}_x^2}$ against E_g for wurtzite GaN. Uniaxial strain is applied along the c-axis of wurtzite GaN, so that the bandgap can be continuously modified.

with $E_g > 0$ in DFT calculations [2]. Clearly, $\frac{\partial^2 V_{xx}}{\partial \mathscr{E}_x^2}$ is larger in magnitude when E_g is smaller. Specifically, for GaAs with $E_g \sim 0.2$ eV in DFT calculation, one has $\frac{\partial^2 V_{xx}}{\partial \mathscr{E}_x^2} \sim 10^3 \times \frac{\mathrm{V/\mathring{A}^2}}{(\mathrm{V/\mathring{A}})^2}$, corresponding to $\mathscr{D} \sim 10^2 \times \frac{2\pi \cdot \mathrm{MHz}}{(\mathrm{V/\mathring{A}})^2}$ for Ga nuclei. We also artificially strain wGaN so that its bandgap E_g can be continuously modified. Again, the $\frac{\partial^2 V_{xx}}{\partial \mathscr{E}_x^2}$ increases as E_g shrinks [Figure 4-5(b)].

Besides $\frac{\partial^2 V}{\partial \mathscr{E}^2}$, $\mathscr{D}$ tensor is also dependent on the quadrupole moment $\boldsymbol{q}$ and angular momentum I of the nucleus under consideration. For nuclei with small $\boldsymbol{q}$ such as Ga, one has $\mathscr{D} \sim [1 \sim 10^2] \times \frac{2\pi \cdot \mathrm{MHz}}{(\mathrm{V/\mathring{A}})^2}$. For nuclei with large $\boldsymbol{q}$ such as Hf, $\mathscr{D}$ can reach $[10 \sim 10^3] \times \frac{2\pi \cdot \mathrm{MHz}}{(\mathrm{V/\mathring{A}})^2}$ or even larger values.

In summary, we will take

$$\begin{aligned} \mathscr{E} &\approx 5 \times \frac{2\pi \cdot \mathrm{MHz}}{\mathrm{V/\mathring{A}}}, \\ \mathscr{D} &\approx 100 \times \frac{2\pi \cdot \mathrm{MHz}}{(\mathrm{V/\mathring{A}})^2} \end{aligned} \tag{4.39}$$

for discussions in following chapters.

[2] Note that DFT calculations usually underestimate the bandgap

4.5 Validity of the Estimation of the $\mathscr{C}$ and $\mathscr{D}$ Tensors

In previous sections, we estimated the $\mathscr{C}$ and $\mathscr{D}$ tensors using both analytical perturbation theory and DFT calculations, and the results exhibit reasonable agreement. In this section, we further assess the validity of these estimations. We will show that these estimations should give the correct order of magnitude of the $\mathscr{C}$ and $\mathscr{D}$ tensors.

4.5.1 Quadrupole Interaction Strength from DFT Calculations

First, we note that the quadrupole interaction strength in equilibrium $Q^{(0)}$ calculated by DFT methods usually agree well with experimental results. For example, Ref. [77] studied the quadrupole splitting $C_q \equiv \frac{eq\mathscr{V}_{zz}}{h}$ of nitrogen-vacancy (NV) center using both DFT calculations and experimental measurements. Here $\mathscr{V}_{zz}$ is the largest principle value of the EFG tensor $\mathscr{V}$. It is found that DFT and experimental results are off by around 5 % (Table 1 therein). Meanwhile, our DFT calculations give $C_q \approx 5.1$ MHz for NV^-, in good agreement with experimental results, which is 4.95 MHz.

Besides, the validity of DFT calculation of other spin-related quantities of point defects, such as hyperfine interaction, zero-field splitting, etc., has been systematically analyzed in Refs. [62, 78] as well. It is found that DFT calculations usually agree well with experimental results.

4.5.2 NER Response

The NER response has been studied experimentally. Here we compare our theoretical prediction on strength of the NER response with experimental results, which supports the validity of the theoretical approaches used in this work.

Experimental Results

In Ref. [70], the NER response of ^{75}As in GaAs quantum well was studied, and the response function $\mathscr{C}$ can be estimated from the data therein, which is

$$\mathscr{C}_{\text{exp}}^{^{75}\text{As}} \sim 20 \times \frac{2\pi \cdot \text{MHz}}{\text{V/Å}}. \tag{4.40}$$

In Ref. [29], the NER response of ^{123}Sb point defect in Si was studied, and the the response function $\mathscr{C}$ can be estimated from the data there in, which is

$$\mathscr{C}_{\text{exp}}^{^{123}\text{Sb}} \sim 30 \times \frac{2\pi \cdot \text{MHz}}{\text{V/Å}}. \tag{4.41}$$

Perturbation Theory Estimation

As discussed in Section 4.2.4, using first-order perturbation theory, the $\mathscr{C}$ tensor can be estimated with

$$\mathscr{C}_{\text{pertb}} \approx \frac{g_e e^3 q}{2I(2I-1)} \frac{1}{4\pi\varepsilon_0 a_0^2} \frac{1}{E_g}. \tag{4.42}$$

For ^{75}As in GaAs, one has $I = \frac{3}{2}$, $E_g = 1.42$ eV, and $q = 314$ mb, leading to

$$\mathscr{C}_{\text{pertb}}^{^{75}\text{As}} \sim 9.1 \times \frac{2\pi \cdot \text{MHz}}{\text{V/Å}}. \tag{4.43}$$

Similarly, for ^{123}Sb defects in Si, one has

$$\mathscr{C}_{\text{pertb}}^{^{123}\text{Sb}} \sim 8.2 \times \frac{2\pi \cdot \text{MHz}}{\text{V/Å}}. \tag{4.44}$$

Here we used $E_g = 0.56$ eV, which is half the bandgap of Si. This is because we need to considere the defect state from ^{123}Sb, which lies inside the bandgap of the Si matrix.

DFT Calculations

As discussed in Section 4.4, the $\mathscr{C}$ tensor can be obtained from DFT calculations as well, which give

$$\mathscr{C}_{\mathrm{DFT}}^{^{75}\mathrm{As}} \sim 4.9 \times \frac{2\pi \cdot \mathrm{MHz}}{\mathrm{V/\AA}}, \tag{4.45}$$

and

$$\mathscr{C}_{\mathrm{DFT}}^{^{123}\mathrm{Sb}} \sim 12.1 \times \frac{2\pi \cdot \mathrm{MHz}}{\mathrm{V/\AA}}. \tag{4.46}$$

One can see that for the NER, which is the first-order response, the theoretical predictions from both the perturbation theory and the DFT calculations give the correct order of magnitude of the $\mathscr{C}$ tensor, as compared with experimental results. Notably, the experimental results are slightly greater than the theoretical predictions for both ^{75}As and ^{123}Sb.

4.5.3 ONQ Response

The ONQ effect we proposed is the second-order response of the quadrupole interaction to the electric field. To the best of our knowledge, there are no experimental data on such a second-order response. On the other hand, the theoretical methods used to calculate the strength of the second-order ONR response are in the same spirit to those used to calculate the strength of the first-order NER response. Hence, we believe they should give reasonable results as well.

Chapter 5

NER and ONQ in Comparison with Other Effects

In this chapter, we compare NER and ONQ with other effects that can couple magnetic, electric, or optical fields to nuclear spins.

5.1 NER vs. NMR

As discussed in Sections 4.2 and 2.1, NER and NMR are the first order response to MW/RF electric and magnetic fields, respectively. Compared with magnetic fields, electric fields usually have better controllability and relatively higher temporal/spatial resolution. This is an unique advantage of NER. On the other hand, NER is not applicable to all nuclei - NER requires the nuclear spin quantum number to be great than $\frac{1}{2}$, otherwise the quadrupole interaction does not exist.

Another important parameter is the interaction strength of NER and NMR. As discussed in Sections 4.2 and 4.4, the strength of NER is

$$\mathscr{C} \sim [1 \sim 10] \times \frac{2\pi \cdot \mathrm{MHz}}{\mathrm{V/\AA}}. \tag{5.1}$$

On the other hand, the strength of NMR is

$$\begin{aligned}\gamma_N &\sim 10 \times \frac{2\pi \cdot \mathrm{MHz}}{\mathrm{T}} \\ &\sim 300 \times \frac{2\pi \cdot \mathrm{MHz}}{\mathrm{V/\AA}}.\end{aligned} \tag{5.2}$$

On the second line we used $\mathscr{E} = c_0 \mathscr{B}$ to convert the strength of magnetic field to electric field of a plane wave (c_0 is the speed of light). Comparing Eq. (5.1, 5.2), one can see that when plane wave MW/RF fields (or MW/RF photons) are used to manipulate nuclear spins, the NMR should be much stronger than NER. Of course, in some situations one has $\mathscr{E} \gg c_0 \mathscr{B}$ and the NER could dominate the NMR.

5.2 ONQ vs. Other Nonlinear Optical Effects

Next, we compare the ONQ effect with other nonlinear optical (NLO) effects that could couple optical photons with nuclear spins. Here we only consider NLO effects that do not require ancilla electron spins and exclude those discussed in Section 3.2. We demonstrate that the ONQ effect has the strongest responses among these possible NLO effects.

5.2.1 Nonlinear Nuclear Zeeman Effect

Optical photons have associated magnetic fields $\mathscr{B} e^{i\omega t}$, which can couple with nuclear spins through the Zeeman interaction $H_{\mathrm{Z}} = \gamma_N \sum_i \mathscr{B}_i I_i$. This interaction is also oscillating at optical frequencies ω, so the resonance with nuclear spins is achievable only when two optical photons with frequencies ω_p and ω_q interact with the nuclear spins simultaneously,

$$H^{\mathrm{NNZ}} = \gamma_N \sum_i \left(I_i \mathscr{B}_i^p e^{i\omega_p t} + I_i \mathscr{B}_i^q e^{i\omega_q t} \right). \tag{5.3}$$

Using the second-order perturbation theory, one has an effective Hamiltonian,

$$\begin{aligned} H_{\text{eff}}^{\text{NNZ}} &\sim \sum_{ij} I_i I_j \gamma_N^2 \frac{1}{\omega_p - \Delta_N} \mathscr{B}_i^p \mathscr{B}_j^q e^{i(\omega_p - \omega_q)} \\ &\sim \sum_{ij} I_i I_j \frac{\gamma_N^2}{c_0^2} \frac{1}{\omega_p - \Delta_N} \mathscr{E}_i^p \mathscr{E}_j^q e^{i(\omega_p - \omega_q)}, \end{aligned} \tag{5.4}$$

where Δ_N is the nuclear spin splitting and is in the MW/RF range. On the second line we used $\mathscr{E} = c_0 \mathscr{B}$ again. One can see that $H_{\text{eff}}^{\text{NNZ}}$ is oscillating in time with the difference-frequency $\omega_p - \omega_q$, which can be tuned to match nuclear spin frequencies. Hence, $H_{\text{eff}}^{\text{NNZ}}$ can drive the Rabi oscillation of nuclear spins, which can be called the nonlinear nuclear Zeeman (NNZ) effect.

The interaction strength of NNZ is

$$g^{\text{NNZ}} = \frac{\gamma_N^2}{c_0^2} \frac{1}{\omega_p - \Delta_N} \sim 10^{-4} \times \frac{2\pi \cdot \text{MHz}}{(\text{V/Å})^2}, \tag{5.5}$$

which is smaller than that of ONQ by more than four orders of magnitude.

5.2.2 Nonlinear Nuclear Electric Resonance

In Sec. 4.1, we discussed that the quadrupole tensor would have a linear response to external electric field, which is the NER effect. If simultaneously apply two electric fields with frequency ω_p and ω_q, respectively, the Hamiltonian would be

$$H^{\text{NNER}} = \sum_{ij} \left(\mathscr{C}_{ij}^p \mathscr{E}_p I_i I_j \mathrm{e}^{i\omega_p t} + \mathscr{C}_{ij}^q \mathscr{E}_q I_i I_j \mathrm{e}^{i\omega_q t} \right). \tag{5.6}$$

Similar to that in the case of NNZ, Eq. (5.6) would lead to a nonlinear nuclear electric resonance effect (NNER), whose effective Hamiltonian is

$$H_{\text{eff}}^{\text{NNER}} \sim \sum_{ijkl} I_i I_j I_k I_l \frac{\mathscr{C}_{ij}^p \mathscr{C}_{kl}^q}{\omega_p - \Delta_N} \mathscr{E}_p \mathscr{E}_q. \tag{5.7}$$

Table 5.1: Order of nonlinear optical effects that couple optical photons and nuclear spins. Interactions involving nuclear spins are in bold font.

	Electron dipole	Nuclear Zeeman	Nuclear quadrupole	Strength $\left[\frac{2\pi\cdot\mathrm{MHz}}{(\mathrm{V/\AA})^2}\right]$
ONQ	second	/	**first**	10^2
NNZ	/	**second**	/	10^{-4}
NNER	second	/	**second**	10^{-6}
Strength	$10^8 \times \frac{2\pi\cdot\mathrm{MHz}}{\mathrm{V/\AA}}$	$300 \times \frac{2\pi\cdot\mathrm{MHz}}{\mathrm{V/\AA}}$	$[1 \sim 10^3] \times 2\pi \cdot \mathrm{MHz}$	/

The effective coupling strength is

$$\mathscr{g}^{\mathrm{NNER}} = \frac{\mathscr{C}_{ij}^{p}\mathscr{C}_{kl}^{q}}{\omega_p - \Delta_N} \sim 10^{-6} \times \frac{2\pi \cdot \mathrm{MHz}}{(\mathrm{V/\AA})^2}, \tag{5.8}$$

where we have used $\mathscr{C}_{ij}^{p} \sim 10 \times \frac{2\pi\cdot\mathrm{MHz}}{\mathrm{V/\AA}}$. One can see that NNER is even weaker than NNZ.

5.2.3 Why the ONQ Effect is Strong

The coupling strength of the ONQ effect can be on the order of $10^2 \times \frac{2\pi\cdot\mathrm{MHz}}{(\mathrm{V/\AA})^2}$, which is stronger than those of NNZ and NNER by several orders of magnitude. To elucidate the reason why the ONQ effect is the strongest, we need to distinguish three types of interactions, namely

1. **Electron dipole interaction**: the interaction between electric field and electron, whose strength is on the order of $1 \times \frac{\mathrm{eV}}{\mathrm{V/\AA}} \sim 10^8 \times \frac{2\pi\cdot\mathrm{MHz}}{\mathrm{V/\AA}}$;

2. **Nuclear Zeeman interaction**: the interaction between magnetic field and nuclear spin, whose strength is on the order of $10 \times \frac{2\pi\cdot\mathrm{MHz}}{\mathrm{T}} \sim 300 \times \frac{2\pi\cdot\mathrm{MHz}}{\mathrm{V/\AA}}$;

3. **Nuclear quadrupole interaction**: the interaction between electron nuclear spin, whose strength is on the order of $2\pi \cdot [1 \sim 10^3] \times \mathrm{MHz}$.

Note that 1 eV is equivalent to $10^8 \times 2\pi \cdot \mathrm{MHz}$. One can see that the electron dipole interaction is very strong. In contrast, the nuclear Zeeman and quadrupole

interactions are rather weak.

The NLO effects, including ONQ, NNZ, and NNER, involve different order of the interactions discussed above, which are shown in Table 5.1. One can see that for ONQ, the second-order nonlinear process actually happens between photons and electrons (electron dipole interaction), while the interaction involving nuclear spin is first-order. In contrast, for NNZ and NNER, the interaction involving nuclear spin (either nuclear Zeeman or nuclear quadrupole interaction) is second-order, which makes them significantly weaker than the ONQ effect.

Chapter 6

Applications of the NER Effect

In this chapter, we discuss some potential applications of the NER effect, which is summarized in Table 6.1.

6.1 Manipulation of Single Nuclear Spin

Different from magnetic fields, electric fields can be well-controlled down to the nano-scale. Therefore, it is possible to realize electrical control over single nuclear spin, even if the nuclear spins have relatively high number density. The mechanism of the NER manipulation over single nuclear spin has been discussed in Section 4.2.2 and Refs. [30, 31]. Experimentally, it has been demonstrated in Ref. [29].

Table 6.1: Potential applications of the NER effect.

Application	ω_p-photon	Nuclear Spin(s)	Frequency Matching Condition
Single Nuclear Spin Manipulation	Pump	$\|e\rangle \leftrightarrow \|g\rangle$	$\omega_p = \Delta_{ge}$
Nuclear Spin Ensemble Manipulation	Annihilation	$\|n\rangle \rightarrow \|n+1\rangle$	$\omega_p = \omega_m$
	creation	$\|n+1\rangle \rightarrow \|n\rangle$	
Spectroscopy	Pump	$\|e\rangle \leftrightarrow \|g\rangle$	$\omega_p = \Delta_{ge}(X)$

6.2 Manipulation of Nuclear Spin Ensemble

Besides controlling single nuclear spins, the NER effect can also be used to couple MW/RF electric fields with a nuclear spin ensemble (NSE). As we will show below, electric fields can excite an collective excitation of an NSE, which is the nuclear magnon. A practical application of this effect might be to use the NSE as a quantum memory to story the quantum information carried by an MW/RF photon.

Before further discussions, we would like to remark that for a photon which has $\mathscr{E} = c_0\mathscr{B}$, the NMR coupling should be stronger than the NER coupling (Section 5.1 and 6.2.3). Therefore, in terms of coupling strength, using the NER coupling is advantageous only when $\mathscr{E} \gg c_0\mathscr{B}$.

6.2.1 Nuclear Magnons

First, we briefly introduce the properties of the collective excitation of nuclear spins, which is here called nuclear magnon (NM). For brevity we assume that there is only one species of nuclei, and hence only one NM band. Multiple species lead to multiple NM bands. However, having multiple NM bands would not change the basic properties of the NMs. This is because the NM bandgap is much larger than the NM bandwidth, so different NM bands are effectively isolated from each other. The Hamiltonian of a NSE can be written as (cf. Chapter 2)

$$\mathscr{H}_N = \sum_{\alpha} \left(\gamma_N I^{\alpha} \cdot \mathscr{B} + I^{\alpha} \cdot Q \cdot I^{\alpha}\right) + \sum_{\alpha\beta} I^{\alpha} \cdot \mathscr{J}^{\alpha\beta} \cdot I^{\beta}. \tag{6.1}$$

Here we assume there is no electron spin ($S = 0$) and neglect the hyperfine interaction. The spin operators are hard to deal with theoretically, so we perform the Holstein–Primakoff transformation [79] to transform the spin operators I^{α} to boson

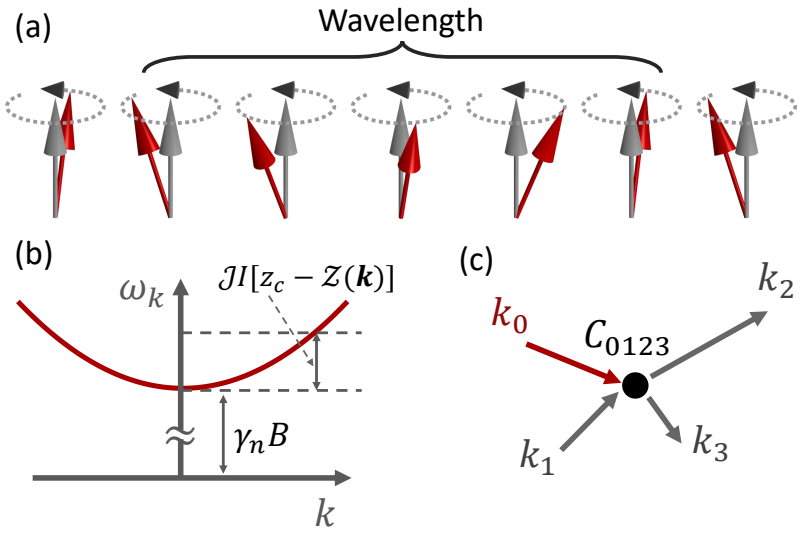

Figure 6-1: (a) Illustration of the NM mode. The ground state of the nuclear spins are denoted by grey upright arrows. When NMs are excited, nuclear spins (denoted by red arrows) precess around the ground states. The spatial pattern of the NM has a periodicity, which is characterized by the wavelength. (b) Band dispersion of the NMs (not drawn to scale). Note that one has $\gamma_N \mathcal{B} \gg 2\mathcal{J}Id^2k^2$. (c) Illustration of the four-NM scattering process. The vertex is denoted by C_{0123}

creation (annihilation) operators $a_\alpha^\dagger$ (a_α),

$$\begin{aligned} I_z^\alpha &= I - a_\alpha^\dagger a_\alpha, \\ I_+^\alpha &= \sqrt{2I}\sqrt{1 - \frac{a_\alpha^\dagger a_\alpha}{2I}}\, a_\alpha, \\ I_-^\alpha &= \sqrt{2I}\, a_\alpha^\dagger \sqrt{1 - \frac{a_\alpha^\dagger a_\alpha}{2I}}, \end{aligned} \tag{6.2}$$

where $I_\pm \equiv I_x \pm i I_y$ are the angular momentum ladder operators. The square roots in Eq. (6.2) can be expanded using the Taylor expansion. For example,

$$I_+^\alpha = \sqrt{2I}\left[1 - \sum_{n=1} \frac{(2n-3)!!}{2^n n!}\left(\frac{a_\alpha^\dagger a_\alpha}{2I}\right)^2\right] a_\alpha, \tag{6.3}$$

which is applicable when $a_\alpha^\dagger a_\alpha < 2I$. More rigorously, the square root can be expanded using the Kubo operators [80,81], which avoids the error due to the truncation of the Taylor series in Eq. (6.3).

The eigenstates of the angular momentum operators are $|I, m_z\rangle_\alpha$, where $m_z = -I, -I+1, \cdots +I$ is the eigenvalue of I_z operator. After the Holstein–Primakoff transformation, the eigenstates become

$$\begin{aligned} |I, I-n\rangle_\alpha &\rightarrow |n\rangle_\alpha \\ &\equiv \frac{1}{\sqrt{(n)!}} \left(a_\alpha^\dagger\right)^n |0\rangle_\alpha, \end{aligned} \tag{6.4}$$

where $|0\rangle_\alpha$ is the vacuum state of the boson operator and corresponds to $|I, I\rangle_\alpha$. One can see that

$$a_\alpha^\dagger |I, I-n\rangle \rightarrow |I, I-(n+1)\rangle, \tag{6.5}$$

that is, the boson operators lead to the transition between angular momentum states with different m_z.

After the Holstein-Primakoff transformation, one can perform the Fourier transformation to switch from r-space to k-space, which is

$$\begin{aligned} a_\alpha &= \frac{1}{\sqrt{N}} \sum_k e^{ik\cdot r_\alpha} a_k, \\ a_k &= \frac{1}{\sqrt{N}} \sum_i e^{-ik\cdot r_\alpha} a_\alpha, \end{aligned} \tag{6.6}$$

where a_k is the annihilation operator of an NM mode with wavevector k, while r_α is the location of the α-th nuclear spin. N is the number of nuclear spins, and is used to normalize the Fourier transformation. A semi-classical one-dimensional picture of the NM mode is illustrated in Figure 6-1(a). Each nuclear spin precesses around its ground state, and the phase of the precession is $e^{ik\cdot r_\alpha}$ with r_α the location of the r_α-th nucleus, so the wavelength is $\lambda = \frac{2\pi}{k}$. This resembles the phonon modes, whereby the atomic vibrations have a $e^{ik\cdot r_\alpha}$ phase factor as well. NMs are in close analogy to electron magnons [82, 83].

After the Holstein–Primakoff transformation and the Fourier transformation, the NSE Hamiltonian Eq. (6.1) can be reformulated in the basis of NM creation (annihi-

lation) operators $a_k^\dagger$ (a_k), yielding

$$\mathscr{H}_N = \mathscr{H}^{(2)} + \mathscr{H}^{(3)} + \mathscr{H}^{(4)} + \cdots , \tag{6.7}$$

where $\mathscr{H}^{(\zeta)}$ contains ζ-number of $a_k^\dagger$ or a_k, and describes the interaction between ζ-number of NMs. Specifically, the quadratic term is

$$\mathscr{H}^{(2)} = \sum_k \omega_k a_k^\dagger a_k \tag{6.8}$$

with ω_k the frequency of the NM mode. Higher order terms such as $\mathscr{H}^{(3)}$ or $\mathscr{H}^{(4)}$ correspond to the interaction between multiple NMs, which lead to (1) shift of NM frequencies and (2) decay of NM, which corresponds to finite NM lifetime [84, 85].

The dipolar interaction between the magnetic moments of the nuclei is a fundamental electromagnetic interaction, and hence the $\mathscr{J}$-interaction is usually unavoidable. Meanwhile, the quadrupole interaction at equilibrium can be zero if the nucleus resides in a high-symmetry environment, such as the tetrahedral environment in zb-GaAs discussed in Section 4.4. For brevity, we will consider the case of $Q = 0$ hereafter. Without loss of generality, we assume the external magnetic field to be along the z-direction. We further assume $\mathscr{J}_{ij}^{\alpha\beta} = \mathscr{J}\delta_{\langle\alpha\beta\rangle}\delta_{ij}$, where δ_{ij} is the Kronecker delta and $\delta_{\langle\alpha\beta\rangle}$ enforces that there is only nearest neighbor interactions. Here we would like to note that the dipolar interaction between nuclear spins is a long-range interaction that decays with $\frac{1}{r^3}$, where r is the distance between nuclear spins. However, using the nearest-neighbor approximation would not influence the order-of-magnitude of the final results. For example, for an 1D chain, the potential energy per nuclear spin is $\sum_n \frac{\mathscr{J}}{n^3} \approx 1.2 \times \mathscr{J}, n \in \mathbb{Z}$ if all the interactions are considered. In 2D or 3D, the result depends on the crystal symmetry, but should be on the order of $\sum_n \frac{\mathscr{J}}{(\sqrt{n})^3} \approx 2.6 \times \mathscr{J}$. Meanwhile, only considering the nearest-neighbor interaction leads to a potential energy of $\mathscr{J}$ per nuclear spin, which is comparable with the results as above. One can also refer to the calculation of Madelung constants, which are also on the order of 1.

In this case, if we only consider $\mathscr{H}^{(2)}$, then we have

$$\omega_k = \gamma_N \mathscr{B} + \mathscr{J} I \left[z_c - \mathscr{E}(k) \right], \tag{6.9}$$

where z_c is the coordination number and $\mathscr{E}(k)$ is a function dependent on the crystal structure. For example, a three-dimensional simple cubic structure has

$$\begin{aligned} z_c - \mathscr{E}(k) &= 6 - 2\left[\cos(k_x d) + \cos(k_y d) + \cos(k_z d)\right] \\ &\approx k^2 d^2. \end{aligned} \tag{6.10}$$

Here d is the lattice constant. On the second line, we used the Taylor expansion for $kd \ll 1$, leading to

$$\omega_k \approx \gamma_N \mathscr{B} + \mathscr{J} I k^2 d^2. \tag{6.11}$$

In the case of $Q \neq 0$, the anisotropy from the nuclear quadrupolar interaction could modify the NM band dispersion. The anisotropy effect has been discussed in the case of electron magnon [83, 86, 87].

One can see that the dispersion of the NM frequency is determined by the nuclear spin-spin interaction $\mathscr{J}$. Remarkably, $\mathscr{J}$ is on the order of kHz, much smaller than $\gamma_N \mathscr{B}$, which is usually on the order of MHz. In other words, the bandwidth the NM bands are very small.

6.2.2 Decay Rate of NM

The decay rate of NMs is a crucial parameter that affects various applications of NMs. In this section, we will estimate the decay rate of NM. We will focus on NM near the Γ-point in the Brillouin zone. This is because the wavevector of photons is usually very small compared with the dimension of the Brillouin zone, and thus only NM near the Γ-point can effectively interact with photons, as imposed by the law of momentum conservation.

As discussed above, the NM decay results from the multi-NM interactions. The leading-order effect should have been $\mathscr{H}^{(3)}$, corresponding to the three-NM scattering.

However, due to the small NM bandwidth, three-NM scattering always violates energy conservation and cannot lead to NM decay. This is similar to the case of optical phonon decay in certain materials such as BAs or AlSb. In these materials, the lifetime of optical phonons are exceptionally long because three-phonon scatterings involving optical phonons are forbidden by the small optical phonon bandwidth and large bandgap between optical and acoustic phonons [88–91].

The leading order effect that leads to NM decay is four-NM scattering, which is described by

$$\mathscr{H}^{(4)} = \sum_{0,1,2,3} C_{0123} a_0 a_1 a_2^\dagger a_3^\dagger. \tag{6.12}$$

Eq. (6.12) corresponds to the $k_0 + k_1 \to k_2 + k_3$ scattering. Note that there could also be other scatterings, such as $k_0 \to k_1 + k_2 + k_3$. But these scatterings are forbidden by the energy conservation law as well and thus could not lead to NM decay. Here the subscripts $l = 0, 1, 2, 3$ label the NM with wavevector k_l that participate in the scattering, and 0 denotes the Γ-point NM under consideration.

The $\mathscr{H}^{(4)}$ coupling arises from the dipolar interaction when considering higher-order terms in the expansion of Eq. (6.2), and the coupling constant C_{0123} can be expressed as [84, 85]

$$C_{0123} = \frac{\mathscr{J}}{4} \left[\mathfrak{X}(k_0) + \mathfrak{X}(k_1) + \mathfrak{X}(k_2) + \mathfrak{X}(k_3) - 4\mathfrak{X}(k_0 - k_2) \right]. \tag{6.13}$$

The relaxation rate due to four-NM scattering can be obtained from Fermi's golden rule, and can be expressed as [84, 85, 88, 89]

$$\kappa_m^{(4)} = \frac{2\pi}{\hbar} \sum_{1,2,3} |C_{0123}|^2 \frac{(n_1 + 1) n_2 n_3}{n_0} \delta(\omega_0 + \omega_1 - \omega_2 - \omega_3) \Delta(k_0 + k_1 - k_2 - k_3). \tag{6.14}$$

Here ω, k and n are respectively the frequency, wavevector and occupation number of the NMs. $\Delta(k_0 + k_1 - k_2 - k_3)$ corresponds to momentum conservation and enforces $k_0 + k_1 = k_2 + k_3$. Meanwhile, $\delta(\omega_0 + \omega_1 - \omega_2 - \omega_3)$ corresponds to energy conservation.

Considering the dispersion relation in Eq. (6.11), one has

$$\delta(\omega_0+\omega_1-\omega_2-\omega_3)\approx\frac{\delta(\cos\theta_{23})}{2\mathcal{J}Id^2k_2k_3}, \tag{6.15}$$

where θ_{23} is the angle between k_2 and k_3. Considering the small NM band width, we will use $n_i=n_0$. For simplicity, we also use $|C_{0123}|\approx\mathcal{J}$ and ignore the k-dependence of C_{0123}. Then one has

$$\begin{aligned}\kappa_m^{(4)}&=\frac{2\pi}{\hbar}\mathcal{J}^2n_0(n_0+1)\left(\frac{d}{2\pi}\right)^6\int\mathrm{d}^3k_2\mathrm{d}^3k_3\delta(\omega_0+\omega_1-\omega_2-\omega_3)\\&=\frac{1}{(2\pi)^3}\frac{\mathcal{J}}{I\hbar}n_0(n_0+1)d^4\int_0^{k_{\max}}k_2\mathrm{d}k_2\int_0^{k_{\max}}k_3\mathrm{d}k_3\\&=\frac{\pi}{2}\left(\frac{3}{4\pi}\right)^{\frac{4}{3}}\frac{\mathcal{J}}{I\hbar}n_0(n_0+1).\end{aligned} \tag{6.16}$$

Here we approximate the first Brillouin zone with an isotropic sphere whose radius $k_{\max}$ is determined by $\frac{4\pi}{3}k_{\max}^3=\left(\frac{2\pi}{d}\right)^3$. As $\mathcal{J}$ is on the order of kHz, one has $\kappa_m^{(4)}\sim$ 0.1 kHz when $n_0=1$. Considering the assumptions used above (e.g., assuming a nearest-neighbor interaction $\mathcal{J}$ and ignoring the k-dependence of C_{0123}), which could influence the magnitude of $\kappa_0^{(4)}$, it is reasonable to use

$$\kappa_0^{(4)}\lesssim[0.1\sim1]\text{ kHz}. \tag{6.17}$$

Even higher-order terms $\mathscr{H}^{(\zeta)}$ with $\zeta>4$ in the Hamiltonian expansion [Eq. (6.7)] could result in NM relaxation $\kappa_0^{(\zeta)}$ as well. Due to the requirement of energy conservation, only even order terms $\zeta=2n$ ($n\in\mathbb{N}$) can contribute to NM relaxation. If one uses the Taylor expansion in Eq. (6.3) to expand the square roots in Eq. (6.2), then approximately one has

$$\frac{\kappa_m^{(\zeta+2)}}{\kappa_m^{(\zeta)}}\sim\frac{1}{2\zeta}n_0(n_0+1), \tag{6.18}$$

which can be obtained using a similar approach to that for calculating $\kappa_m^{(4)}$ above. Hence, $\kappa_m^{(4)}$ would make the major contribution to the total NM relaxation rate, as long

as $n_0 \lesssim 1$, which requires $k_B T \lesssim \omega_m$. If one has the NM frequency as $\omega_m \sim 30$ MHz, which can be realized with a magnetic field ~ 3 T, and the temperature as $T \sim 2$ mK, which is achievable in a dilute refrigerator, then n_0 would be around 0.94, largely satisfying the requirement discussed above.

Here we would like to remark that the Holstein-Primakoff transformation in Eq. (6.2) is rigorous as all the commutation relations of the spin operators are satisfied. The problem is how to deal with the square root. In the discussions above, we used the Taylor series [Eq. (6.3)] to expand the square root. This is not the most suitable approach for expanding the square roots in Eq. (6.2) when n_0 is comparable with $2I$ ($k_B T \gtrsim \omega_0$). An more rigorous approach uses the so-called Kubo operator [80, 81], which is

$$\sqrt{1 - \frac{a^\dagger a}{2I}} = 1 + f_1 n + f_2 n^2 + \cdots f_{2I} n^{2I}, \tag{6.19}$$

where $n \equiv a^\dagger a$. By selecting proper coefficients $f_1, f_2, \cdots f_{2I}$, one can make the expansion above rigorous for $0 \leq n \leq 2I$, $n \in \mathbb{Z}$. As an example, for $I = \frac{3}{2}$, one has

$$\sqrt{1 - \frac{a^\dagger a}{2I}} = 1 - \frac{1}{6}(11 + 3\sqrt{3} - 6\sqrt{6})n + \frac{1}{6}(6 + 4\sqrt{3} - 5\sqrt{6})n^2 + \frac{1}{6}(-1 - \sqrt{3} + \sqrt{6})n^3 \tag{6.20}$$

The Kubo-opeators have been used to deal with magnetism at all temperatures, including temperature near or above the (anti)-ferromagnetic transition temperature [80, 81]. Notably, using the Kubo operators, only up to the $4I$-th order term would appear in the expansion of the square root. Hence, the NM relaxation rate can be more rigorously computed. For example, for ^{75}As with $I = 3/2$, the NM relaxation rate only result from terms up to $\kappa_0^{(14)}$, instead of the infinite series in Eq. (6.18).

Besides the Kubo operators, there are also other approaches to treat the square roots in the Holstein-Primakoff transformation more rigorously than the Taylor series. One example is the Newton series studied in Ref. [92]. The rigorous treatment of the Holstein-Primakoff transformation is beyond the scope of the current work.

6.2.3 NER/NMR Effect of NM

Using the Holstein-Primakoff transformation, one has the single nuclear NER Hamiltonian as

$$\begin{aligned} H_\alpha^{\mathrm{NER}} &= \sum_{ij} \mathscr{C}_{ij}^p \mathscr{E}_p I_i^\alpha I_j^\alpha \\ &\approx \mathscr{g}^{\mathrm{NER}} \mathscr{E}_p a_\alpha + h.c. \end{aligned} \tag{6.21}$$

where we only kept the first-order terms $\propto a_\alpha, a_\alpha^\dagger$ in the Holstein-Primakoff transformation, which can be resonant with the electric field. $h.c.$ stands for Hermitian conjugate. $\mathscr{g}^{\mathrm{NER}} \sim \mathscr{C}_{ij}^p$ is the NER coupling strength with a single nuclear spin.

After second-quantizing the MW photon and switching to the k-space, one has the NER Hamiltonian of the NSE as

$$\begin{aligned} \mathscr{H}^{\mathrm{NER}} &= \sum_\alpha H_\alpha^{\mathrm{NER}} \\ &= \mathscr{g}^{\mathrm{NER}} \mathscr{E}^{\mathrm{zpf}} \sqrt{N} a_p^\dagger a_m + h.c. \end{aligned} \tag{6.22}$$

where $a_p^\dagger$ is the creation operator of an ω_p-photon, a_m is the annihilation operator of the NM that interacts with the ω_p-photon. The wavevector k of this NM is fixed by the momentum conservation and is thus omitted. As compared with the lattice constant d, the wavelength of MW photons is so long that only the magnetostatic NM with $k \approx 0$ interacts with the MW photon. Also,

$$\mathscr{E}^{\mathrm{zpf}} = \sqrt{\frac{\hbar \omega_p}{2 \varepsilon_0 V_p}} \tag{6.23}$$

is the zero-point electric field of the ω_p-photon in an MW/RF cavity with mode volume V_p. ε_0 is the vacuum permittivity. The Rabi frequency of the swapping between the NM and the ω_p-photon is

$$\begin{aligned} \mathscr{\ell}^{\mathrm{NER}} &= \mathscr{g}^{\mathrm{NER}} \mathscr{E}^{\mathrm{zpf}} \sqrt{N} \\ &= \mathscr{g}^{\mathrm{NER}} \sqrt{\frac{\hbar \omega_p \rho}{2 \varepsilon_0}}, \end{aligned} \tag{6.24}$$

where $\rho = N/V_p$ is an effective number density of the nuclear spins. We use $\rho =$

20^{28} m^{-3}, and one has $\ell^{\rm NER} \sim 0.1$ kHz with $\omega_p = 10$ MHz and $\mathscr{C} = 5 \times \frac{2\pi\cdot\text{MHz}}{\text{V/Å}}$.

As a comparison, we examine the interaction strength between the ω_p-photon and the NM via NMR. In this case, the coupling Hamiltonian should be

$$\mathscr{H}^{\rm NMR} = \gamma_N \mathscr{B}^{\rm zpf} \sqrt{N} a_p^\dagger a_m + h.c. \tag{6.25}$$

where

$$\mathscr{B}^{\rm zpf} = \sqrt{\frac{\mu_0 \hbar \omega_p}{2V_p}} \tag{6.26}$$

is the zero-point magnetic field of the ω_p in a MW cavity, with μ_0 as the vacuum permeability. It is straightforward to find that the NMR Rabi frequency is $\ell^{\rm NMR} \sim$ 6 kHz under the same condition as discussed above.

6.3 Spectroscopy

Similar to NMR, NER can be used for spectroscopy as well. In NMR spectroscopy, the resonance frequency of nuclear spins is predominantly determined by the gyromagnetic ratio of the isotope (e.g., $42.577 \times \frac{2\pi\cdot\text{MHz}}{\text{T}}$ for ^{1}H and $10.71 \times \frac{2\pi\cdot\text{MHz}}{\text{T}}$ ^{13}C), which is a constant for the isotope in different environments. The change in resonance frequency, which is the so-called "chemical shift" and is used to extract information on the chemical environment, only comes from the shielding effect of surrounding electrons. In normal non-magnetic materials, the shielding effect is usually very weak [1]. Consequently, only a small change in the resonance frequency (usually on the order of tens of ppm, part in million) can be induced, which necessitates sophisticated control over external magnetic fields and/or the RF spectrometer.

In contrast, a unique advantage of NER spectroscopy is that the resonance frequency of a certain isotope is sensitively dependent on the environment, because the EFG is directly generated by surrounding electrons. For example, in zinc blende GaAs, the quadrupole splitting of ^{75}As is zero, thanks to the tetrahedral symmetry.

[1] Recall that the relative magnetic susceptibility of nonmagnetic materials is usually on the order of 10^{-6}

In wurtzite GaAs, the quadrupole splitting of ^{75}As is around 2.5 MHz. One can see that the resonance frequency can be very sensitive to the environment of the isotope under consideration.

Chapter 7

Applications of the ONQ Effect

The ONQ effect establishes an efficient interface between nuclear spins and optical photons. In this chapter, we will discuss some potential applications of such an interface. A summary of these applications can be found in Table 7.3.

7.1 Single Nuclear Spin Manipulation

First, we will discuss the ONQ control over single nuclear spin in more detail, which will be the foundation of other applications of the ONQ effect. As discussed in Section 4.3.2, under two-color lasers with respective frequencies ω_p and ω_q, there will be an ONQ Hamiltonian, which oscillates with time at frequency $|\omega_p - \omega_q|$,

$$H^{\mathrm{ONQ}} = \sum_{ij} \mathscr{D}_{ij}^{pq}(\omega_p - \omega_q; \omega_p, -\omega_q)\mathscr{E}_p\mathscr{E}_q I_i I_j \mathrm{e}^{i(\omega_p-\omega_q)t} + h.c \tag{7.1}$$

where $\mathscr{E}_p$ ($\mathscr{E}_q$) is the electric field strength of the ω_p (ω_q) laser.

7.1.1 Rabi Oscillation

In the basis of $\{|g\rangle, |e\rangle\}$, which are the ground and excited nuclear spin states under consideration, the effective ONQ Hamiltonian in the rotating frame is

$$H_{\mathrm{eff}}^{\mathrm{ONQ}} = \frac{\delta}{2}\left(|e\rangle\langle e| - |g\rangle\langle g|\right) + \left[g^{\mathrm{ONQ}}\mathscr{E}_p\mathscr{E}_q|e\rangle\langle g| + h.c.\right], \tag{7.2}$$

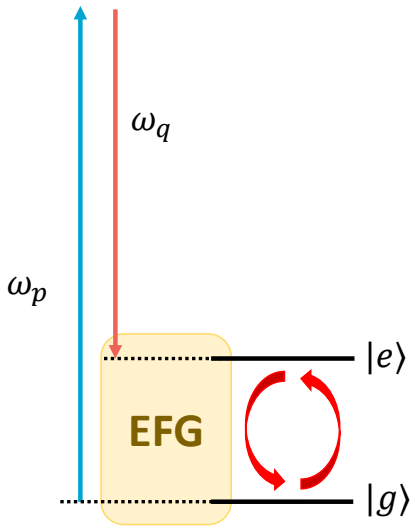

Figure 7-1: Illustration of the ONQ control over single nuclear spin. Two lasers with respective frequencies ω_p and ω_q are applied simultaneously. When the difference-frequency is resonant with nuclear spin transition energy ($\omega_p - \omega_q = \Delta_{ge}$) is satisfied, the nuclear spin could undergo Rabi oscillation between two states $|e\rangle$ and $|g\rangle$.

where $\delta = \omega_p - \omega_q - \Delta_{ge}$ is the detuning from perfect resonance. The ONQ coupling strength is

$$\mathscr{g}^{\mathrm{ONQ}} = \sum_{ij} \mathscr{D}_{ij} \langle e|I_i I_j|g\rangle \sim 10^2 \times \frac{2\pi \cdot \mathrm{MHz}}{(\mathrm{V/\AA})^2}, \tag{7.3}$$

where we have omitted the polarizations (p and q) of the electric fields.

From Eq. (7.2), one can see that when the frequency matching condition $\omega_p - \omega_q = \Delta_{ge}$ is satisfied, the ONQ effect can induce nuclear Rabi oscillation between $|e\rangle$ and $|g\rangle$, with a Rabi frequency of

$$f_{\mathrm{Rabi}} = |\mathscr{g}^{\mathrm{ONQ}} \mathscr{E}_p \mathscr{E}_q|. \tag{7.4}$$

Specifically, when $\mathscr{E}_p = \mathscr{E}_q = 10$ MV/m, one has $f_{\mathrm{Rabi}} = 100$ Hz, when can be significantly greater than the decoherence rate of single isolated nuclear spins [8, 9].

Notably, to realize the ONQ Rabi oscillation, one only needs

- nuclear spin with non-zero $\mathscr{D}$ tensor,
- two-color laser satisfying the frequency matching condition.

Therefore, the ONQ Rabi may serve as a proof-of-principle experiment for the ONQ

effect.

The frequency matching condition is actually a energy conservation condition - the excess energy of the two photons $\omega_p - \omega_q$ is absorbed (emitted) by the nuclear spin when it undergoes the $|g\rangle \rightarrow |e\rangle$ ($|e\rangle \rightarrow |g\rangle$) transition. This is similar to other NLO processes such as Raman scattering or difference frequency generation, whereby the excess energy of the two photons is absorbed (emitted) by a phonon or a third photon.

7.1.2 Readout of the Single Nuclear Spins State

To detect the quantum state of the single nuclear spin, one possible approach is to introduce an electron spin for readout [29, 48, 93] after the Rabi oscillation induced by the ONQ interaction is finished. This can be realized by ionizing/neutralizing the defect atom that hosts the single nuclear spin, which has been demonstrated in Refs. [29, 48]. This could serve as a proof-of-principle experiment of the ONQ effect in the short term.

In the long term, it might be desirable to totally get rid of electron spins and to develop an all-optical control over nuclear spins. One possible approach is to use high-quality optical cavities and high-efficiency single photon detectors. A single nuclear spin is put into an optical cavity resonant with the ω_p-photon and is pumped with a ω_q-laser. After the second-quantization of the ω_q-photon, the ONQ coupling would be

$$H_{\mathrm{ONQ}} = g^{\mathrm{ONQ}} \mathscr{E}_p \mathscr{E}_q^{\mathrm{zpf}} \left(|g\rangle\langle e| a_q^\dagger + h.c. \right), \tag{7.5}$$

where $h.c.$ stands for Hermitian conjugate, $b_q^\dagger$ is the creation operator of the ω_q-photon, and $\mathscr{E}_q^{\mathrm{zpf}} = \sqrt{\frac{\omega_q}{\varepsilon_r \varepsilon_0 V_q}}$ is the zero-point field of the ω_q-photon in the cavity with V_q the mode volume. When the nuclear spin is on excited state $|e\rangle$, then it can emit a ω_q-photon via the ONQ effect and jump back to $|g\rangle$. On the other hand, if the nuclear spin is on ground state $|g\rangle$, then the ω_q-photon would not be emitted. Hence, the state of the nuclear spin can be determined by detecting whether the ω_q-photon

is emitted using a single photon detector. The emission rate of the ω_q-photon is [94]

$$\begin{aligned} R &= \frac{4\left[g^{\mathrm{ONQ}}\mathscr{E}_p\mathscr{E}_q^{\mathrm{zpf}}\right]^2}{\kappa_q} \\ &= \frac{4[g^{\mathrm{ONQ}}\mathscr{E}_p]^2}{\varepsilon_r\varepsilon_0 V_q}Q_q, \end{aligned} \tag{7.6}$$

where κ_q is the decay rate, and $Q_q \equiv \frac{\omega_q}{\kappa_q}$ is the quality factor of the cavity. One can see that the emission rate R can be faster for a cavity with large quality factor and small mode volume.

In practice, optical cavities with quality factors above 10^{10} have been demonstrated [95, 96], and the mode volume can be down to 10^{-22} m^3 by nano-photonics design [97]. Using $Q_q = 10^{10}$ and $V_q = 10^{-22}$ m^{-3}, one has

$$R\ [\mathrm{Hz}] \approx 60 \times [\mathscr{E}_p]^2\ [\mathrm{MV/cm}]^2 \tag{7.7}$$

That is, one has $R = 60$ Hz when $\mathscr{E}_p = 1$ MV/cm. This is a relatively small emission rate, thus high efficiency single photon detected would be desired [98, 99]. Besides, it also requires an optical cavity that simultaneously has high Q-factor and small mode volume. This could be challenging as well. So we consider this all-optical readout of single nuclear spin as a long-term goal, which could be facilitated by the development of quantum/classical photonics.

7.2 Isotope Spectroscopy

In this section, we discuss how the ONQ effect can be used for isotope spectroscopy, yielding information on both the structure of the material and the type of the isotopes. The first approach is to detect the side peaks due to the ONQ scattering, similar to conventional Raman spectroscopy. Besides, the material imaging can be achieved by detecting the nuclear spin dynamics induced by the ONQ effect, similar to the NMR. Compare with other traditional spectroscopic techniques that rely on nuclear spins, such as NMR or nuclear quadrupole resonance (NQR), the ONQ spectroscopy uses

optical fields, instead of MW magnetic fields. This brings advantages such as higher temporal/spatial resolution - the temporal resolution of optical techniques can often be below picoseconds or even femtoseconds; The spatial resolution is limited only by the diffraction limit, and can be on the order of hundreds of nanometers.

In addition, the detection of the side peaks in the ONQ spectroscopy or the detection of the nuclear spin dynamics are relatively "classical" experiments, which do not touch too much the quantum properties of the nuclear spins. Hence, these two experiments should be relatively easier to demonstrate, and could serve as the proof-of-principle experiments of the ONQ effect.

7.2.1 Detect the Side Peaks

If nuclear spins are pumped by a laser with frequency ω_p, then electric fields (photons) with shifted frequency $\omega_p \pm \Delta_{ge}$ would be emitted, thanks to the ONQ effect. Notably, the frequency shift $\Delta_{ge} \propto \mathcal{q}\mathcal{V}$ is not the same for all nuclei, but depends on

- Type of isotope. For example, ^{69}Ga and ^{71}Ga have different quadrupole moment $\mathcal{q}$, and hence different $\Delta_{ge} \propto \mathcal{q}$ (Figure 7-2).

- Environment. For example, zinc blende GaAs has tetragonal symmetry, which enforces $\Delta_{ge} \propto \mathcal{V} = 0$. While wurtzite GaAs has relatively lower symmetry, leads to $\Delta_{ge} \neq 0$.

Besides, the intensity of the peak, which is proportional to $\mathcal{q}\mathcal{D}$, is also dependent on the two conditions above. Therefore, the ONQ effect provides information on both the type of the isotope and the environment (structure of the material).

Next, we analyse the experimental feasibility of the ONQ spectroscopy. Here we compare it with the Raman spectroscopy (Table 7.1), which is a prototypical technique relying on detecting the side-bands, i.e., the (anti)-Stokes peaks. For Raman spectroscopy, Raman-active vibrational modes are detected by measuring the frequency shift of the side bands.

We first consider the intensity of the side peaks. For Raman scattering, the

Table 7.1: Comparison between ONQ and Raman spectroscopy.

	Scattering rate per f.u.	Frequency shift	Linewidth
ONQ	$10^2 \times \frac{2\pi\cdot\text{MHz}}{(\text{V/Å})^2}$	MHz $\sim$ GHz	kHz
Raman	$10^5 \times \frac{2\pi\cdot\text{MHz}}{(\text{V/Å})^2}$	THz	sub-THz

coupling strength (per unit cell) with external electric field is

$$\begin{aligned} \not{g}^{\text{Raman}} &= \Delta\varepsilon\varepsilon_0 V_{\text{u.c.}} \\ &\sim 10^5 \times \frac{2\pi\cdot\text{MHz}}{(\text{V/Å})^2}, \end{aligned} \tag{7.8}$$

where $\Delta\varepsilon$ is the change in the relative permittivity when a single phonon (per unit cell) is excited, and is typically on the order of $10^{-3} \sim 10^{-2}$. $V_{\text{u.c.}}$ is the volume of a unit cell. As discussed before, the ONQ coupling strength (per nuclear spin) is on the order of $\not{g}^{\text{ONQ}} \sim 10^2 \times \frac{2\pi\cdot\text{MHz}}{(\text{V/Å})^2}$, which is smaller than $\not{g}^{\text{Raman}} \sim 10^5 \times \frac{2\pi\cdot\text{MHz}}{(\text{V/Å})^2}$ by three orders of magnitude [1]. This should not be a serious issue because the total intensity is proportional to the number of atoms (nuclear spins) participating in the interaction. Notably, Raman spectroscopy is applicable in gas phase or atomically-thin monolayer materials, which has a very limited number of atoms [100, 101]. Hence, if the ONQ spectroscopy is used on a three-dimensional solid-state material, which has a large number of atoms, then the intensity of the side peak would be significantly improved and should be detectable. Moreover, it is also possible to increase the intensity of the side peaks by using a stronger pumping laser. Finally, the linewidth (decay rate) of nuclear spins ($\sim$ kHz, see discussions below) is much smaller than that of phonons ($\sim$ THz), which could help increase the total ONQ transition rate, according to the Fermi's golden rule [102]. In summary, we believe that the intensity of the ONQ side peaks can be strong enough to be detectable in experiments.

Next, we consider the the frequency shift of the side peaks. For Raman spectroscopy, the frequency shift is usually on the order of THz (frequency of optical phonons). In comparison, the frequency shift in ONQ spectroscopy (Δ_{ge}) is on the

[1] Here we assum each unit cell contains one nuclear spin under consideration.

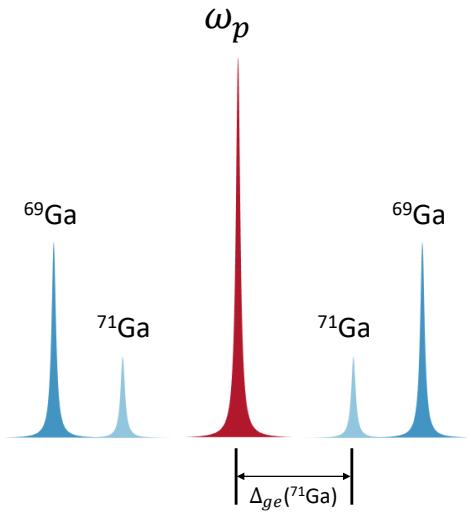

Figure 7-2: Mechanism of the isotopic spectroscopy using the ONQ effect. Under the pumping laser with frequency ω_p, side peaks with frequency $\omega_p \pm \Delta_{ge}(X)$ can be detected. $\Delta_{ge}(X)$ is dependent on both the type of the isotope and the chemical environment of the nuclei. Here we use ^{69}Ga and ^{71}Ga as an example. ^{69}Ga and ^{71}Ga have different quadrupole moment q_{69} and q_{71}, and their frequency shfit satisfies $\frac{\Delta_{ge}(^{69}\mathrm{Ga})}{\Delta_{ge}(^{71}\mathrm{Ga})} = \frac{q_{69}}{q_{71}}$

order of MHz $\sim$ GHz. Therefore, relatively high spectral resolution is required, which could be a challenge in practice. Fortunately, Raman-like spectroscopy with spectral resolution down to the sub-kHz level has been demonstrated experimentally [102].

Finally, we need to consider the linewidth of the side peaks - it should be smaller than the frequency shift of side peaks to be detectable. There are several contributions to the total line width

- Linewidth of the pumping laser, which can be below 1 kHz [103–108].
- The decay rate of nuclear spins, which can also be below 1 kHz.
- The broadening due to inhomogeneity, which can be orders of magnitude lower than Δ_{ge} in most situations. For example, our *ab initio* calculation indicates that a 1% strain only leads to a less than 10% change in Δ_{ge}.

In total, the linewidth of the side peaks can be kept far below the frequency shift Δ_{ge}, which is on the order of MHz $\sim$ GHz. Therefore, we believe the side peaks can be experimentally detectable.

7.2.2 Detect the Nuclear Spin Dynamics

The information of the materials can also be obtained by detecting the nuclear spin dynamics induced by the ONQ effect, using techniques developed in the NMR technology. This is because the nuclear dynamics induced by the ONQ and the NMR are essentially the same (Rabi oscillation, decay, etc.), so they can be detected using similar techniques, such as reading the total polarization of the spins. As an concrete example, in Ref. [70], the nuclear spin dynamics is induced by electric fields via the NER, and is detected by the optical time-resolved Kerr rotation technique.

7.3 Quantum Memory

Nuclear spins have long coherence time, and have been considered as ideal platform for quantum memory. On the other hand, optical photons can be carrier of quantum information in many scenario. The ONQ effect establishes an efficient interface between nuclear spins and optical photons. In this section, we demonstrate that via the ONQ effect, quantum information can be exchanged between optical photons and nuclear spins, and thus nuclear spins can be a quantum memory that stores the quantum information carried by optical photons.

7.3.1 Nuclear Spin Ensemble

Since the coupling strength between optical photons and a single nuclear spin is relatively weak, we resort to nuclear spin ensemble (NSE), which has been discussed in Section 6.2. As we will show below, the advantage of using NSE is that the total ONQ coupling strength can be enhanced by a factor of $\sqrt{N}$, where N is the number of nuclear spins interacting with optical photons simultaneously.

To facilitate following discussions, here we talk a bit more about the *ground* and *excited* states of the NSE. Without laser field, the *true* ground state of the NSE can be described as

$$|G\rangle = |g_1 g_2 g_3 \cdots g_N\rangle, \tag{7.9}$$

where all N nuclear spins are in the ground state $|g\rangle$. Actually, $|G\rangle$ is a state where the population of all nuclear magnon (NM) modes are zero.

The first excited state of the NSE is

$$|E\rangle = \sum_{\alpha} c_{\alpha} |g_1 g_2 \cdots g_{\alpha-1} e_{\alpha} g_{\alpha+1} \cdots g_N\rangle, \tag{7.10}$$

where the coefficients c_α satisfies $\sum_\alpha |c_\alpha|^2 = 1$. One can see that $|E\rangle$ corresponds to the state whereby a single NM is excited. In other words, one has

$$|E\rangle = a_k^\dagger |G\rangle. \tag{7.11}$$

The coefficients c_α are determined by the wavevector k. As discussed in Section 6.2, if we ignore the interaction between nuclear spins, and assume that the NSE is homogeneous, then the energy difference between $|G\rangle$ and $|E\rangle$ is $\Delta_{GE} = \Delta_{ge} = \omega_m$. Note that there could be excited states with even higher energy, such as

$$|E2\rangle = \sum_{\alpha\beta} c_{\alpha\beta} |g_\alpha g_\beta \cdots g_{\alpha-1} e_\alpha g_{\alpha+1} \cdots g_{\beta-1} e_\beta g_{\beta+1} \cdots g_N\rangle. \tag{7.12}$$

For $|E2\rangle$, two NMs are excited, that is, $|E2\rangle = a_k^\dagger a_{k'}^\dagger |G\rangle$.

A pre-requisite for any quantum memory is initialization. Actually, as we will show below, the NM mode (denote by a subscript m hereafter) that can interact with two-color photons is fixed by the requirement of energy and momentum conservation. Therefore, we only need to initialize the m-th mode, i.e., $n_m \to 0$. The m-th mode can be cooled down either thermally or by laser cooling, as we will discuss in Section 7.5. Note that even if $n_m = 0$, the population of other NM modes can still be non-zero. However, because other modes cannot interact with optical photons due to the violation of energy and/or momentum conservation, they would not influence the quantum memory application, except that they could influence the decoherence time of the m-th mode. In other words, $n_m = 0$ can be regarded as a *pseudo*-ground state, which is sufficient for quantum memory application, but it is not the *true* ground

state described by Eq. (7.9).

Here for exemplary purpose, we show that the initialization to the true ground state is possible if the quadrupole interaction is strong, which induces a large nuclear energy splitting. At sufficiently low temperatures, the probability for the NSE to be on $|G\rangle$ is

$$\begin{aligned} p_G &= \left[1+\exp\left(-\frac{\Delta_{ge}}{k_B T}\right)\right]^{-N} \\ &\approx 1 - N\exp\left(-\frac{\Delta_{ge}}{k_B T}\right), \end{aligned} \tag{7.13}$$

where T is the temperature and k_B is the Boltzmann constant. For certain systems, the energy splitting Δ_{ge} can be on the order of 1 GHz, equivalent to 50 mK. Thus, one has $p_G \approx 1-10^{-12}$ when $T = 1$ mK and $N = 10^{10}$, sufficient for practical applications.

7.3.2 Hyperfine Control over NSE

Previously, it has been demonstrate that electron spin can be used to control NSE through the hyperfine interaction [109–112]. Using hyperfine interaction to control nuclear spins has been extensively discussed in Sec. 3. Here we only discuss how the transition rate between $|\mathbb{0}\rangle$ and $|\mathbb{1}\rangle$ scales with N when a single electron spin is used to control the NSE. Here $|\mathbb{0}\rangle$ and $|\mathbb{1}\rangle$ are the number states of the NM mode that interacts with the electron. While other NM modes can have nonzero occupations, for brevity we set $|\mathbb{0}\rangle = |G\rangle$ in and $|\mathbb{1}\rangle = |E\rangle$ in Eqs. (7.9, 7.10). This would not change the essence of discussions below, as other NMs do not participate in the interaction with the electron spin.

The hyperfine Hamiltonian for the NSE is

$$\mathscr{H}^{\rm hf} = \sum_{\alpha} S\cdot \mathscr{A}^{\alpha}\cdot I^{\alpha}. \tag{7.14}$$

Note that here we have omitted Cartesian indices. As shown in Eqs. (2.4, 2.5), the strength of the hyperfine interaction $\mathscr{A}^{\alpha}$ is proportional to the wavefunction density ρ_S^{α} near the α-th nuclear site. If the electron needs to control N nuclear spins, then its wavefunction is shared by all nuclear spins. Consequently, one has $\mathscr{A}^{\alpha} \propto \rho_S^{\alpha} \propto \frac{1}{N}$,

and

$$\mathscr{H}^{\mathrm{hf}} = \frac{1}{N}\sum_{\alpha} S \cdot \mathscr{A}_0 \cdot I^{\alpha}, \tag{7.15}$$

where we assumed that the system is uniform, so $\mathscr{A}_0$ is the same for all nuclear spins. Then, the coupling strength between $|\mathbb{0}\rangle$ and $|\mathbb{1}\rangle$ via hyperfine interaction is

$$\begin{aligned}
\mathscr{G}^{\mathrm{hf}} &= \langle \mathbb{1}|\mathscr{H}_{\mathrm{hf}}|\mathbb{0}\rangle \\
&= \frac{1}{N}\sum_{\alpha\beta} c_\beta \langle g_1 g_2 \cdots g_{\beta-1} e_\beta g_{\beta+1} \cdots g_N | S \cdot \mathscr{A}_0 \cdot I^{\alpha} | g_1 g_2 g_3 \cdots g_N \rangle \\
&= \frac{1}{N}\sum_{\alpha\beta} c_\beta \mathscr{g}^{\mathrm{hf}} \delta_{\alpha\beta} \\
&= \frac{\mathscr{g}^{\mathrm{hf}}}{\sqrt{N}},
\end{aligned} \tag{7.16}$$

where we assume a uniform sample and hence $c_\alpha = \frac{1}{\sqrt{N}}$ on the last line. $\mathscr{g}^{\mathrm{hf}} = \langle e|S \cdot \mathscr{A}_0 \cdot I|g\rangle$ is the hyperfine coupling strength if the electron were to control a single nuclear spin. One can see that the coupling strength is inversely proportional to $\sqrt{N}$, i.e., it becomes weaker for a large NSE. Therefore, a key to realizing the electron spin control over NSE is to confine the electron wavefunction so that only a small NSE interacts with the electron spin. Indeed, in Refs. [110–112], only around 10^5 nuclear spins in a quantum dot are controlled simultaneously.

7.3.3 ONQ control over NSE

In this section, we discuss the ONQ control over NSE. First, we derive the ONQ coupling strength with NSE, using an approach similar to that in Section 7.3.2. When interacting with optical lasers, the ONQ Hamiltonian of a NSE is [cf. Eq. (7.2)]

$$\mathscr{H}^{\mathrm{ONQ}} = \mathscr{g}^{\mathrm{ONQ}} \mathscr{E}_p \mathscr{E}_q \sum_{\alpha} |e_\alpha\rangle\langle g_\alpha| + h.c. \tag{7.17}$$

The inhomogeneity in both the NSE and the laser field are ignored. Then the ONQ coupling strength of a NSE is

$$\begin{aligned}\mathscr{G}^{\mathrm{ONQ}} &= \langle \mathbb{1}|\mathscr{H}^{\mathrm{ONQ}}|\mathbb{0}\rangle \\ &= \sum_{\alpha\beta} c_\beta \langle g_1 g_2 \cdots g_{\beta-1} e_\beta g_{\beta+1} \cdots g_N| \left\{ \mathscr{g}^{\mathrm{ONQ}} |e_\alpha\rangle\langle g_\alpha| \right\} |g_1 g_2 g_3 \cdots g_N\rangle \\ &= \sum_{\alpha\beta} c_\beta \mathscr{g}^{\mathrm{ONQ}} \delta_{\alpha\beta} \mathscr{E}_p \mathscr{E}_q \\ &= \sqrt{N} \mathscr{g}^{\mathrm{ONQ}} \mathscr{E}_p \mathscr{E}_q .\end{aligned} \tag{7.18}$$

A Notably feature is the $\sqrt{N}$ amplification factor, which boosts the ONQ interaction when the NSE is large. Here $|\mathbb{0}\rangle$ and $|\mathbb{1}\rangle$ are the number states of the m-th NM mode, which participates in the interaction with the optical photons. We again used $|\mathbb{0}\rangle = |G\rangle$ in and $|\mathbb{1}\rangle = |E\rangle$ to simplify the expressions. Note again that in most situations only one NM mode can interact with optical photons because of the requirement of simultaneous conservation of both energy and momentum.

Next, we will derive the ONQ coupling between optical photons and the NM using a different approach. We start from the original ONQ Hamiltonian of the NSE, which is

$$\begin{aligned}\mathscr{H}_{\mathrm{ONQ}} &= \sum_\alpha H^\alpha_{\mathrm{ONQ}} \\ &= \sum_\alpha \sum_{ij} \left(\mathscr{D}^{pq}_{ij} \mathscr{E}^\alpha_p \mathscr{E}^\alpha_q I^\alpha_i I^\alpha_j + h.c. \right).\end{aligned} \tag{7.19}$$

Here the nuclei are labelled by α. $\mathscr{E}^\alpha_{p(q)}$ is the electric field at the site of the α-th nucleus.

Then, we transform the spin operators to boson creation/annihilation operators using the Holstein-Primakoff transformation, yielding $\sum_{ij} \mathscr{D}^{pq}_{ij} I^\alpha_i I^\alpha_j \approx \mathscr{g}^{\mathrm{ONQ}} (a^\dagger_\alpha + h.c.)$. Here we ignored some other higher-order terms that involve e.g. $a^\dagger_\alpha a_\alpha$ or $a^\dagger_\alpha a^\dagger_\alpha$ [cf. Eq (6.2, 6.3)], since they are off-resonance. This leads to

$$\mathscr{H}_{\mathrm{ONQ}} \approx \sum_\alpha \mathscr{g}^{\mathrm{ONQ}} \mathscr{E}^\alpha_p \mathscr{E}^\alpha_q \left(a^\dagger_\alpha + h.c. \right). \tag{7.20}$$

As we will discuss below, for the quantum memory application, the system is under the ω_p-pumping laser and is put into an optical cavity resonant with the ω_q-field. Consequently, we treat the ω_p-field as an external plane wave $\mathscr{E}_p^\alpha = \mathscr{E}_p e^{ik_p\cdot r_\alpha}$ with k_p the wavevector, and second-quantize the ω_q-field using $\mathscr{E}_q^\alpha = \mathscr{E}_q^{\rm zpf}\left(a_q^\dagger e^{-ik_q\cdot r_\alpha} + h.c.\right)$, where $\mathscr{E}_q^{\rm zpf}$ is the zero-point field of the ω_q-photon. We also perform the Fourier transformation for the $a_\alpha^\dagger$ (a_α) operators [cf. Eq. (6.6)], leading to

$$\begin{aligned}
\mathscr{H}_{\rm ONQ} &= \sum_\alpha \mathscr{g}^{\rm ONQ}\mathscr{E}_p\mathscr{E}_q^{\rm zpf} e^{ik_p\cdot r_\alpha}\left(a_q^\dagger e^{-ik_q\cdot r_\alpha} + h.c.\right)\frac{1}{\sqrt{N}}\sum_k\left(e^{-ik\cdot r_\alpha}a_k^\dagger + h.c.\right) \\
&= \frac{\mathscr{g}^{\rm ONQ}\mathscr{E}_p\mathscr{E}_q^{\rm zpf}}{\sqrt{N}}\sum_k\sum_\alpha\left\{e^{i(k_p-k_q-k)\cdot r_\alpha}a_q^\dagger a_k^\dagger + e^{i(k_p-k_q+k)\cdot r_\alpha}a_q^\dagger a_k + h.c.\right\} \\
&= \frac{\mathscr{g}^{\rm ONQ}\mathscr{E}_p\mathscr{E}_q^{\rm zpf}}{\sqrt{N}}\sum_k\left\{N\Delta(k_p-k_q-k)b_q^\dagger a_k^\dagger + N\Delta(k_p-k_q+k)a_q^\dagger a_k + h.c.\right\} \\
&= \mathscr{g}^{\rm ONQ}\sqrt{N}\mathscr{E}_p\mathscr{E}_q^{\rm zpf}\left\{a_q^\dagger a_m + a_q^\dagger a_m^\dagger + h.c.\right\}.
\end{aligned} \tag{7.21}$$

Here one can observe the $\sqrt{N}$ factor for the collective interaction between the optical photons and the NM. On the last line, we omitted the k subscript of the NM mode, but instead used m as the subscript. This is because due to the conservation of momentum, one has $k = \pm(k_q - k_q)$, and thus k is always close to the Γ-point in the Brillouin zone.

Finally, one should note that the frequency of the ω_q-photon is not arbitrary, but determined by conservation of energy. For the $a_q^\dagger a_m$ term, one has $\omega_q = \omega_h \equiv \omega_p + \omega_m$. For the $a_q^\dagger a_m^\dagger$ term, one has $\omega_q = \omega_l \equiv \omega_p + \omega_m$. We replace the subscript q with h and l accordingly, yielding

$$\mathscr{H}_{\rm ONQ} = \mathscr{g}^{\rm ONQ}\sqrt{N}\mathscr{E}_p\left\{\mathscr{E}_h^{\rm zpf}a_h^\dagger a_m + \mathscr{E}_l^{\rm zpf}a_l^\dagger a_m^\dagger + h.c.\right\}. \tag{7.22}$$

The collective coupling strength are

$$\begin{aligned}
\mathscr{G}_h &= \mathscr{g}^{\rm ONQ}\sqrt{N}\mathscr{E}_p\mathscr{E}_h^{\rm zpf}, \\
\mathscr{G}_l &= \mathscr{g}^{\rm ONQ}\sqrt{N}\mathscr{E}_p\mathscr{E}_l^{\rm zpf}.
\end{aligned} \tag{7.23}$$

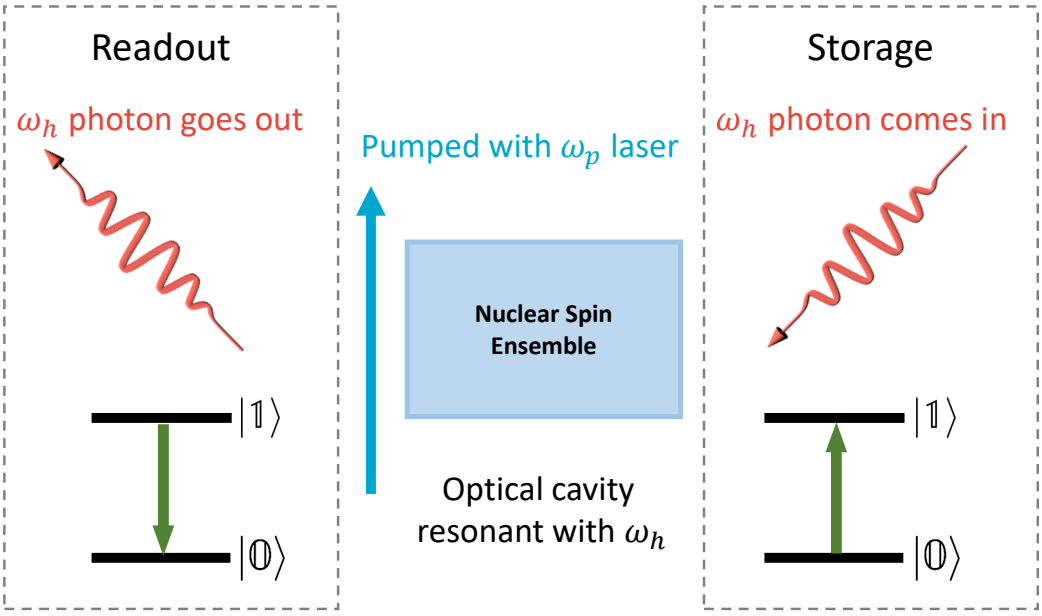

Figure 7-3: Illustration of the NSE quantum memory using the ONQ effect. The NSE is put inside an optical cavity with resonance frequency ω_p, and is pumped with the ω_q-laser. When a ω_p-photons comes into the cavity, the NSE can jump from $|\mathbb{0}\rangle$ to $|\mathbb{1}\rangle$ and memorize the ω_p-photon, via the ONQ interaction with the photon. This is the storage process. For readout, one detects whether a ω_p-photon can be emitted to determine the state of the NSE.

One can see that the total coupling strength is enhanced by a factor of $\sqrt{N}$, consistent with Eq. (7.18). This is in sharp contrast to the hyperfine coupling strength for a NSE in Eq. (7.16), which is proportional to $\frac{1}{\sqrt{N}}$. Therefore, using the ONQ effect, a relatively large number of nuclear spins can be controlled simultaneously, provided that the spot size and penetration depth of the pumping laser is large enough so that all the nuclear spins interact with the pumping laser efficiently. Specifically, the spot size and penetration depth of an off-resonance laser can be much greater than 1 μm, while a crystal sample with 1 μm size along each dimension contains $N \sim 10^{10}$ nuclear spins, considering that the number density of nuclear spins is typically on the order of $\rho \sim 10^{28}$ m^{-3} in pristine crystals.

7.3.4 Protocol of the NSE Quantum Memory

Next, we discuss the storage and readout protocol of the NSE Quantum memory, which is illustrated in Figure 7-3. Without loss of generality, we assume that the

photon carrying the quantum information has frequency ω_h [cf. Eq. (7.19)]. The NSE is put inside an optical cavity resonant with the ω_h-photon, and is pumped with the ω_p-laser.

$$\mathscr{H}^{\rm ONQ} = \mathscr{g}^{\rm ONQ}\sqrt{N}\mathscr{E}_q\mathscr{E}_h^{\rm zpf}a_h|\mathbb{1}\rangle\langle\mathbb{0}| + h.c. \tag{7.24}$$

Here for clarity we used $a_m^\dagger = |\mathbb{1}\rangle\langle\mathbb{0}|$ and only considered the beam-splitting term in Eq. (7.19). This is because for quantum memory we only need to consider the swap between a single photon and a single NM. Actually, the coupling strength of the squeezing term can be very small because the ω_h-cavity is off-resonance with the ω_l-photon [2]. In the ω_h-cavity, $\mathscr{E}_h^{\rm zpf}$ can be expressed as

$$\mathscr{E}_h^{\rm zpf} = \sqrt{\frac{\omega_h}{2\varepsilon_0 V_h}}, \tag{7.25}$$

where V_h is the mode volume of the ω_h-cavity. If $\omega_h = 1$ eV, $\mathscr{E}_p = 10$ MV/m, $N = 10^{10}$, and $V_h = 1\ \mu\text{m}^3$, then one has the coupling strength as

$$\mathscr{G}^{\rm ONQ} = \mathscr{g}^{\rm ONQ}\sqrt{N}\mathscr{E}_q\mathscr{E}_h^{\rm zpf} \sim 0.13\ \text{MHz}. \tag{7.26}$$

Considering that the quality factor of an optical cavity can reach 10^9 or even 10^{10} (see e.g., Refs. [96, 113, 114]), the linewidth of the optical photon in the cavity is $\kappa_h \sim 0.1$ MHz. One has the spontaneous transition rate can be estimated as

$$\mathscr{f}_{\rm spon} \sim \frac{\left[4\mathscr{G}^{\rm ONQ}\right]^2}{\kappa_h} \sim 0.6\ \text{MHz}, \tag{7.27}$$

which is far above the decoherence/decay rate of both the NSE and the photon.

For both storage and readout process, the NSE is put in the ω_h-cavity and pumped with the ω_p-laser. The storage process the ω_h-photon is as follows. The NSE is first initialized to $|\mathbb{0}\rangle$. When the ω_h-photon comes in, the NSE can absorb the ω_h-photon, and jump to $|\mathbb{1}\rangle$.

For readout, one possible approach is to detect whether a ω_h-photon is emitted to

[2] That is, $\mathscr{E}_l^{\rm zpf}$ is very small compared with $\mathscr{E}_h^{\rm zpf}$

determine the state of the NSE - If the NSE is in $|\mathbb{1}\rangle$, then it is possible to detect an outgoing ω_h-photon; if the NSE is in $|\mathbb{0}\rangle$, then one cannot detect the ω_h photon. The emission rate is in Eq. (7.27), which is a relatively high emission rate, and should be detectable by current single photon detectors [98, 99].

Another approach for the nondemolition measurement of the quantum state of the NSE, using the dispersive interaction [115–118] with an off-resonance anharmonic optical cavity. In this case, the ω_p-cavity is tuned off-resonance with the ONQ transition, i.e., $\delta \equiv \omega_p - \omega_q - \Delta_{GE} \neq 0$ [3]. Meanwhile, the cavity has an anharmonicity α, which could result from e.g., the interaction with an ancillary atom [119, 120] and can reach above 1 MHz. In this case, the resonance frequency of the cavity depends on the states of the NSE, and the shift in the resonance frequency is given by

$$\zeta \approx \frac{2\left[\mathscr{g}^{\mathrm{ONQ}}\sqrt{N}\mathscr{E}_q\mathscr{E}_h^{\mathrm{zpf}}o1\right]^2}{\delta}\frac{1}{1+\delta/\alpha}. \tag{7.28}$$

One has $\zeta \approx 30$ kHz when $\mathscr{E}_q = 0.1$ MV/cm, $\delta = 0.2$ MHz, and $\alpha = 1$ MHz. Such a ζ is resolvable considering that the linewidth of the cavity is around 24 kHz when $Q = 10^{10}$. Therefore, by detecting the shift in the resonance frequency of the cavity, one can indirectly probe the NSE state. This approach for detecting NSE state could be more challenging than the *resonant photon emission* approach described above, since introducing anharmonicity in the optical cavity could affect the properties of the NSE (e.g., coherence time) as well. Hence, the system needs to be carefully designed, which we leave as a future work.

7.3.5 Undesired Transitions

Finally, we would like to remark that besides the desired storage/readout transitions as described above, the NSE can do other undesired transitions as well. For example, when the NSE is in $|\mathbb{0}\rangle$ and is pumped with the ω_p-field, the NSE can spontaneously jump to $|\mathbb{1}\rangle$ and emit a photon with frequency $\omega_q - \omega_m$. However, the transition

[3] Δ_{GE} is energy difference between $|G\rangle$ and $|E\rangle$, as discussed in the main text

rate ℓ'_{spon} of such a process is strongly suppressed by the cavity resonance with the ω_h-field. Roughly, one has [96]

$$\frac{\ell'_{\text{spon}}}{\ell_{\text{spon}}} = \frac{\kappa_h^2}{4\omega_m^2 + \kappa_h^2}. \tag{7.29}$$

If $\omega_m = 2\pi \cdot \text{GHz}$ and $\kappa_h = 2\pi \cdot \text{MHz}$, one has $\frac{\ell'_{\text{spon}}}{\ell_{\text{spon}}} \sim 2.5 \times 10^{-7}$, which barely affects the fidelity of the quantum memory.

7.4 Quantum Transduction

As described in previous sections, through the ONQ effect, nuclear spins can be coupled to optical photons. On the other hand, nuclear spins can be coupled to microwave (MW) / radio frequency (RF) photons (denoted by a subscript r hereafter) via nuclear Zeeman interaction (Section 2.1). Consequently, nuclear spins can be the transducers between optical and MW/RF photons, which will be the focus of this section.

7.4.1 Transduction Hamiltonian

First we look at the transduction Hamiltonian, which involves both the ONQ interaction and the nuclear Zeeman interaction. Here we treat the ω_p-laser as the pumping field, and second quantize the ω_h and ω_r-photon. The transduction Hamiltonian of the combined system of nuclear spins, optical photons, and MW/RF photons is

$$\mathscr{H}^{r\leftrightarrow o} = \sum_{\alpha} \left\{ \frac{\delta}{2}(|e_\alpha\rangle\langle e_\alpha| - |g_\alpha\rangle\langle g_\alpha|) + \mathscr{g}^{\text{ONQ}} \mathscr{E}_h^{\text{zpf}} \mathscr{E}_p a_h^\dagger |g_\alpha\rangle\langle e_\alpha| + \gamma_N \mathscr{B}^{\text{zpf}} a_r^\dagger |g_\alpha\rangle\langle e_\alpha| + h.c. \right\}. \tag{7.30}$$

The frequency matching condition requires $\omega_h - \omega_p = \omega_r$. However, ω_r is detuned from the resonance frequency Δ_{ge} by $\delta = |\omega_r - \Delta_{ge}|$, which should be large enough to avoid the absorption of the MW/RF photons by the nuclear spins. $\mathscr{E}_h^{\text{zpf}} = \sqrt{\frac{\omega_h}{2\varepsilon_0 V_h}}$ is the zero-point electric field of the ω_h-photon as described before. $\mathscr{B}_r^{\text{zpf}} = \sqrt{\frac{\mu_o \omega_r}{2V_r}}$ is the zero-point magnetic field of the ω_r-photon, where μ_0 is the vacuum permeability.

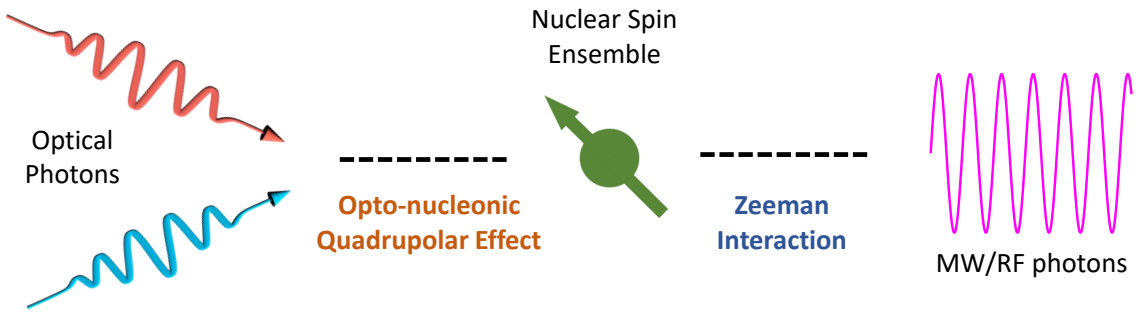

Figure 7-4: Illustration of the quantum transduction between optical and MW/RF photons using the ONQ effect. Nuclear spins interact with optical photons via the ONQ effect, and interact with MW/RF photons via the nuclear Zeeman interaction. The transduction between optical and MW/RF photons can be realized using nuclear spins as the media.

When the detuning is large enough, Eq. (7.30) can be re-written as

$$\mathscr{H}_{\text{eff}}^{r\leftrightarrow o} = \mathscr{G}_h a_h^\dagger |\mathbb{0}\rangle\langle\mathbb{1}| + \mathscr{G}_r a_r^\dagger |\mathbb{0}\rangle\langle\mathbb{1}| + h.c. \tag{7.31}$$

Here we have ignored the inhomogeneity in nuclear spins. The first (second) term describes the collective interaction between the NSE and the optical (MW/RF) photon. The collective coupling strength are

$$\begin{aligned} \mathscr{G}_h &= \mathscr{g}^{\text{ONQ}} \sqrt{N} \mathscr{E}_p \mathscr{E}_h^{\text{zpf}}, \\ \mathscr{G}_r &= \gamma_N \sqrt{N} \mathscr{B}_r^{\text{zpf}}. \end{aligned} \tag{7.32}$$

Before further analyses, we estimate the magnitude of $\mathscr{G}_h$ and $\mathscr{G}_r$ achievable in experiments. We assume $\omega_h = 1$ eV and $\omega_r = 2\pi \cdot 1$ GHz. We also assume $N = \rho V_h$, where the number density of nuclear spins is $\rho \sim 10^{28}$ m^{-3}. This leads to $\mathscr{G}_h \approx 2.4$ MHz when $\mathscr{E}_p = 1.8$ MV/cm. As for $\mathscr{G}_r$, we assume that the mode volume of the MW/RF cavity to be $V_r = 1$ mm^3, then one has $\mathscr{G}_r \sim 0.3$ MHz when $N \sim 10^{18}$, corresponding to a crystal with 0.1 mm^3 size. Note that MW/RF cavities with even smaller mode volume are achievable [121].

7.4.2 Adiabatical Elimination and Input-Output Formalism

In the limit of large detuning $\delta \gg \mathcal{G}_h, \mathcal{G}_r$, one can adiabatically eliminate the nuclear spins dynamics in Eq. (7.31), and arrive at

$$\mathcal{H}_{\text{ad}}^{r\leftrightarrow o} = \mathcal{G}_{hr} a_h^\dagger a_r + h.c. \tag{7.33}$$

where

$$\mathcal{G}_{hr} = \frac{\mathcal{G}_h \mathcal{G}_r}{\delta} \tag{7.34}$$

is the effective coupling strength between optical and MW/RF photons. Then the transduction efficiency can be estimated using the input-output formalism [122, 123]. Specifically, the Quantum Langevin equation for the optical and MW/RF fields are

$$\begin{aligned} \frac{da_h}{dt} &= -i\mathcal{G}_{hr} a_r - \frac{\kappa_h}{2} a_h - \sqrt{\kappa_h} a_h^{\text{in}}, \\ \frac{da_r}{dt} &= -i\mathcal{G}_{or}^* a_h - \frac{\kappa_r}{2} a_r - \sqrt{\kappa_r} a_r^{\text{in}}, \end{aligned} \tag{7.35}$$

where κ_h and κ_r are the cavity decay rate of the optical and MW/RF photons, respectively. a_h^{in} and a_r^{in} are the input fields. Transforming to the frequency domain, Eq. (7.35) becomes algebraic equations, which yield

$$\begin{aligned} a_h^{\text{out}}(\omega) &= \frac{4i\mathcal{G}_{hr}\sqrt{\kappa_h\kappa_r}}{4|\mathcal{G}_{hr}|^2 + (\kappa_h - 2i\omega)(\kappa_r - 2i\omega)} a_r^{\text{in}}(\omega) + \frac{4|\mathcal{G}_{hr}|^2 - (\kappa_h + 2i\omega)(\kappa_r - 2i\omega)}{4|\mathcal{G}_{hr}|^2 + (\kappa_h - 2i\omega)(\kappa_r - 2i\omega)} a_h^{\text{in}}(\omega), \\ a_r^{\text{out}}(\omega) &= \frac{4i\mathcal{G}_{or}^*\sqrt{\kappa_h\kappa_r}}{4|\mathcal{G}_{hr}|^2 + (\kappa_h - 2i\omega)(\kappa_r - 2i\omega)} a_h^{\text{in}}(\omega) + \frac{4|\mathcal{G}_{hr}|^2 - (\kappa_h - 2i\omega)(\kappa_r + 2i\omega)}{4|\mathcal{G}_{hr}|^2 + (\kappa_h - 2i\omega)(\kappa_r - 2i\omega)} a_r^{\text{in}}(\omega). \end{aligned} \tag{7.36}$$

The conversion efficiency between optical and MW/RF fields is

$$\begin{aligned} \eta(\omega) &\equiv \left| \frac{a_h^{\text{out}}(\omega)}{a_r^{\text{in}}(\omega)} \right|^2 = \left| \frac{a_r^{\text{out}}(\omega)}{a_h^{\text{in}}(\omega)} \right|^2 \\ &= \left| \frac{4i\mathcal{G}_{hr}\sqrt{\kappa_h\kappa_r}}{4|\mathcal{G}_{hr}|^2 + (\kappa_h - 2i\omega)(\kappa_r - 2i\omega)} \right|^2. \end{aligned} \tag{7.37}$$

The frequency matching condition $\omega_h - \omega_p = \omega_r$ corresponds to $\omega = 0$ in Eqs. (7.36, 7.37). In this case, unity transduction efficiency $\eta(\omega = 0) = 1$ can be achieved when

$$\Gamma \equiv \frac{2|\mathcal{G}_{hr}|}{\sqrt{\kappa_h \kappa_r}} = 1. \tag{7.38}$$

This condition is also called the impedance matching condition.

As discussed in the previous section, $\mathcal{G}_h = 2.4$ MHz and $\mathcal{G}_r = 0.3$ MHz can be achievable in experiments. Here we also need to examine the photon loss rates κ_h and κ_r. For optical cavities, the quality factor can reach over 10^9 [96,113,114], equivalent to $\kappa_h = 0.24$ MHz for $\omega_h = 1$ eV. For MW/RF cavities, the quality factor can reach 10^5 [124], equivalent to $\kappa_r = 0.01$ MHz when $\omega_r = 1$ GHz. Under these conditions, $\Gamma = 1$ is achieved when the detuning is $\delta \approx 30$ MHz, satisfying the $\delta \gg \mathcal{G}_h, \mathcal{G}_r$ condition required for the adiabatical elimination.

7.4.3 Master Equation Simulations

The adiabatical elimination in Eq. (7.33) provides an easy approach for estimating the transduction efficiency. However, it has a major drawback - the dynamics of the transducers (nuclear spins here) are completely ignored. This is not a good assumption, especially when the dynamics, including the decay rate of the transducers are fast.

To demonstrate how the dynamics of nuclear spins affect the transduction efficiency, we adopt the master equation approach. The master equation can be expressed as

$$\frac{d\rho}{dt} = -i[\mathscr{H}_{\text{eff}}^{r\leftrightarrow o}, \rho] + \kappa_h \zeta(a_h) + \kappa_m \zeta(\sigma^-) + \kappa_r \zeta(a_r), \tag{7.39}$$

where $\mathscr{H}_{\text{eff}}^{r\leftrightarrow o}$ is the full transduction Hamiltonian as shown in Eq. (7.31), ρ is the density matrix of the total system, and

$$\zeta(o) = o\rho o^\dagger - \frac{1}{2}\left(o^\dagger o\rho - \rho o^\dagger o\right) \tag{7.40}$$

is the Lindblad operator of a certain operator o. $\sigma^- \equiv |\mathbb{0}\rangle\langle\mathbb{1}|$. Here we only considered

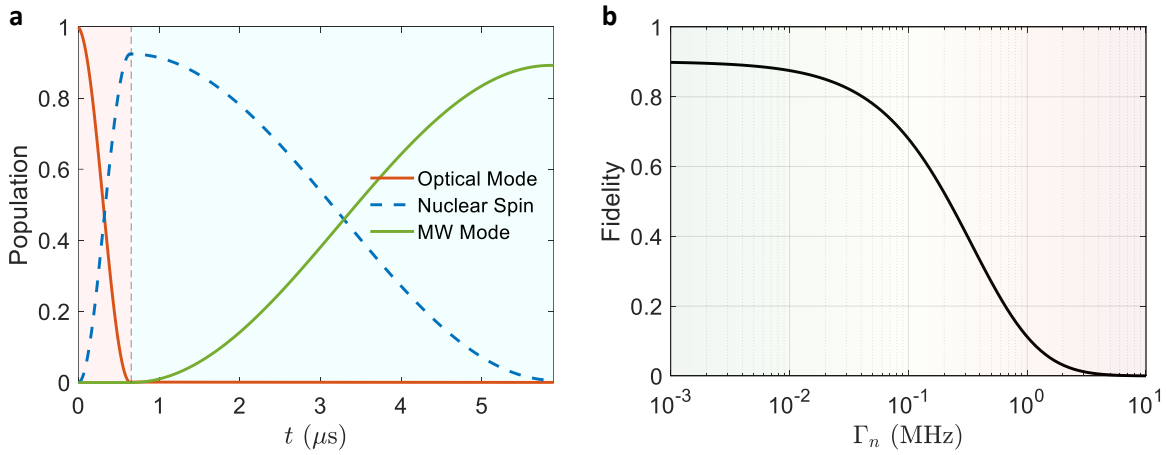

Figure 7-5: Numerical simulation of the optical to MW/RF transduction process using the master equation. (a) Time evolution of the populations of different subsystems (optical photon, nuclear spins, and MW/RF photon). Here we take $\kappa_m = 0.01$ MHz. (b) Fidelity of the optical to MW/RF transition as a function of NSE dissipation rate κ_m. In the simulations we take $\mathcal{G}_h = 2.4$ MHz and $\mathcal{G}_r = 0.3$ MHz, as discussed in the main text.

the relaxation of the nuclear spins, and the decoherece effect is ignored, which makes marginal influence on the transduction process, according to our numerical tests.

There are various protocols to implement the transduction between optical and MW/RF photons. Here we consider a simple protocol using sequential swap gates [125, 126]. For clarity, we use the optical to MW/RF transduction as an example. The reverse MW/RF to optical transduction can be studied similarly. The protocol is as follows. When an optical photon comes in, it is stored in the resonant optical cavity and interacts with the nuclear spins for a certain amount of time that leads to a $|\mathbb{0}\rangle \to |\mathbb{1}\rangle$ transition of the NSE, which is a swap process. During this period of time, the MW/RF cavity is detuned, and the interaction between nuclear spins and MW/RF photons are off. Then one turns on the interaction between MW/RF photons and nuclear spins, and detunes the resonance frequency of optical cavity so that optical photons can be decoupled. In this case, the nuclear spin transitions leads to the emission of the MW/RF photon via the ONQ effect. In Figure 7-5, we show that such a simple swap protocol could yield a transduction fidelity around 90 % with parameters described around Eq. (7.38).

Next, we demonstrate how the decoherence of nuclear spins can affect the trans-

duction efficiency. From Figure 7-5(b), one can see that the transduction fidelity significantly deteriorates when $\kappa_m \gtrsim 0.1$ MHz. Fortunately, nuclear spins are immune to external perturbations, and κ_m as low as kHz is readily achievable.

7.5 Laser Cooling of Nuclear Magnons

Nuclear spin is one of the hardest substances to cool down. As discussed before, the gyromagnetic ratio of nuclei is typically on the order of $10 \times \frac{2\pi \cdot \text{MHz}}{\text{T}}$. Hence, under a 2 T magnetic field, the nuclear spin splitting is only 20 MHz, equivalent to 1 mK. On the other hand, the ^{3}He/^{4}He dilution refrigerators usually can only reach around 2 mK [127], whereby the nuclear spin has $\sim 38\%$ probability to be on the excited state, hindering various applications of nuclear spins. One possible approach to avoid this problem is to use nuclear spins with large quadrupole interaction, where the nuclear spin splitting can reach ~ 1 GHz, equivalent to 50 mK (see e.g., Sec. 7.3.4). However, nuclei with large quadrupole interaction are not viable for all applications.

Can we further cool down nuclear spins with lasers? At first sight, one may expect that under laser illumination, substances would be heated up because they can absorb energy from the laser. Somewhat intuitively, laser can actually cool down objects. Laser cooling of atoms and molecules using the Doppler effect [128–130] has been proposed and realized almost half-century ago. In recent years, laser cooling of quasiparticles such as phonons [131], excitons [132], and electron magnons [133] has also been proposed and/or realized using different techniques/mechanims. In this section, we will show that the ONQ effect can enable the laser cooling of nuclear magnons under feasible experimental conditions.

7.5.1 Laser Cooling/Heating Scheme

The eigenstates of the NM Hamiltonian Eq. (6.8) are the number states $|n\rangle$, whereby n NMs are excited. Under the pumping laser ω_p, NMs can be created (annihilated) due to the ONQ interaction, which can be described by the ONQ Hamiltonian [cf.

Eq. (7.21), see also Ref. [134]]

$$\mathscr{H}_m^{\mathrm{ONQ}} = \mathscr{G}_h a_m^\dagger a_h + \mathscr{G}_l a_m^\dagger a_l^\dagger + h.c. \tag{7.41}$$

where

$$\mathscr{G}_{h(l)} = \mathscr{g}^{\mathrm{ONQ}} \sqrt{N} \mathscr{E}_p \mathscr{E}_{h(l)}^{\mathrm{zpf}} \tag{7.42}$$

is are the coupling strengths.

Possible transitions of the NM mode are illustrated in Figure 7-6. Here Green (red) arrows correspond to the first (second) term in Eq. (7.41). For laser cooling, one needs $\mathscr{G}_h \gg \mathscr{G}_l$ [131], whereby the second term in Eq. (7.41) (red arrows) can be ignored. The solid and dashed green arrows indicate two reverse processes: The solid green arrows indicate the $\omega_p + \omega_m \to \omega_h$ process, which annihilates and cools down NMs; The dashed green arrows correspond to the reverse $\omega_h \to \omega_p + \omega_m$ transition, which creates and heats-up NMs (back-heating effect). Usually the back-heating can be minimal if the ω_h-photon has a small population. The grey curved lines denote the interactions between NMs/photons and the heat bath. On the other hand, the laser heating of NMs can be achieved when $\mathscr{G}_l \gg \mathscr{G}_h$, whereby the first term in Eq. (7.41) (green arrows) can be ignored.

In the rotating frame of ω_p, one has the Hamiltonian of the combined system of ω_h-photons and NMs as

$$\mathscr{H}_C = \omega_m a_m^\dagger a_m + (\omega_h - \omega_p) a_h^\dagger a_h + \left(\mathscr{G}_h a_h^\dagger a_m + h.c. \right). \tag{7.43}$$

Here we used the condition of $\mathscr{G}_h \gg \mathscr{G}_l$, which can be realized by e.g., using an optical cavity resonant with the ω_h-photon. In this case, one has $\mathscr{E}_h^{\mathrm{zpf}} = \sqrt{\frac{\hbar\omega_h}{2\varepsilon_0 V_h}}$, where V_h is the mode volume of the ω_h-cavity. As estimated before, one has $\mathscr{G}_h[\mathrm{kHz}] \approx 1.9 \times \mathscr{E}_p[\mathrm{MV/m}]$, that is, a 1 MV/m pumping field leads to a collective ONQ coupling strength of around 1.9 kHz.

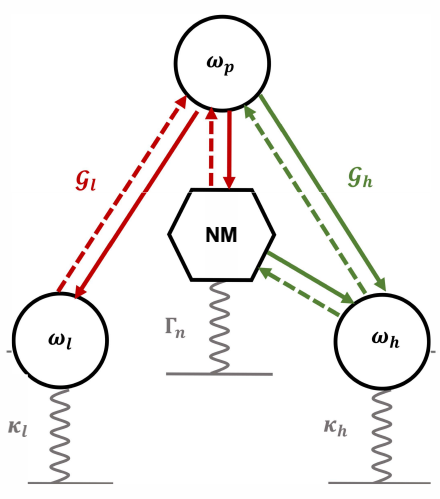

Figure 7-6: Scheme of the laser cooling/heating process. Circles denote photons whose frequencies are marked inside the circle. The hexagon denotes the NM. Arrows denote possible ONQ transitions, while the grey wavy lines indicate the coupling with the heat bath.

7.5.2 Dynamics of the Laser Cooling Process

The dynamics of the laser cooling process can be described by the master equation

$$\frac{d\rho}{dt} = -i[\mathscr{H}_C, \rho] + \kappa_h \zeta(a_h) + \kappa_m (n_{\text{th}} + 1)\zeta(a_m) + \kappa_m n_{\text{th}} \zeta(a_m^\dagger), \tag{7.44}$$

where κ_h and κ_m are the decay rates of the ω_h-photon and the NM, respectively, while

$$n_{\text{th}} = \frac{1}{\exp\left(\frac{\omega_m}{k_B T}\right) - 1} \tag{7.45}$$

is the thermal population of the nuclear magnon. Considering that ω_m can reach tens of MHz, while T can be mK in a dilute refrigerator, we fix $n_{\text{th}} = 1$ for following discussions. The thermal occupation of the ω_h-photon is ignored since $\omega_h \gg k_B T$.

The laser cooling behavior is characterized by two parameters

$$\frac{\mathcal{G}_h}{\kappa_m} \quad \text{and} \quad \frac{\mathcal{G}_h}{\kappa_h} \tag{7.46}$$

κ_m is usually in the sub-kHz range (Section 6.2.2), while $\mathcal{G}_h$ can be well above 1 kHz.

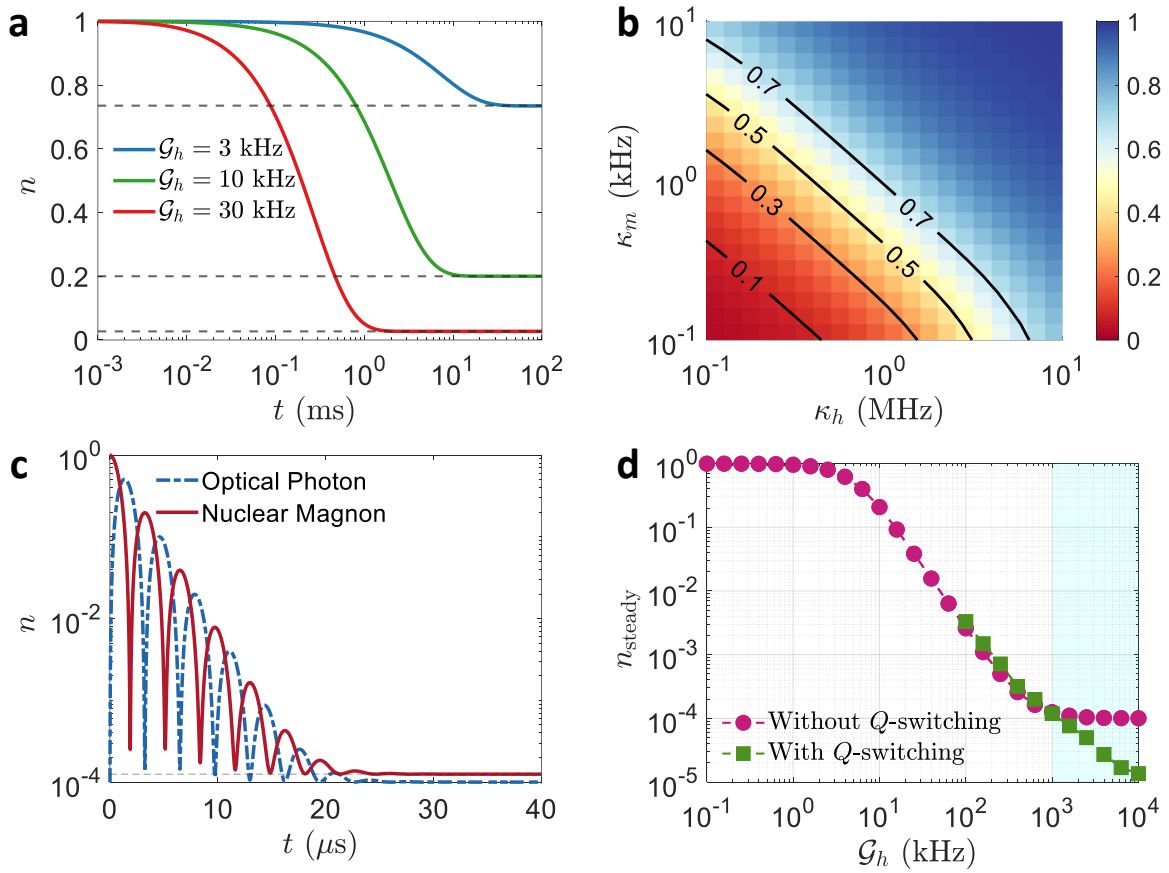

Figure 7-7: Numerical simulation of the laser cooling of nuclear magnon using the ONQ effect. (a) Time evolution of $n_m(t)$ in the weak-coupling regime ($\mathcal{G}_h/\kappa_h \ll 1$. (b) The steady state NM occupation n_{steady} as a function of dissipation rates κ_m and κ_h in the weak-coupling regime. Here we set $\mathcal{G}_h = 10$ kHz. (c) Time evolution of $n_m(t)$ and $n_h(t)$ in the strong coupling regime. Here we set $\mathcal{G}_h = 1$ MHz. (d) n_{steady} as a function of $\mathcal{G}_h$ in both weak and strong-coupling regime. The strong-coupling regime is mark in cyan. The red (green) curve denotes laser cooling without (with) switching the Q-factor of optical cavity. In (a, c, d), $\kappa_m = 0.1$ kHz and $\kappa_h = 1$ MHz are used.

Hence, we are in the "strong-coupling" ($\frac{\mathcal{G}_h}{\kappa_m} \geq 1$) regime regarding the dissipation of NMs. On the other hand, κ_h can be kept below MHz considering that a quality factor Q_h on the order of $10^9 \sim 10^{10}$ has been realized in optical cavities.

Weak-Coupling Regime

We first consider the weak-coupling regime ($\frac{\mathcal{G}_h}{\kappa_h} < 1$). We first fix $\kappa_m = 0.1$ kHz and $\kappa_h = 1$ MHz. In Figure 7-7(a), the occupation number of the NM mode $n_m(t)$ is plotted against time for $\mathcal{G}_h = 3, 10$, and, 30 kHz, respectively. One can see that $n_m(t)$ monotonically decays with time until reaching a steady value (Section 7.5.3), which is denoted by the dashed horizontal lines in Figure 7-7(a). Specifically, with $\mathcal{G}_h = 10$ kHz (30 kHz), one has $n_{\text{steady}} \approx 0.20$ (0.027), smaller by a factor of 5 (37) as compared with n_{th}. Note that the occupation number n_h of the ω_h-photon is very small during the whole process (Figure 7-8, Section 7.5.3) because of its fast decay rate $\kappa_h \gg \mathcal{G}_h$.

Next, we fix $\mathcal{G}_h = 10$ kHz, corresponding to $\mathcal{E}_p \approx 5$ MV/m. In this case, n_{steady} as a function of κ_m and κ_h is shown in Figure 7-7(b). One can see that sizable cooling effect exists even when $\kappa_m = 1$ kHz and $\kappa_h = 1$ MHz.

Strong Coupling Regime

Next, we switch to the strong-coupling regime and set $\mathcal{G}_h = 1$ MHz [Figure 7-7(c)]. In this case, $n_m(t)$ and $n_h(t)$ exhibit oscillating dynamics - ω_h-photon and the NM swaps with each other with a frequency of $2\mathcal{G}_h$. Notably, the magnitude of the total occupation $(n_m + n_h)$ continuously decreases with an envelope function $e^{-\bar{\kappa}t}$. The overall decay rate is

$$\bar{\kappa} = \frac{1}{2}(\kappa_m + \kappa_h). \tag{7.47}$$

This is because approximately the NM and the ω_h-photon mode each exists for half of the time t during the swap process. Finally, n_{steady} reaches $\sim 10^{-4}$, smaller than n by a factor of 10^4.

7.5.3 Steady State Occupation of the NMs

During the laser cooling process, the NMs are coupled to the ω_h-photons via the ONQ effect, which is described by Eq. (7.22). The *reduced* transition rate between NMs and ω_h-photons can be obtained from the Fermi's golden rule

$$\begin{aligned}\mathscr{K} &= 2\pi \mathscr{G}_h^2 \rho_f \\ &= 2\pi \mathscr{G}_h^2 \frac{2}{\pi} \frac{\kappa_h}{4(\omega_m - \omega_h)^2 + \kappa_h^2} \\ &\xrightarrow{\omega_m = \omega_h} \frac{4\mathscr{G}_h^2}{\kappa}.\end{aligned} \tag{7.48}$$

Here ρ_f is the density of states of the final states. On the second line, we assume that the density of states of the ω_h-photon in the optical cavity is a Lorentzian function with linewidth κ_h. On the last line, we set $\omega_m = \omega_h$, which is the resonance condition.

For bosons, the *total* transition rate depends on the occupation number as well. For example, the total transition rate of $\omega_p + \omega_m \to \omega_h$ is

$$f_1 = \mathscr{K} n_m (n_h + 1), \tag{7.49}$$

where n_m and n_h are the occupation number of the NM and the ω_h-photon, respectively. Similarly, the total transition rate of $\omega_h \to \omega_p + \omega_m$ is

$$f_2 = \mathscr{K} (n_m + 1) n_h. \tag{7.50}$$

Note that the ω_p-field is treated as a classical field. In other words, the number of ω_p-photons is implicitly represented by the electric field strength $\mathscr{E}_p$, which is incorporated in the $\mathscr{C}$ factor [cf. Eqs. (7.23, 7.48)].

Meanwhile, the NMs and the ω_h-photons are coupled to the heat bath with a coupling rate of κ_m and κ_h, respectively. This leads to additional transitions. For the NM, we have

- Absorption of NMs from the heat bath, with a transition rate $f_3 = \kappa_m n_{\text{th}} (n_m + 1)$;

- Emission of NMs to the heat bath, with transition rate $f_4 = \kappa_m(n_{\rm th}+1)n_m$;

Under the ONQ coupling with the ω_h-photon and the coupling with the heat bath, there are four transitions involving NMs, which are described above. The steady state NM occupation $n_m^{\rm steady}$ can be obtained by balancing all the four transitions above (i.e., $f_1 + f_4 = f_2 + f_3$), leading to

$$\mathscr{K}(n_m^{\rm steady}+1)n_h^{\rm steady} + \kappa_m n_{\rm th}(n_m^{\rm steady}+1) = \mathscr{K} n_m^{\rm steady}(n_h^{\rm steady}+1) + \kappa_m(n_{\rm th}+1)n_m^{\rm steady}, \tag{7.51}$$

where $n_m^{\rm steady}$ are $n_h^{\rm steady}$ are the steady-state occupation of the NM and the ω_h-photon, respectively. A similar equation can be obtained by balancing the transitions involving the ω_h-photon, which is

$$\mathscr{K} n_{\rm steady}(n_h^{\rm steady}+1) = \kappa_h n_h^{\rm steady} + \mathscr{K}(n_{\rm steady}+1)n_h^{\rm steady}, \tag{7.52}$$

where we used the fact that the thermal occupation of the ω_h-photon is zero. Eqs. (7.51, 7.52) yield

$$\begin{aligned} n_m^{\rm steady} &= n_{\rm th}\frac{\kappa_m(\mathscr{K}+\kappa_h)}{(\kappa_m+\kappa_h)\mathscr{K}+\kappa_m\kappa_h}, \\ n_h^{\rm steady} &= n_{\rm th}\frac{\kappa_m\mathscr{K}}{(\kappa_m+\kappa_h)\mathscr{K}+\kappa_m\kappa_h}. \end{aligned} \tag{7.53}$$

In the weak-coupling regime, Eq. (7.53) reduces to

$$\begin{aligned} n_m^{\rm steady} &\approx n_{\rm th}\frac{\kappa_m\kappa_h}{4\mathscr{G}_h^2+\kappa_m\kappa_h}, \\ n_h^{\rm steady} &\approx 0, \end{aligned} \tag{7.54}$$

which are used in the main text. Actually, the occupation of the ω_h-photon is very small during to whole laser-cooling process in the weak-coupling regime, as shown in Figure 7-8.

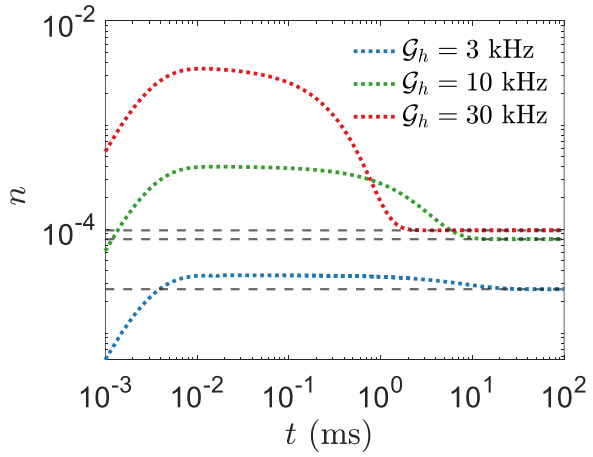

Figure 7-8: Time evolution of the occupation number of the ω_h-photon in the weak-coupling regime. The horizontal dashed lines indicate the steady state occupation calculated from Eq. (7.53). Here $\kappa_h = 1$ MHz, $\kappa_m = 0.1$ kHz.

7.5.4 Q-switching

Interestingly, in the strong-coupling ($\frac{\mathcal{G}_h}{\kappa_h} \geq 1$) regime, further increasing $\mathcal{G}_h$ does not help improve the cooling effect [red curve in Figure 7-7(d)]. Actually, n_{steady} becomes a constant [cf. Eq. (7.53)]

$$n_{\text{steady}} = \frac{\kappa_m}{\kappa_h} n_{\text{th}}. \tag{7.55}$$

This effect also appears in the case of optical cooling of mechanical modes [135–137]. Fortunately, this limitation can be avoided by Q-switching [138] - When $n_h(t)$ reaches its maximum, one abruptly increases κ_h. This results in the quick decay of the ω_h-photons and the suppression of the back-heating effect (Figure 7-9). With Q-switching, the NM mode can be further cooled down when $\frac{\mathcal{G}_h}{\kappa_h} \geq 1$ (green curve in Figure 3d).

7.5.5 Entropy of the NM system

Similar to occupation number, entropy is another important parameter for various applications. Here we show that during the laser cooling process, the entropy of the NM system is also suppressed.

For a non-interacting boson mode whose chemical potential is zero and energy is

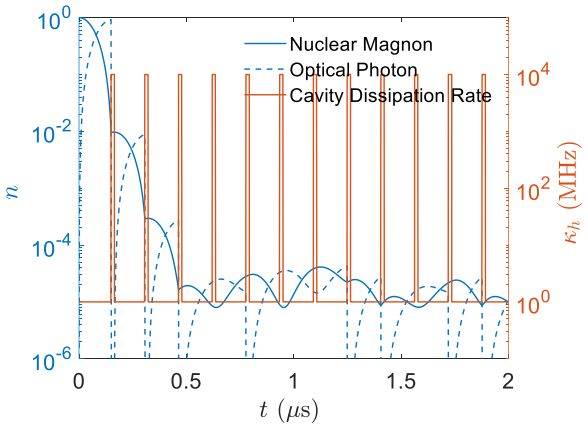

Figure 7-9: Dynamics of laser cooling with Q-switching. The cavity dissipation rate is abruptly increased when $n_h(t)$ reaches its maximum. $\mathcal{G}_h = 10$ MHz.

ω, its entropy at thermal equilibrium is

$$S_{\text{th}} = -\ln(\alpha - 1) + \frac{\alpha \ln \alpha}{\alpha - 1}, \tag{7.56}$$

where $\alpha = \exp\left(\frac{\omega}{k_B T}\right)$, with T as the temperature and k_B as the Boltzmann constant. α is related to the thermal occupation number as

$$n_{\text{th}} = \frac{1}{\alpha - 1}. \tag{7.57}$$

Eqs. (7.56, 7.57) leads to

$$S_{\text{th}} = S_{\text{th}}(n_{\text{th}}), \tag{7.58}$$

that is, S_{th} is determined by n_{th}.

Figure 7-10, shows the time evolution of the von Neuman entropy S_{vn} of the NM mode during the laser cooling process. When $t < 0$, the NM mode is only coupled to the thermal bath. One can see that $S_{\text{vn}} = S_{\text{th}}(n_{\text{th}})$ is a constant when $t < 0$, as expected.

At $t = 0$, the laser cooling is turned on, and S_{vn} starts to decrease with time, until a steady value $S_{\text{vn, steady}}$. Interestingly, one has

$$S_{\text{vn, steady}} \approx S_{\text{th}}(n_{\text{steady}}). \tag{7.59}$$

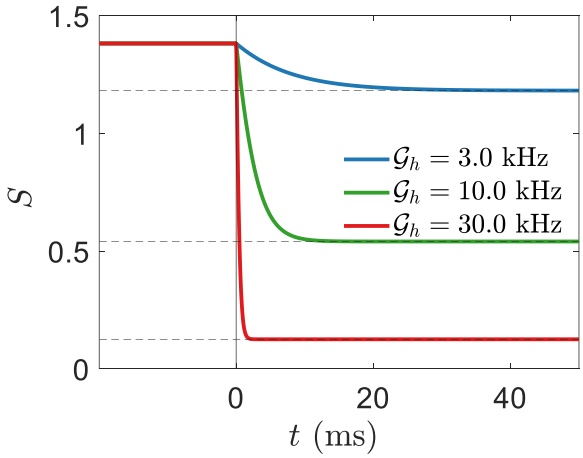

Figure 7-10: Time evolution of the von Neumann entropy $S_{\rm vn}$ of the NM mode during the laser cooling process. The laser cooling is turned on at $t = 0$. The horizontal lines indicate $S_{\rm th}(n_{\rm steady})$. Here $\kappa_h = 1$ MHz, $\kappa_m = 0.1$ kHz.

$S_{\rm th}(n_{\rm steady})$ is denoted by the horizontal lines in Figure 7-10. One can see that after the laser cooling, the entropy of the NM system resembles that of an equilibrium thermal system whose occupation number is $n_{\rm steady}$.

7.5.6 Laser Heating of NMs

For laser heating of NM modes, the optical cavity should be red-detuned to be resonant with the ω_l-photon, so that one has $\mathcal{G}_l \gg \mathcal{G}_h$. In this case, the combined Hamiltonian of the NM and the ω_l-photons is

$$\mathscr{H}_H = \omega_m a_m^\dagger a_m + (\omega_l - \omega_p) a_l^\dagger a_l + \left(\mathcal{G}_l a_l^\dagger a_m^\dagger + h.c.\right) \tag{7.60}$$

For laser heating, the parameter $\frac{4\mathcal{G}_l^2}{\kappa_m \kappa_l}$ plays a crucial role.

Weak-Coupling Regime

If $\frac{4\mathcal{G}_l^2}{\kappa_m \kappa_l} < 1$, the population of NM $n_m(t)$ increases with time, until reaching a steady number [Figure 7-11(a)]

$$n_m^{\rm steady} = \frac{n_{\rm th}\kappa_m\kappa_l + 4\mathcal{G}_l^2}{\kappa_m\kappa_h - 4\mathcal{G}_l^2}, \tag{7.61}$$

which is denoted by the dashed horizontal lines in Figure 7-11(a).

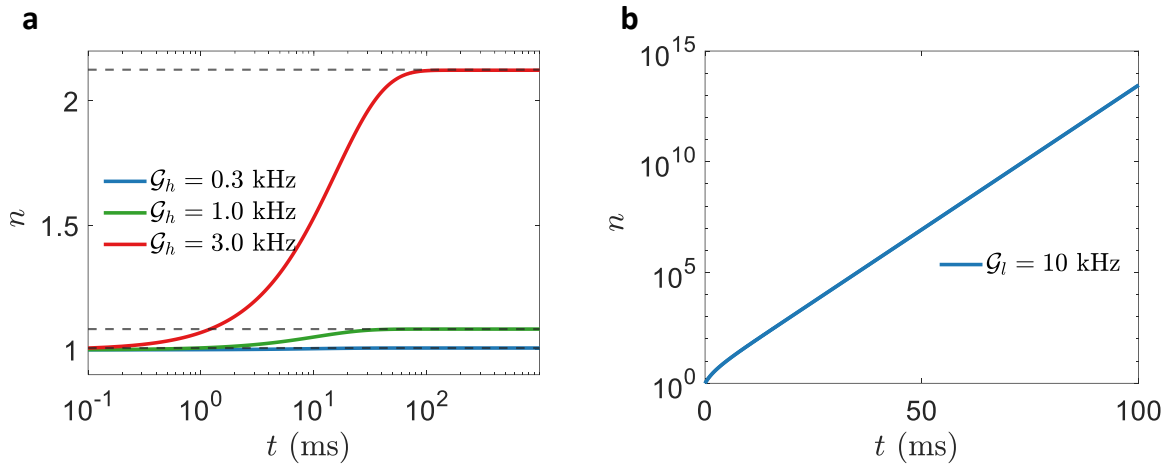

Figure 7-11: Numerical simulation of the laser heating of nuclear magnon using the ONQ effect. The figures shows the time evolution of the occupation of the nuclear magnon $n_m(t)$ in (a) weak-coupling regime (using master equation) and (b) strong-coupling regime (using semi-classical rate equation). $\kappa_m = 0.1$ kHz, $\kappa_h = 1$ MHz.

Strong-Coupling Regime

If $\frac{4\mathcal{G}_l^2}{\kappa_m \kappa_l} > 1$, then the occupation number of NMs would not reach a steady-state value. Instead, it will increase with time exponentially. Of course, the final population is limited by (1) the depletion of laser energy; and (2) the maximum number of NMs, which is NI.

Since in the strong-coupling regime, n_m could reach a very large value, the master equation is not suitable for studying the dynamics. This is because the Fock space needs to be truncated to a dimension greater than n_m, which significantly boosts the computational cost. In this regard, we use the semi-classical rate equation to study the laser heating dynamics, which is

$$\begin{aligned} \frac{dn_m}{dt} &= \mathcal{K}(n_m+1)(n_l+1) - \mathcal{K} n_m n_l + \kappa_m n_m (n_{\text{th}}+1) - (n_m+1) n_{\text{th}}, \\ \frac{dn_l}{dt} &= \mathcal{K}(n_m+1)(n_l+1) - \mathcal{K} n_m n_l + \kappa_h n_l, \end{aligned} \tag{7.62}$$

where $\mathcal{K} = \frac{4\mathcal{G}_l^2}{\kappa_m + \kappa_l}$. A numerical solution of the rate equation is shown in Figure 7-11(b), where the exponential growth of n_m with time can be observed.

7.5.7 Laser Cooling of a Single Nuclear Spin

In previous sections, we discussed the laser cooling/heating of NMs, which are the collective excitations of an NSE. Similar mechanisms can potentially be applied to cool down a single nuclear spin as well.

For a single nuclear spin, the concept of NM does not apply. Instead, one should deal with the occupation number of the excited state, which is also denoted as $n_{\rm th}$ here for clarity. The ONQ coupling strength with a single nuclear spin is

$$\mathcal{G}_h = \mathcal{g}^{\rm ONQ}\mathcal{E}_p\sqrt{\frac{\hbar\omega_h}{2\varepsilon_0 V_h}}, \tag{7.63}$$

which lacks the $\sqrt{N}$ amplification factor (i.e., $N = 1$). Fortunately, by judicious nano-photonics design, an ultra-small mode volume $V_h \sim 10^{-22}$ m^3 at $\omega_h = 1$ eV could be achievable [97]. Thus, one has $\mathcal{G}_h \approx 20$ Hz when $\mathcal{E}_p = 10$ MV/m.

Meanwhile, different from the NM, whose decay rate is constrained by the interactions between nuclear spins, a single nuclear spin can have a decay rate $\kappa_m \lesssim 1$ μHz when isolated from other nuclear/electron spins [8,9]. In this case, after laser cooling, the finally occupation number of the excited state is

$$\begin{aligned} n_m^{\rm steady} &= \frac{\kappa_m\kappa_h}{4\mathcal{G}_h^2 + \kappa_m\kappa_h} n_{\rm th} \\ &\approx 6\times 10^{-4} n_{\rm th}, \end{aligned} \tag{7.64}$$

where we used $\mathcal{E}_p = 10$ MV/m, $\kappa_m = 1$ μHz, and $\kappa_h = 1$ MHz. Note that since the coupling strength is $\mathcal{G}_h \approx 20$ Hz, the pumping laser should be stable for a duration on the order of seconds.

7.6 Applications: NER vs. ONQ

The potential applications of the ONQ effect are listed in Table 7.3, while those of the NER effect are listed in Table 6.1. One can see that ONQ and NER have some common applications, such as controlling single nuclear spins. On the other hand,

Table 7.2: Comparison of the potential applications of the NER and ONQ effects

Application	NER	ONQ
Single Nuclear Spin Manipulation	✓	✓
Spectroscopy	✓	✓
NSE Manipulation (Quantum Storage)	✓	✓
Quantum Transduction	✓	✗
Laser Cooling/Heating	✓	✗

ONQ has some unique applications, such as the laser cooling of NMs. The comparison of potential applications of the NER and ONQ effects is summarized in Table 7.2.

Table 7.3: Potential applications of the ONQ effect. The desired transition(s) for a certain application are in bold font.

Application	Specification	ω_p-photon (Optical)	ω_q-photon (Optical)	ω_r-photon (MW/RF)	Nuclear Spin	Frequency Matching Condition
Single Nuclear Spin Manipulation	Rabi Oscillation	Pump	Pump	Not Involved	$\|\mathbf{e}\rangle \leftrightarrow \|\mathbf{g}\rangle$	$\|\omega_p - \omega_q\| = \Delta_{ge}$
Spectroscopy	Isotopic Mapping, etc.	Pump	**Creation**	Not Involved	$\|e\rangle \leftrightarrow \|g\rangle$	$\|\omega_p - \omega_q\| = \Delta_{ge}(X)$
Quantum Storage	Storage	**Annihilation**	Pump	Not Involved	$\|\mathbf{G}\rangle \rightarrow \|\mathbf{E}\rangle$	$\|\omega_p - \omega_q\| = \Delta_{GE}$
	Readout	**Creation**	Pump	Not Involved	$\|\mathbf{E}\rangle \rightarrow \|\mathbf{G}\rangle$	
Quantum Transduction	Optical $\rightarrow$ MW/RF	Pump	**Annihilation**	**Creation**	Off-resonance	$\omega_p - \omega_q = \omega_r$ $\omega_p - \omega_q \neq \Delta_{GE}$
	MW/RF $\rightarrow$ Optical	Pump	**Creation**	**Annihilation**	Off-resonance	
Laser Cooling	Cool down Nuclear Magnons	Creation	Pump	Not Involved	$\|\mathbf{n+1}\rangle \rightarrow \|\mathbf{n}\rangle$	$\omega_p - \omega_q = \Omega_m$

Chapter 8

Miscellaneous Topics

8.1 Experimental Considerations

In this section, we briefly discuss some issues relevant to the the experimental demonstration of the ONQ effect.

8.1.1 Size of the Crystal Sample

As discussed in previous chapters, the collective ONQ coupling strength $\mathcal{G}_h$ between the optical fields and the NSE is an intensive property that depends on $\rho \equiv \frac{N}{V_h}$, where N is the number of nuclear spin, while V_h is the mode volume of the ω_h-cavity. Hence, ρ is approximately the number density of the nuclear spins. One can see that $\mathcal{G}_h$ is approximately independent of the size of the crystal that contains the nuclear spin, which should be comparable with V_h.

On the other hand, the collective ONQ interaction in Eq. (7.22) requires the optical fields to be uniform in the whole crystal sample, otherwise only part of the nuclear spins interact with optical fields. Hence, the size of the crystal should not be too large. Particularly, the optical fields can have stronger intensity when focused onto a smaller spot-size, and the spot-size is limited by the wavelength of the optical field, which is on the order of 1 μm. To this end, we suggest using a crystal sample with transverse area of $[1\ \mu\text{m}]^2$ to demonstrate the ONQ coupling between optical

photons and the NSE.

Another factor that should be considered is the penetration depth of the optical field. As discussed in the main text, we propose to use optical fields whose frequencies ω are below the bandgap E_g of the crystal. Therefore, the direct absorption of the laser energy via the one-photon process is in principle zero. On the other hand, the multi-photon process, whereby electrons do interband transitions by simultaneously absorbing multiple photons, can lead to the absorption of the laser energy. Specifically, the intensity of the two- and three-photon process is determined by the two- and three-photon absorption coefficient α_2 and α_3, which are on the order of 10^{-10} m/W and 10^{-25} m^3/W^2 in typical semiconductors [139–145]. The penetration depth of an optical field due to the two-photon absorption can be estimated as [139, 144]

$$\begin{aligned} d_{2\text{ph}} &= \frac{1}{\alpha_2 P_{\text{in}}}, \\ d_{3\text{ph}} &= \frac{1}{\alpha_3 P_{\text{in}}^2}, \end{aligned} \tag{8.1}$$

respectively, where $P_{\text{in}} = \frac{1}{2} c \varepsilon_0 \mathscr{E}^2$ is the incident laser power. Here c is the speed of light. If the electric field is $\mathscr{E} = 10$ MV/m, then one has $d_{2\text{ph}} \approx 7.5 \times 10^4$ μm and $d_{3\text{ph}} \approx 5.7 \times 10^8$ μm. This indicates that the two-photon absorption is much stronger than the three-photon absorption when $\mathscr{E} = 10$ MV/m, so we will only consider two-photon absorption when estimating the temperature rise below. On the other hand, if the depth of the crystal is $d = 0.1$ μm, then the optical field inside can be considered as uniform, since $d \ll d_{2\text{ph}}$.

In summary, we suggest using a crystal sample with a $1 \times 1 \times 0.1$ μm^3 dimension, which can ensure that the optical fields inside are uniform. Considering that the number density of nuclear spins can be on the order of 10^{28} m^{-3} in typical semiconductors (e.g., zbGaAs), the $1 \times 1 \times 0.1$ μm^3 crystal sample contains around 10^9 nuclear spins.

8.1.2 Temperature Rise In the Electron/Phonon System Under Laser Illumination

In this section, we estimate the temperature rise of the crystal sample under laser illumination. The duration τ_{laser} of the laser illumination needs to be on the order of ms (Figure 3 in the main text), which is much longer than the timescale $\tau_{e,p}$ of electron/phonon dynamics (typically fs to ps). Hence, we first treat the laser as a continuous wave laser to estimate the temperature rise in the electron/phonon system. The laser energy absorption power per unit area can be estimated with [146]

$$\begin{aligned} P_{\text{abs}} &= P_{\text{in}} \left(1 - e^{-\frac{d}{d_{2\text{ph}}}} \right) \\ &\approx P_{\text{in}} \frac{d}{d_{2\text{ph}}} \\ &= \frac{1}{2} c \varepsilon_0 \mathscr{E}^2 \frac{d}{d_{2\text{ph}}}, \end{aligned} \tag{8.2}$$

where P_{in} is the incident laser power.

The temperature rise in the electron/phonon system can be estimated from

$$\begin{aligned} \Delta T_{ep} &= \frac{P_{\text{abs}}}{K} d \\ &\approx 1.5 \text{ mK} \end{aligned} \tag{8.3}$$

where we use $\mathscr{E} = 10$ MV/m (laser power 130 mW/μm^2), $d = 0.1$ μm, and the thermal conductivity is taken as $K = 10 \text{ W} \cdot \text{m}^{-1} \cdot \text{K}^{-1}$. Here, we would like to remark that the defects in the crystal sample, which could result in one-photon absorption of laser energy, should be avoided. Hence, high-quality crystal samples are desirable.

Besides, if the laser frequency satisfies $2\omega < E_g$, then the two-photon absorption is forbidden as well. In this case, the leading order contribution to the absorption would be the three-photon process, which is much slower, as discussed before. The absorption of the laser energy and the temperature rise could be even smaller than those estimated in Eqs. (8.2, 8.3).

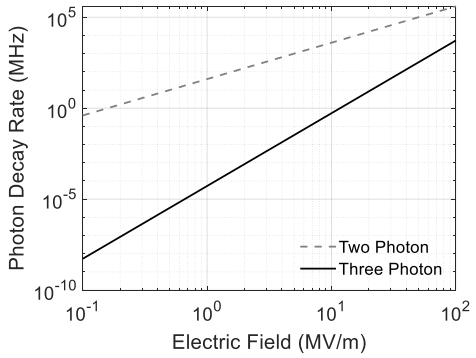

Figure 8-1: Photon decay rate due to two- and three-photon absorption as a function of electric field strength in zinc blende GaAs.

8.1.3 Cavity Photon Decay due to Multi-Photon Absorption

The multi-photon absorption leads to the decay of the cavity photons as well, which limits the maximum achievable quality factor of the cavity. The decay rate of the photon due to two/three-photon absorption can be estimated as

$$\kappa_{2\text{ph}\,(3\text{ph})} = \frac{c}{d_{2\text{ph}\,(3\text{ph})}}, \tag{8.4}$$

which is plotted in Figure 8-1 as a function of the electric field strength $\mathscr{E}$. As discussed in the main text, the electric field needs be on the order of 10 MV/m for the laser cooling of nuclear magnons. At such an electric field strength, the photon decay rate due to two-photon absorption is on the order of GHz. Hence, the two-photon absorption needs to be avoided by using a laser with frequency ω that satisfies $2\omega < E_g$, where E_g is the bandgap. In this case, the leading order contribution would be the three-photon process. From Figure 8-1, one can see that the photon decay rate from three-photon absorption is below MHz when $\mathscr{E} = 10$ MV/m. If the photon decay rate needs to be further decreased, then it would be necessary to avoid three-photon absorption as well, whereby the four-photon absorption would be the leading contribution in the multi-photon process.

8.1.4 Influence of the Photon/Laser Linewidth

The laser/photon linewidth is an important parameter for the ONQ effect. Before further discussions, we would like to note that while it is desirable to have a small laser/photon linewidth, it is *not necessary* to have a laser/photon linewidth smaller than the NMR frequency. Nonlinear optical responses can exist even if the laser/photon linewidth is wide. For example, the bulk photovoltaic effect [147], whereby a DC charge current is generated under light illumination, can happen under white light [148], which has a ultra-large "linewidth".

As can be observed in Eqs. (7.6, 7.27), the ONQ transition rate is inversely proportional to the photon linewidth. Here we further examine the importance of the laser/photon linewidth. We assume the laser/photon has a Lorentzian lineshape, and the two-color laser/photon used in the ONQ effect are described by

$$\begin{aligned} \mathscr{E}_1(\omega_1) &= \frac{1}{\pi}\frac{\kappa_p}{(\omega_1-\omega_p)^2+\kappa_p^2}, \\ \mathscr{E}_2(\omega_2) &= \frac{1}{\pi}\frac{\kappa_q}{(\omega_2-\omega_q)^2+\kappa_q^2}. \end{aligned} \tag{8.5}$$

One can see that the central frequency is ω_p (ω_q) and the linewidth is κ_p (κ_q).

When two-color fields with frequencies ω_1 and ω_2 are combined to trigger the Rabi oscillation of the nuclear spins, the efficiency of the Rabi oscillation is proportional to $\eta(\omega_1,\omega_2)=\frac{f_{\text{Rabi}}^2}{f_{\text{Rabi}}^2+(\omega_1-\omega_2-\Delta)^2}$, where Δ is the nuclear spin resonance frequency and f_{Rabi} is Rabi frequency. Under laser/photon with lineshapes described by Eq. (8.5), the overall efficiency of the Rabi oscillation can be estimated with

$$\begin{aligned} \eta_0 &= \int\int \mathrm{d}\omega_1\mathrm{d}\omega_2 \mathscr{E}_1(\omega_1)\mathscr{E}_2(\omega_2)\eta(\omega_1,\omega_2) \\ &= \frac{1}{\pi^2}\int\int \mathrm{d}\omega_1\mathrm{d}\omega_2 \frac{\kappa_p}{(\omega_1-\omega_p)^2+\kappa_p^2}\frac{\kappa_q}{(\omega_2-\omega_q)^2+\kappa_q^2}\frac{f_{\text{Rabi}}^2}{f_{\text{Rabi}}^2+(\omega_1-\omega_2-\Delta)^2} \\ &= \frac{f_{\text{Rabi}}(f_{\text{Rabi}}+\kappa_p+\kappa_q)}{(\omega_p-\omega_q-\Delta)^2+(f_{\text{Rabi}}+\kappa_p+\kappa_q)^2}. \end{aligned} \tag{8.6}$$

One can see that when $\omega_p-\omega_q-\Delta=0$ and $\kappa_p=\kappa_q=0$, then the efficiency is $\eta_0=1$,

as expected. Besides, one has $\eta_0 \sim 1$ when

$$\begin{aligned} \omega_p - \omega_q - \Delta &\lesssim f_{\text{Rabi}}, \\ \kappa_{p\,(q)} &\lesssim f_{\text{Rabi}}. \end{aligned} \tag{8.7}$$

That is, the detuning from perfect resonance frequency and the linewidth of the two-color laser/photon should be kept below the Rabi frequency f_{Rabi}, which can be on the order of kHz to MHz.

8.2 Nuclear Magnetism

In electronic systems, the interaction between nearby electron spins could lead to the formation of macroscopic electronic spin (magnetic) structures, including ferromagnetism, anti-ferromagnetism, ferri-magnetism, and spin waves [149]. In this section, we discuss the possibility of the formation of nuclear spin patterns.

First, one should note that a spin polarization always breaks time-reversal symmetry (TRS), and a single nuclear spin could not spontaneously have a net spin polarization. To establish a magnetic structure, the TRS must be broken. In practice, the TRS can be broken by

- external fields, such as magnetic field or circularly polarized light;
- interactions between nuclear spins, which could lead to spontaneous symmetry breaking.

Next, we discusses these possibilities in more detail.

8.2.1 Magnetic Fields

External magnetic fields naturally break TRS, and hence lead to a nuclear spin polarization. In the following, we will show that various nuclear spin patterns can be realized under magnetic fields.

"Ferromagnetic-like" Structure

If all the nuclei are of the same species and are in the same environment, then they would have the same polarization under external magnetic fields, which can be regarded as a "ferromagnetic-like" structure [1].

"Anti-ferromagnetic-like" Structure

If the nuclei are of different species, then "anti-ferromagnetic-like" structures could arise under magnetic fields as well. For example, the gyromagnetic ratio of ^{13}C and ^{29}Si are

$$\begin{aligned} \gamma^{^{13}\mathrm{C}} &\approx +10.7084 \times \frac{2\pi \cdot \mathrm{MHz}}{\mathrm{T}}, \\ \gamma^{^{29}\mathrm{Si}} &\approx -8.465 \times \frac{2\pi \cdot \mathrm{MHz}}{\mathrm{T}}, \end{aligned} \tag{8.8}$$

respectively. Consequently, in a SiC compound, if a magnetic field along $+z$ direction is applied, then ^{13}C would preferably polarize along $+z$ direction, whereas ^{29}Si would preferably polarize along $-z$ direction, forming a "anti-ferromagnetic-like" structure.

"Staggered-magnetic-like" Structure

When the quadrupole interaction (Section 2.3) is considered, the nuclear spin could form more complicated magnetic structures, which is here called "staggered-magnetic-like" structure.

First, we would like to remark that although the quadrupole interaction leads to anisotropy and a "preferred"-direction $\boldsymbol{n}$ [2], it cannot lead to *net* nuclear spin polarization. This is because the nuclear quadrupole interaction $H_{\mathrm{Q}} = I \cdot Q \cdot I$ is quadratic in spin operator I, so the nuclear spin would have the same energy, and thus equal probability, to polarize along $+\boldsymbol{n}$ and $-\boldsymbol{n}$ directions. Consequently, the net spin polarization is still zero in equilibrium.

[1] Note that this is not true ferromagnetism, because ferromagnetism should arise spontaneously without external magnetic fields. Here we use "ferromagnetic-like" only to indicate that all the nuclear spins have the same polarization. Similar caveat applies to the "anti-ferromagnetic-like" and "staggered-magnetic-like" patterns below.

[2] $\boldsymbol{n}$ is one of principal axis of the quadrupole tensor Q, along which the nuclear quadrupole interaction energy is the lowest.

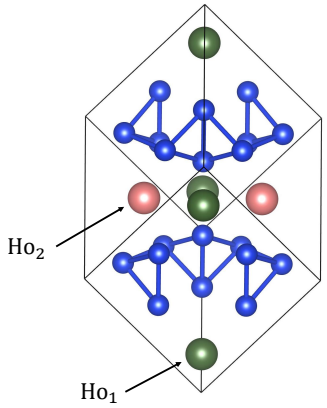

Figure 8-2: Atomic structure of $HoSi_3$. The blue atoms are Si, while pink and green atoms are two equivalent Ho.

If quadrupole interaction and external magnetic field co-exist, then the net polarization of the nuclear spin is determined by both the $\boldsymbol{n}$ vector and the magnetic field. As a result, nuclear spins under different environment (different $\boldsymbol{n}$) could have different net spin polarization. Here we use $HoSi_3$ as an example. $HoSi_3$ has space group I4/mmm, and the two Ho atoms in the unit-cell are in inequivalent environments (Figure 8-2), leading to different $\boldsymbol{n}$. If a 1 T magnetic field is applied along the z direction ([111] crystallographical direction), then the two inequivalent Ho atoms have different net spin polarization on the ground state, which are

$$\begin{aligned} \langle I \rangle_{\mathrm{Ho}_1} &= [2.5270,\ 2.3921,\ -0.3765], \\ \langle I \rangle_{\mathrm{Ho}_2} &= [2.4952,\ 2.2955,\ -0.8626]. \end{aligned} \tag{8.9}$$

Note that $\langle I \rangle_{\mathrm{Ho}_1}$ and $\langle I \rangle_{\mathrm{Ho}_2}$ are neither parallel nor anti-parallel to each other, which can be considered as the "staggered-magnetic-like" structure.

Temperature Considerations

In the discussions above, we show that under external magnetic fields, the nuclear spin ground state would have a net spin polarization. Hence, a nuclear spin structure can be realized. To achieve such a net spin polarization, the nuclear spin should have a large probability to be on the ground state. Since the nuclear spin splitting under

a 1 T magnetic field is usually on the order of 10 MHz, the temperature should be below 0.1 mK to ensure a high occupancy of the ground state.

8.2.2 Circularly Polarized Light

Besides magnetic field, circularly polarized light (CPL) [3] naturally breaks TRS as well: the time-reversal partner of a left-handed CPL is a right-handed CPL. As we will show below, CPL can dynamically lead to a net spin polarization. Here we assume there is no external magnetic fields, while a quadrupole interaction leads to the nuclear spin splitting. For brevity, we assume $I = 1$, and

$$Q = \begin{bmatrix} -100 & 0 & 0 \\ 0 & -100 & 0 \\ 0 & 0 & 200 \end{bmatrix} \times 2\pi \cdot \text{MHz}. \tag{8.10}$$

The eigenstates under the quadrupole interaction are $\{|0\rangle, |+1\rangle, |-1\rangle\}$, among which $|0\rangle$ is the ground state with an energy level of -200 MHz, while $|\pm 1\rangle$ are degenerate with an energy of $+100$ MHz.

Since $|\pm 1\rangle$ are degenerate, they are simultaneously populated when one applies a linear polarized light (LPL) resonant with the $|0\rangle \rightarrow |\pm 1\rangle$ transition. This effect is shown in Figure 8-3(a). On the other hand, when a CPL is applied, the transition between $|0\rangle$ and $|+1\rangle$ (or between $|0\rangle$ and $|-1\rangle$) is selectively triggered, depending on the helicity of the CPL. As shown in Figure 8-3(b), the nuclear spin selectively transits between $|0\rangle$ and $|-1\rangle$ when a right-handed CPL is applied, whereas $|+1\rangle$ is never occupied. Similarly, when a left-handed CPL is applied, $|-1\rangle$ would never be occupied.

The discussions above indicate that CPL can induce a dynamical nuclear spin polarization. Meanwhile, the ground state of the nuclear spin is still $|0\rangle$, and the nuclear spin always has the tendency to relax (thermalize) to $|0\rangle$. Therefore, the dynamical polarization competes with the relaxation process. A key parameter here

[3] For brevity, we will use CPL to denote circularly polarized radio frequency or microwave as well.

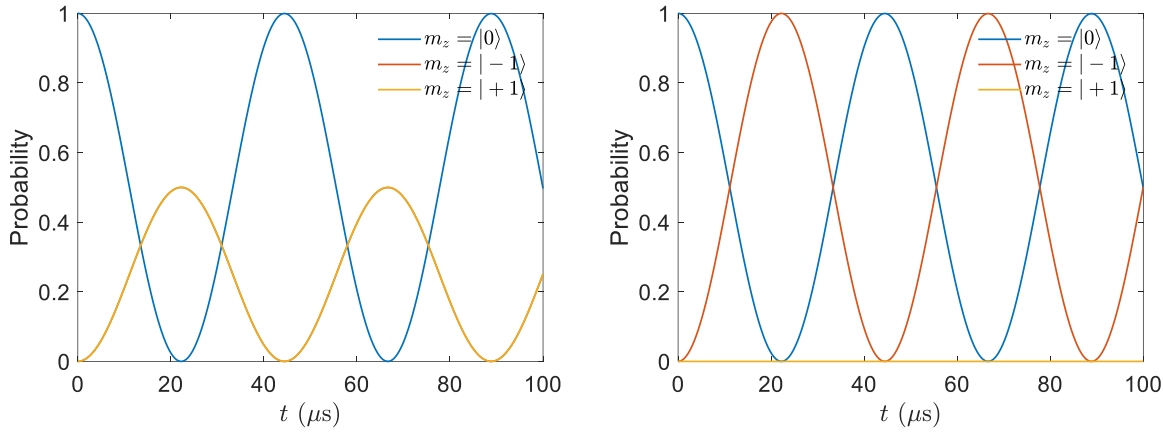

Figure 8-3: Rabi oscillations of a $I = 1$ nuclear spin under (a) LPL and (b) CPL. Under LPL, not net spin polarization is generated, because the nuclear spin has equal probability to be on the $|+1\rangle$ and $|-1\rangle$ states. In contrast, under CPL, a net spin polarization can be generated because only the transitions between $|0\rangle$ and $|-1\rangle$ is allows.

is $\frac{f}{\kappa}$, where f is the Rabi frequency between $|0\rangle$ and $|+1\rangle$ or $|-1\rangle$, while κ is the relaxation rate of the nuclear spin. When $\frac{f}{\kappa} > 1$, the nuclear spin can have a full polarization to $|+1\rangle$ or $|-1\rangle$. On the other hand, when $\frac{f}{\kappa} < 1$, only partial polarization is achievable.

8.2.3 Spontaneous Symmetry Breaking Due to Interactions

In electronic systems, the interaction between nearby electron spins could result in magnetism [149], which breaks the TRS. This can be considered as a spontaneous symmetry breaking. Similarly, the interactions between nuclear spins could result in nuclear magnetism as well. In contrast to electronic magnetism, the nuclear magnetism has some notable difference

- The exchange interaction between localized electron spins, which leads to electronic magnetism, are usually short range interactions. This because usually these interactions depend on the overlap between electron wavefunctions, which quickly decays with distance. Consequently, in many models that describes magnetism, such as the Ising model and the Heisenberg model, only nearest-

neighbor interactions are considered [4].

In contrast, the interactions between nuclear spins mostly result from dipolar interactions, which is long range and decays with $\frac{1}{r^3}$, with r the distance between the nuclear spins. This could significantly complicated the nuclear spin dynamics. The nuclear spins do not necessarily form ferromagnetic or anti-ferromagnetic structures at low temperature. For example, if the interaction between two nuclear spins are $H_{\alpha\beta} = \frac{J_0 I^\alpha I^\beta}{r^3_{\alpha\beta}}$ with $J_0 > 0$, then the potential energy between nearest-neighbor nuclear spins could be minimized when an anti-ferromagnetic structure is formed. However, the anti-ferromagnetic structure has a maximized potential energy between next-nearest-neighbor nuclear spins. Hence, the the anti-ferromagnetic structure is not necessarily the ground state. Instead, complex spin structures resembling the electron spin glasses could appear [150–152].

- The exchange interaction between electron spins can reach meV, equivalent to a temperature of tens of Kelvin. On the other hand, the dipole interaction between nuclear spins are only on the order of kHz [cf. Section 2.4], equivalent to tens of nK. As the critical temperature of the magnetic phase transitions are usually comparable with the interaction strength [153–155], one needs to cool down to below nK to observe the spontaneous nuclear spin magnetic structure, which is rather challenging.

8.3 Nuclear Spin Interactions with Phonons

Besides electric/magnetic/optical fields, nuclear spins could possible interact with phonons/acoustic waves (we will simply use "phonon" hereafter) as well. On one hand, this could enable the phonon control over nuclear spins [44, 45], similar to the phonon control over a variety of other quantum systems [156–159]. On the other

[4]The are also dipolar interactions between electron spins, which is long range. However, the dipolar interaction is on the order of μeV between nearest electron spins. This is significantly weaker than the exchange interaction, which can reach meV. Consequently, the properties of the electron spins are predominantly determined by the exchange interaction.

hand, the coupling with phonons could also lead to the decoherence/relaxation of nuclear spins. In this section, we examine the interaction between nuclear spins and phonons.

First, we note that the frequency of optical phonons is most systems is on the order of THz, well above the nuclear spin frequency, which is usually below GHz. Therefore, optical phonons cannot resonantly couple with phonons[5], and we only need to consider acoustic phonons near the Γ-point in the Brillouin zone, which can be mimicked by compressive/tensile strain. The strain leads to a change in the EFG, and hence the quadrupole interaction, which can be expressed as

$$\begin{aligned} H^{\text{phonon}} &= \sum_{ij,\,pq} \mathcal{S}_{ij}^{pq} u_{pq} I_i I_j \\ &\sim g^{\text{phonon}} |e\rangle\langle g| + h.c. \end{aligned} \tag{8.11}$$

where on the second line we transformed the Hamiltonian to the subspace spanned by two nuclear spin states $|e\rangle$ and $|g\rangle$. u_{pq} denotes the strain with p, q as Cartesian indices. $\mathcal{S}_{ij}^{pq} \equiv \frac{\partial Q_{ij}}{\partial u_{pq}}$ is the response function.

In Figure 8-4, we show the change in EFG $\Delta\mathcal{V}$ at the site of Ga nuclei in wGaN as a function of u_{xx}. By fitting the data with first-order polynomial, we obtain

$$\mathcal{S} \sim 3.0 \text{ MHz}. \tag{8.12}$$

We first consider a single nuclear spin. The magnitude of the strain u^0 when a single phonon (per unit cell) is excited can be estimated with

$$u^0 = \sqrt{\frac{\hbar\omega_{\text{ph}}}{GV_{\text{u.c.}}}}, \tag{8.13}$$

where ω_{ph} is the phonon frequency, G is the elastic modulus, while $V_{\text{u.c.}}$ is the volume of the unit cell. Using $\omega_{\text{ph}} = 20$ MHz, $V_{\text{u.c.}} = 10^{-28}$ m^3, and $G = 300$ GPa, one has $u^0 \sim 4 \times 10^{-5}$. Therefore, the coupling strength between a single nuclear spin with a

[5] at least in the sense of first-order coupling

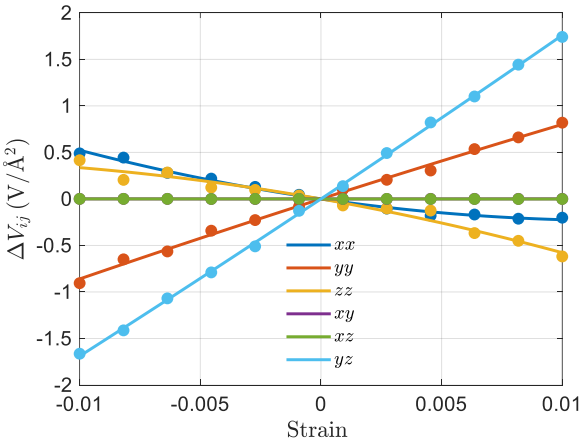

Figure 8-4: Change in the EFG tensor at the site of Ga nuclei in wGaN as a function of strain u_{xx}.

single phonon (per unit cell) is

$$\mathcal{g}^{\text{phonon}} = \langle e|\mathcal{S}_{ij}u^0 I_i I_j|g\rangle \sim 10 \text{ kHz}. \tag{8.14}$$

The exact magnitude of $\mathcal{g}^{\text{phonon}}$ depends on the quadrupole moment of the nuclei as well.

Next, we consider the coupling between a single phonon with a NSE, whereby the Hamiltonian can be written as

$$\begin{aligned} \mathcal{H}^{\text{phonon}} &= \sum_\alpha u^\alpha I^\alpha \cdot \mathcal{S} \cdot I^\alpha \\ &= \frac{\mathcal{g}^{\text{phonon}}}{\sqrt{N}} \sum_\alpha |e\rangle\langle g|_\alpha + h.c. \end{aligned} \tag{8.15}$$

where we omitted p, q. On the second line we assumed that the system is homogeneous, N is the total number of unit cells [6]. The strain in each unit cell when a single photon is excited is thus $\frac{u^0}{\sqrt{N}}$, because the elastic energy of the phonon has to be shared by all the unit cells. Then the coupling strength between phonon and the

[6] also the total number of nuclear spins

NSE is (cf. Sections 7.3.2, 7.3.3)

$$\begin{aligned} \mathscr{G}^{\text{phonon}} &= \langle \mathbb{1} | \mathscr{H}^{\text{phonon}} | \mathbb{0} \rangle \\ &= \mathscr{g}^{\text{phonon}}, \end{aligned} \tag{8.16}$$

which is independent of the number of unit cells.

One can see that the coupling between phonon and nuclear spin (ensemble) is a relatively strong interaction, and the phonon control over nuclear spins could be efficient. On the other hand, the decoherence/relaxation of nuclear spins due to the coupling with phonons can also be strong. Fortunately, such a decoherence/relaxation can be avoided by designing the structure of the sample, so that there are no phonons whose frequencies are resonant with nuclear spins. A simple strategy is to use a crystal with small size L. With a finite L, the phonon modes in the crystal is discrete, i.e.,

$$\omega_{\text{ph}}^{n} \sim v_{\text{ph}} \frac{2\pi}{L} n, \tag{8.17}$$

where v_{ph} is the speed of the acoustic phonon, and n denotes the n-th phonon mode. The frequency spacing between different phonon modes is thus

$$\begin{aligned} \Delta\omega_{\text{ph}} &= v_{\text{ph}} \frac{2\pi}{L} \\ &\sim \frac{3 \text{ GHz}}{L \text{ } [\mu\text{m}]}. \end{aligned} \tag{8.18}$$

On the second line L is in the unit of μm, and we have used $v_{\text{ph}} = 3000$ m/s. One can see that when $L = 1$ μm, the frequency spacing between different phonon mode is on the order of 3 GHz, which is significantly larger than the nuclear spin frequency. Therefore, it is feasible to avoid phonons resonant with nuclear spin transitions and the resultant decoherence/relaxation, which could help improve the precision of the spectroscopy.

Chapter 9

Concluding Remarks and Future Directions

In conclusion, in this thesis we propose an opto-nuclear quadrupolar (ONQ) effect, whereby two-color photons can be coupled with nuclear spins. Some advantage of the ONQ effect are

- Ancillary electron spins are not required, in contrast to the approaches discussed in Chapter 3;
- There is flexibility in choosing the wavelength of the optical photons, as discussed in Section 4.3;
- The ONQ effect is stronger by several orders of magnitude than other nonlinear optical effects that could couple with nuclear spins, as discussed in Section 5.2.

Then, we propose some potential applications of the ONQ effect under feasible experimental conditions (Chapter 7), including quantum memory, quantum transduction, and laser cooling of nuclear magnons for initialization. These applications fully exploit the long relaxation/decoherence time nuclear spins.

For future studies, there are several possible directions

- Find/design materials suitable for ONQ applications. One can focus on topological materials and/or materials containing isotopes with large quadrupole

moment, which could have strong ONQ response. For certain applications, one also needs to consider e.g., the isotope purity.

- Design photonics structure to enhance the light-matter interaction strength. For example, if one aims at controlling single nuclear spins, then optical cavities with small mode volume is favorable. Optical cavities with high Q-factors are also desirable.

- On the experimental side, the experimental demonstration of the ONQ effect is desirable. Some proof-of-principle experimental can be

  - Detecting the side peaks due to the ONQ scattering or detecting the nuclear spin dynamics induced by the ONQ effect, as proposed in proposed in Section 7.2. These two "classical" experiments could be relatively easier to demonstrate.

  - The ONQ control over single nuclear spins or nuclear spin ensemble, as discussed in Section 7.1 and 7.3. These two experiments are relevant to the quantum properties of the nuclear spins, and could be more challenging.

Appendix A

Nonlinear Optical Responses of Electronic System

During my Ph.D. study, besides the *Optical Control over Nuclear Spins*, which is the focus of the main text of this theis, I have been working other some other projects, which I will briefly describe in the following.

Enhanced Linear/Nonlinear Optical Responses in Topological Materials

- Linear optical responses (gain/absorption coefficient) is enhanced in topological materials with Mexican-hat band structure due to (1) band inversion that increases the interband transitions rate and (2) Mexican-hat band structure that increases the joint density of states. By exploring the topological materials database, we found a number of materials that could out-perform the MgCdTe detector in the infrared/terahertz range. Recently, the large optical response of $Pb_xSn_{1-x}Se$, which is a Mexican-hat topological insulation, has been verified in experiments.

  Related publication:

  Haowei Xu, Jian Zhou, Hua Wang, and Ju Li, Giant Photonic Response of Mexican-Hat Topological Semiconductors for Mid-infrared to Terahertz Applications. J. Phys. Chem. Lett. 11, 6119–6126 (2020).

Mark Polking, Haowei Xu, Ju Li, et. al. Manuscript in preparation.

- We point out several guidelines for designing materials with strong nonlinear optical responses, including (1) topological band structure, (2) strong inversion symmetry breaking, and (3) small electronic band gap. We substantiate these guidelines with Janus transition metal dichalcogenides (TMDs) in the 1T' phase, whose nonlinear photocurrent conductivity is larger than other 2D materials by two orders of magnitude. Recently, the colossal terahertz frequency nonlinearities of 1T' Janus TMDs have been observed in experiments.

  Related publication:

  Haowei Xu, Hua Wang, Jian Zhou, Yunfan Guo, Jing Kong and Ju Li, Colossal switchable photocurrents in topological Janus transition metal dichalcogenides. npj Comput. Mater. 7, 1–9 (2021).

  Jiaojian Shi*, Haowei Xu* (equal contribution), Christian Heide, Changan HuangFu, Chenyi Xia, Felipe de Quesada, Hao Zhou, Tianyi Zhang, Leo Yu, Amalya Johnson, Fang Liu, Tony Heinz, Liying Jiao, Shambhu Ghimire, Ju Li, Jing Kong, Yunfan Guo, and Aaron M. Lindenberg. Giant terahertz-frequency nonlinearities from a monolayer Janus topological semiconductor. Manuscript in preparation.

Electron Spin-Related Nonlinear Optical Responses

- We propose a bulk spin photovoltaic (BSPV) effect, whereby spin current can be generated under light illumination. By symmetry analysis, we elucidate that the only requirement of the BSPV effect is inversion symmetry breaking, while time-reversal symmetry breaking is not necessary. Furthermore, if the system has mirror symmetry, then via the BSPV effect, it is possible to obtain pure spin current without accompanying charge current, which is highly desirable for certain spintronics applications.

  Related publication:

Haowei Xu, Hua Wang, Jian Zhou, and Ju Li, Pure Spin Photocurrent in Non-centrosymmetric Crystals: Bulk Spin Photovoltaic Effect. Nature Commun. 12, 4330 (2021)

- We propose a nonlinear Edelstein effect (NLEE), whereby static spin polarization can be generated under light illumination. We demonstrate that ferromagnetic, ferrimagnetic, and anti-ferromagnetic orders can all be realized with the NLEE. We also discussed the relationship between NLEE and other magneto-optical effects such as inverse Faraday effect. This theoretical proposition agrees well with recent experimental results [160].

  Related publication:

  Haowei Xu, Jian Zhou, Hua Wang, and Ju Li, Light-Induced Static Magnetization: Nonlinear Edelstein Effect. Phys. Rev. B 103, 205417 (2021).

Many-Body Effects in Nonlinear Optical Responses

- We formulate an Green's function formalism to incorporate many-body effects in nonlinear optical responses. Using this formalism, we found that in topological materials, nonlinear optical responses can be significantly different on the surface than in the bulk. For example, the nonlinear photocurrent on the surface can have opposite directions to that in the bulk. We attribute this effect to the topological surface properties.

  Related publication:

  Haowei Xu, Hua Wang, and Ju Li, Abnormal Nonlinear Optical Responses on the Surface of Topological Materials. npj Computational Materials 8, 111 (2022)

- Using the many-body formalism described above, we examined how electron-phonon coupling can affect nonlinear optical effects. We found that when the phonons are out-of-equilibrium (e.g., when there is a temperature gradient),

then they can significantly alter the optical selection rules and lead to non-trivial effects in nonlinear optical responses.

Related publication:

Haowei Xu, Hua Wang, and Ju Li, Nonlinear Photocurrents with Nonreciprocal Phonon Dressing. Phys. Rev. B 106, 035102 (2022).

Light-Induced Phase Transitions

- Inspired by optical tweezers, we illustrate that a linearly polarized laser pulse with selected frequencies can drive ultrafast diffusionless martensitic phase transitions in various materials. Coupling with electrons and/or phonons, light can effectively modify the energy landscape. We have illustrated this concept in various systems such as ferroelastic monolayer SnSe/SnO, bilayer hBN, and monolayer MoS_2. The phase transition switching time can be on the order of picoseconds, to be compared with the nanosecond time-scale in conventional thermal and diffusional phase transitions. The estimated energy consumption of the light-driven martensitic phase transitions is also about 2 orders of magnitude lower than that in Ge-Sb-Te alloy. Recently, some evidence of opto-mechanical-driven phase transition in SnSe has been observed in experiments.

  Related publications:

  Jian Zhou, Haowei Xu, Yifei Li, R. Jaramillo and Ju Li, Opto-Mechanics Driven Fast Martensitic Transition in Two-Dimensional Materials. Nano Lett. 18, 7794–7800 (2018).

  Haowei Xu, Jian Zhou, Yifei Li, R. Jaramillo, and Ju Li, Optomechanical control of stacking patterns of h-BN bilayer. Nano Res. 12, 2634–2639 (2019).

  Jian Zhou, Haowei Xu, Yongliang Shi, and Ju Li, Terahertz Driven Reversible Topological Phase Transition of Monolayer Transition Metal Dichalcogenides. Adv. Sci. 2003832 (2021).

  Jiaojian Shi*, Yijing Huang*, Christian Heide* (equal contribution), Carl-

Friedrich Schön, Haowei Xu, Yuki Kobayashi, Andrew F. May, Pooja Donthi Reddy, Duan Luo, Eamonn Hughes, Kunal Mukherjee, Mariano Trigo, Ju Li, Jian Zhou, Shambhu Ghimire, Matthias Wuttig, David A. Reis, Aaron M. Lindenberg. Evidence of opto-mechanical-driven topological phase transition in SnSe. Manuscript in preparation.

- We propose that using gapless surface states, the topological phase transition can happen at arbitrarily weak (but finite) external field strength. This can be regarded as an unconventional topological phase transition, where the bandgap closing is guaranteed by bulk-edge correspondence and symmetries, while the bandgap reopening is induced by external fields. This can be a convenient approach to realize topological phase transitions. As an example, using Floquet theory, we demonstrate that the surface of Bi_2Se_3 would become a quantum anomalous Hall insulator under circularly polarized light. In other words, Bi_2Se_3 becomes an axion insulator.

  Related publication:

  Haowei Xu, Jian Zhou, and Ju Li. Light-induced quantum anomalous Hall effect on the surfaces of topological insulators. Adv. Sci. 2101508 (2021)

Bibliography

[1] Paul Horowitz, Winfield Hill, and Ian Robinson. *The art of electronics*, volume 2. Cambridge university press Cambridge, 1989.

[2] Gary Wolfowicz, F Joseph Heremans, Christopher P Anderson, Shun Kanai, Hosung Seo, Adam Gali, Giulia Galli, and David D Awschalom. Quantum guidelines for solid-state spin defects. *Nature Reviews Materials*, 6(10):906–925, 2021.

[3] Igor Žutić, Jaroslav Fabian, and S Das Sarma. Spintronics: Fundamentals and applications. *Reviews of modern physics*, 76(2):323, 2004.

[4] SD Bader and SSP Parkin. Spintronics. *Annu. Rev. Condens. Matter Phys.*, 1(1):71–88, 2010.

[5] Jun John Sakurai and Eugene D Commins. Modern quantum mechanics, revised edition, 1995.

[6] Vitaly N Golovach, Massoud Borhani, and Daniel Loss. Electric-dipole-induced spin resonance in quantum dots. *Physical Review B*, 74(16):165319, 2006.

[7] Katja C Nowack, FHL Koppens, Yu V Nazarov, and LMK Vandersypen. Coherent control of a single electron spin with electric fields. *Science*, 318(5855):1430–1433, 2007.

[8] M Steger, K Saeedi, MLW Thewalt, JJL Morton, H Riemann, NV Abrosimov, P Becker, and H-J Pohl. Quantum information storage for over 180 s using donor spins in a 28si "semiconductor vacuum". *Science*, 336(6086):1280–1283, 2012.

[9] Kamyar Saeedi, Stephanie Simmons, Jeff Z Salvail, Phillip Dluhy, Helge Riemann, Nikolai V Abrosimov, Peter Becker, Hans-Joachim Pohl, John JL Morton, and Mike LW Thewalt. Room-temperature quantum bit storage exceeding 39 minutes using ionized donors in silicon-28. *Science*, 342(6160):830–833, 2013.

[10] Theodore H Maiman. Stimulated optical radiation in ruby. *Nature*, 187:493, 1960.

[11] Andrew Weiner. *Ultrafast optics*, volume 72. John Wiley & Sons, 2011.

[12] Frank L Pedrotti, Leno M Pedrotti, and Leno S Pedrotti. *Introduction to optics*. Cambridge University Press, 2017.

[13] PA Franken, Alan E Hill, CW el Peters, and Gabriel Weinreich. Generation of optical harmonics. *Physical Review Letters*, 7(4):118, 1961.

[14] Bahaa EA Saleh and Malvin Carl Teich. *Fundamentals of photonics*. john Wiley & sons, 2019.

[15] Bahram Jalali and Sasan Fathpour. Silicon photonics. *Journal of lightwave technology*, 24(12):4600–4615, 2006.

[16] Emanuel Knill, Raymond Laflamme, and Gerald J Milburn. A scheme for efficient quantum computation with linear optics. *nature*, 409(6816):46–52, 2001.

[17] Pieter Kok, William J Munro, Kae Nemoto, Timothy C Ralph, Jonathan P Dowling, and Gerard J Milburn. Linear optical quantum computing with photonic qubits. *Reviews of modern physics*, 79(1):135, 2007.

[18] Anasua Chatterjee, Paul Stevenson, Silvano De Franceschi, Andrea Morello, Nathalie P de Leon, and Ferdinand Kuemmeth. Semiconductor qubits in practice. *Nature Reviews Physics*, 3(3):157–177, 2021.

[19] Colin D Bruzewicz, John Chiaverini, Robert McConnell, and Jeremy M Sage. Trapped-ion quantum computing: Progress and challenges. *Applied Physics Reviews*, 6(2):021314, 2019.

[20] Mark Saffman. Quantum computing with atomic qubits and rydberg interactions: progress and challenges. *Journal of Physics B: Atomic, Molecular and Optical Physics*, 49(20):202001, 2016.

[21] Sepehr Ebadi, Alexander Keesling, Madelyn Cain, Tout T Wang, Harry Levine, Dolev Bluvstein, Giulia Semeghini, Ahmed Omran, J-G Liu, Rhine Samajdar, et al. Quantum optimization of maximum independent set using rydberg atom arrays. *Science*, page eabo6587, 2022.

[22] Su-Yang Xu, Qiong Ma, Huitao Shen, Valla Fatemi, Sanfeng Wu, Tay-Rong Chang, Guoqing Chang, Andrés M Mier Valdivia, Ching-Kit Chan, Quinn D Gibson, et al. Electrically switchable berry curvature dipole in the monolayer topological insulator wte2. *Nature Physics*, 14(9):900–906, 2018.

[23] Qiong Ma, Su-Yang Xu, Ching-Kit Chan, Cheng-Long Zhang, Guoqing Chang, Yuxuan Lin, Weiwei Xie, Tomás Palacios, Hsin Lin, Shuang Jia, et al. Direct optical detection of weyl fermion chirality in a topological semimetal. *Nature Physics*, 13(9):842–847, 2017.

[24] Junyeong Ahn, Guang-Yu Guo, and Naoto Nagaosa. Low-frequency divergence and quantum geometry of the bulk photovoltaic effect in topological semimetals. *Physical Review X*, 10(4):041041, 2020.

[25] Hikaru Watanabe and Youichi Yanase. Chiral photocurrent in parity-violating magnet and enhanced response in topological antiferromagnet. *Physical Review X*, 11(1):011001, 2021.

[26] Haowei Xu, Hua Wang, Jian Zhou, Yunfan Guo, Jing Kong, and Ju Li. Colossal switchable photocurrents in topological janus transition metal dichalcogenides. *npj Computational Materials*, 7(1):1–9, 2021.

[27] Liang Z Tan and Andrew M Rappe. Enhancement of the bulk photovoltaic effect in topological insulators. *Physical review letters*, 116(23):237402, 2016.

[28] Haowei Xu, Jian Zhou, Hua Wang, and Ju Li. Giant photonic response of mexican-hat topological semiconductors for mid-infrared to terahertz applications. *The Journal of Physical Chemistry Letters*, 11(15):6119–6126, 2020.

[29] Serwan Asaad, Vincent Mourik, Benjamin Joecker, Mark AI Johnson, Andrew D Baczewski, Hannes R Firgau, Mateusz T Mądzik, Vivien Schmitt, Jarryd J Pla, Fay E Hudson, et al. Coherent electrical control of a single high-spin nucleus in silicon. *Nature*, 579(7798):205–209, 2020.

[30] Rostyslav Savytskyy, Tim Botzem, Irene Fernandez de Fuentes, Benjamin Joecker, Fay E Hudson, Kohei M Itoh, Alexander M Jakob, Brett C Johnson, David N Jamieson, Andrew S Dzurak, et al. An electrically-driven single-atomflip-flop'qubit. *arXiv preprint arXiv:2202.04438*, 2022.

[31] Jian Leng, Fan Yang, and Xiang-Bin Wang. Nuclear electric resonance. *arXiv preprint arXiv:2111.01424*, 2021.

[32] Peter E Blöchl. First-principles calculations of defects in oxygen-deficient silica exposed to hydrogen. *Physical Review B*, 62(10):6158, 2000.

[33] John David Jackson. Classical electrodynamics, 1999.

[34] RV Pound. Nuclear electric quadrupole interactions in crystals. *Physical Review*, 79(4):685, 1950.

[35] Helena M Petrilli, Peter E Blöchl, Peter Blaha, and Karlheinz Schwarz. Electric-field-gradient calculations using the projector augmented wave method. *Physical Review B*, 57(23):14690, 1998.

[36] Mildred S Dresselhaus, Gene Dresselhaus, and Ado Jorio. *Group theory: application to the physics of condensed matter*. Springer Science & Business Media, 2007.

[37] Melvin A Ruderman and Charles Kittel. Indirect exchange coupling of nuclear magnetic moments by conduction electrons. *Physical Review*, 96(1):99, 1954.

[38] Tadao Kasuya. A theory of metallic ferro-and antiferromagnetism on zener's model. *Progress of theoretical physics*, 16(1):45–57, 1956.

[39] Kei Yosida. Magnetic properties of cu-mn alloys. *Physical Review*, 106(5):893, 1957.

[40] JH Van Vleck. Note on the interactions between the spins of magnetic ions or nuclei in metals. *Reviews of Modern Physics*, 34(4):681, 1962.

[41] Atsushi Goto, Shinobu Ohki, Kenjiro Hashi, and Tadashi Shimizu. Optical switching of nuclear spin–spin couplings in semiconductors. *Nature Communications*, 2(1):1–5, 2011.

[42] Atsushi Goto, Kenjiro Hashi, Shinobu Ohki, and Tadashi Shimizu. Optically induced nuclear spin–spin couplings in gaas manifested by spin echo decays under optical pumping. *npj Quantum Information*, 8(1):1–6, 2022.

[43] Anthony J Sigillito, Alexei M Tyryshkin, Thomas Schenkel, Andrew A Houck, and Stephen A Lyon. All-electric control of donor nuclear spin qubits in silicon. *Nature nanotechnology*, 12(10):958–962, 2017.

[44] Yuma Okazaki, Imran Mahboob, Koji Onomitsu, Satoshi Sasaki, Shuji Nakamura, Nobu-Hisa Kaneko, and Hiroshi Yamaguchi. Dynamical coupling between a nuclear spin ensemble and electromechanical phonons. *Nature communications*, 9(1):1–8, 2018.

[45] Smarak Maity, Benjamin Pingault, Graham Joe, Michelle Chalupnik, Daniel Assumpção, Eliza Cornell, Linbo Shao, and Marko Lončar. Mechanical control of a single nuclear spin. *Physical Review X*, 12(1):011056, 2022.

[46] Fedor Jelezko, T Gaebel, I Popa, M Domhan, A Gruber, and Jorg Wrachtrup. Observation of coherent oscillation of a single nuclear spin and realization of a two-qubit conditional quantum gate. *Physical Review Letters*, 93(13):130501, 2004.

[47] MV Gurudev Dutt, L Childress, L Jiang, E Togan, J Maze, F Jelezko, AS Zibrov, PR Hemmer, and MD Lukin. Quantum register based on individual electronic and nuclear spin qubits in diamond. *Science*, 316(5829):1312–1316, 2007.

[48] Jarryd J Pla, Kuan Y Tan, Juan P Dehollain, Wee H Lim, John JL Morton, Floris A Zwanenburg, David N Jamieson, Andrew S Dzurak, and Andrea Morello. High-fidelity readout and control of a nuclear spin qubit in silicon. *Nature*, 496(7445):334–338, 2013.

[49] Jarryd J Pla, Fahd A Mohiyaddin, Kuan Y Tan, Juan P Dehollain, Rajib Rahman, Gerhard Klimeck, David N Jamieson, Andrew S Dzurak, and Andrea Morello. Coherent control of a single si 29 nuclear spin qubit. *Physical review letters*, 113(24):246801, 2014.

[50] GD Fuchs, Guido Burkard, PV Klimov, and DD Awschalom. A quantum memory intrinsic to single nitrogen–vacancy centres in diamond. *Nature Physics*, 7(10):789–793, 2011.

[51] Paz London, J Scheuer, J-M Cai, I Schwarz, A Retzker, Martin B Plenio, M Katagiri, T Teraji, S Koizumi, J Isoya, et al. Detecting and polarizing nuclear spins with double resonance on a single electron spin. *Physical review letters*, 111(6):067601, 2013.

[52] V Jacques, P Neumann, J Beck, M Markham, D Twitchen, J Meijer, F Kaiser, G Balasubramanian, F Jelezko, and J Wrachtrup. Dynamic polarization of single nuclear spins by optical pumping of nitrogen-vacancy color centers in diamond at room temperature. *Physical review letters*, 102(5):057403, 2009.

[53] ML Goldman, TL Patti, D Levonian, SF Yelin, and MD Lukin. Optical control of a single nuclear spin in the solid state. *Physical Review Letters*, 124(15):153203, 2020.

[54] Yuttapoom Puttisong, XJ Wang, IA Buyanova, L Geelhaar, H Riechert, AJ Ptak, CW Tu, and WM Chen. Efficient room-temperature nuclear spin hyperpolarization of a defect atom in a semiconductor. *Nature communications*, 4(1):1–8, 2013.

[55] Sen Yang, Ya Wang, DD Rao, Thai Hien Tran, Ali S Momenzadeh, M Markham, DJ Twitchen, Ping Wang, Wen Yang, Rainer Stöhr, et al. High-fidelity transfer and storage of photon states in a single nuclear spin. *Nature Photonics*, 10(8):507–511, 2016.

[56] D Serrano, J Karlsson, A Fossati, A Ferrier, and P Goldner. All-optical control of long-lived nuclear spins in rare-earth doped nanoparticles. *Nature communications*, 9(1):1–7, 2018.

[57] Or Katz, Roy Shaham, and Ofer Firstenberg. Coupling light to a nuclear spin gas with a two-photon linewidth of five millihertz. *Science advances*, 7(14):eabe9164, 2021.

[58] SR Hartmann and EL Hahn. Nuclear double resonance in the rotating frame. *Physical Review*, 128(5):2042, 1962.

[59] A Henstra, P Dirksen, J Schmidt, and W Th Wenckebach. Nuclear spin orientation via electron spin locking (novel). *Journal of Magnetic Resonance (1969)*, 77(2):389–393, 1988.

[60] Eduard C Reynhardt and Grant L High. Dynamic nuclear polarization of diamond. ii. nuclear orientation via electron spin-locking. *The Journal of chemical physics*, 109(10):4100–4107, 1998.

[61] Jianming Cai, Fedor Jelezko, Martin B Plenio, and Alex Retzker. Diamond-based single-molecule magnetic resonance spectroscopy. *New Journal of Physics*, 15(1):013020, 2013.

[62] Ádám Gali. Ab initio theory of the nitrogen-vacancy center in diamond. *Nanophotonics*, 8(11):1907–1943, 2019.

[63] Wolfgang Kraut and Ralph von Baltz. Anomalous bulk photovoltaic effect in ferroelectrics: a quadratic response theory. *Physical Review B*, 19(3):1548, 1979.

[64] Ralph von Baltz and Wolfgang Kraut. Theory of the bulk photovoltaic effect in pure crystals. *Physical Review B*, 23(10):5590, 1981.

[65] Pierre Hohenberg and Walter Kohn. Inhomogeneous electron gas. *Physical review*, 136(3B):B864, 1964.

[66] Walter Kohn and Lu Jeu Sham. Self-consistent equations including exchange and correlation effects. *Physical review*, 140(4A):A1133, 1965.

[67] N Bloembergen. Linear stark effect in magnetic resonance spectra. *Science*, 133:1363, 1961.

[68] D Gill and N Bloembergen. Linear stark splitting of nuclear spin levels in gaas. *Physical Review*, 129(6):2398, 1963.

[69] RW Dixon and N Bloembergen. Electrically induced perturbations of halogen nuclear quadrupole interactions in polycrystalline compounds. i. phenomenological theory and experimental results. *The Journal of Chemical Physics*, 41(6):1720–1738, 1964.

[70] Masaaki Ono, Jun Ishihara, Genki Sato, Yuzo Ohno, and Hideo Ohno. Coherent manipulation of nuclear spins in semiconductors with an electric field. *Applied Physics Express*, 6(3):033002, 2013.

[71] Paolo Giannozzi, Stefano Baroni, Nicola Bonini, Matteo Calandra, Roberto Car, Carlo Cavazzoni, Davide Ceresoli, Guido L Chiarotti, Matteo Cococcioni, Ismaila Dabo, Andrea Dal Corso, Stefano de Gironcoli, Stefano Fabris, Guido Fratesi, Ralph Gebauer, Uwe Gerstmann, Christos Gougoussis, Anton Kokalj, Michele Lazzeri, Layla Martin-Samos, Nicola Marzari, Francesco Mauri, Riccardo Mazzarello, Stefano Paolini, Alfredo Pasquarello, Lorenzo Paulatto, Carlo Sbraccia, Sandro Scandolo, Gabriele Sclauzero, Ari P Seitsonen, Alexander Smogunov, Paolo Umari, and Renata M Wentzcovitch. Quantum espresso: a modular and open-source software project for quantum simulations of materials. *Journal of Physics: Condensed Matter*, 21(39):395502 (19pp), 2009.

[72] P Giannozzi, O Andreussi, T Brumme, O Bunau, M Buongiorno Nardelli, M Calandra, R Car, C Cavazzoni, D Ceresoli, M Cococcioni, N Colonna, I Carnimeo, A Dal Corso, S de Gironcoli, P Delugas, R A DiStasio Jr, A Ferretti,

A Floris, G Fratesi, G Fugallo, R Gebauer, U Gerstmann, F Giustino, T Gorni, J Jia, M Kawamura, H-Y Ko, A Kokalj, E Küçükbenli, M Lazzeri, M Marsili, N Marzari, F Mauri, N L Nguyen, H-V Nguyen, A Otero de-la Roza, L Paulatto, S Poncé, D Rocca, R Sabatini, B Santra, M Schlipf, A P Seitsonen, A Smogunov, I Timrov, T Thonhauser, P Umari, N Vast, X Wu, and S Baroni. Advanced capabilities for materials modelling with quantum espresso. *Journal of Physics: Condensed Matter*, 29(46):465901, 2017.

[73] John P Perdew, Kieron Burke, and Matthias Ernzerhof. Generalized gradient approximation made simple. *Physical review letters*, 77(18):3865, 1996.

[74] Peter E Blöchl. Projector augmented-wave method. *Physical review B*, 50(24):17953, 1994.

[75] RD King-Smith and David Vanderbilt. Theory of polarization of crystalline solids. *Physical Review B*, 47(3):1651, 1993.

[76] Raffaele Resta and David Vanderbilt. Theory of polarization: a modern approach. In *Physics of Ferroelectrics*, pages 31–68. Springer, 2007.

[77] Matthias Pfender, Nabeel Aslam, Patrick Simon, Denis Antonov, Gergo Thiering, Sina Burk, Felipe Fávaro de Oliveira, Andrej Denisenko, Helmut Fedder, Jan Meijer, et al. Protecting a diamond quantum memory by charge state control. *Nano letters*, 17(10):5931–5937, 2017.

[78] Viktor Ivády, Igor A Abrikosov, and Adam Gali. First principles calculation of spin-related quantities for point defect qubit research. *npj Computational Materials*, 4(1):1–13, 2018.

[79] T Holstein and Hl Primakoff. Field dependence of the intrinsic domain magnetization of a ferromagnet. *Physical Review*, 58(12):1098, 1940.

[80] Ryogo Kubo. The spin-wave theory of antiferromagnetics. *Physical Review*, 87(4):568, 1952.

[81] Sambhu N Datta and Anirban Panda. All-temperature magnon theory of ferromagnetism. *Journal of Physics: Condensed Matter*, 21(33):336003, 2009.

[82] Andrii V Chumak, Vitaliy I Vasyuchka, Alexander A Serga, and Burkard Hillebrands. Magnon spintronics. *Nature physics*, 11(6):453–461, 2015.

[83] HY Yuan, Yunshan Cao, Akashdeep Kamra, Rembert A Duine, and Peng Yan. Quantum magnonics: when magnon spintronics meets quantum information science. *Physics Reports*, 965:1–74, 2022.

[84] SM Rezende and RM White. Multimagnon theory of antiferromagnetic resonance relaxation. *Physical Review B*, 14(7):2939, 1976.

[85] SM Rezende and RM White. Spin-wave lifetimes in antiferromagnetic rbmn f 3. *Physical Review B*, 18(5):2346, 1978.

[86] Sergio M Rezende, Antonio Azevedo, and Roberto L Rodriguez-Suarez. Introduction to antiferromagnetic magnons. *Journal of Applied Physics*, 126(15):151101, 2019.

[87] Sergio M Rezende. *Fundamentals of magnonics*, volume 969. Springer, 2020.

[88] Tianli Feng, Lucas Lindsay, and Xiulin Ruan. Four-phonon scattering significantly reduces intrinsic thermal conductivity of solids. *Physical Review B*, 96(16):161201, 2017.

[89] Xiaolong Yang, Tianli Feng, Joon Sang Kang, Yongjie Hu, Ju Li, and Xiulin Ruan. Observation of strong higher-order lattice anharmonicity in raman and infrared spectra. *Physical Review B*, 101(16):161202, 2020.

[90] Joon Sang Kang, Man Li, Huan Wu, Huuduy Nguyen, and Yongjie Hu. Experimental observation of high thermal conductivity in boron arsenide. *Science*, 361(6402):575–578, 2018.

[91] Sheng Li, Qiye Zheng, Yinchuan Lv, Xiaoyuan Liu, Xiqu Wang, Pinshane Y Huang, David G Cahill, and Bing Lv. High thermal conductivity in cubic boron arsenide crystals. *Science*, 361(6402):579–581, 2018.

[92] Jürgen König and Fred Hucht. Newton series expansion of bosonic operator functions. *SciPost Physics*, 10(1):007, 2021.

[93] Philipp Neumann, Johannes Beck, Matthias Steiner, Florian Rempp, Helmut Fedder, Philip R Hemmer, Jörg Wrachtrup, and Fedor Jelezko. Single-shot readout of a single nuclear spin. *science*, 329(5991):542–544, 2010.

[94] A Meldrum, P Bianucci, and F Marsiglio. Modification of ensemble emission rates and luminescence spectra for inhomogeneously broadened distributions of quantum dots coupled to optical microcavities. *Optics express*, 18(10):10230–10246, 2010.

[95] Ivan S Grudinin, Andrey B Matsko, Anatoliy A Savchenkov, Dmitry Strekalov, Vladimir S Ilchenko, and Lute Maleki. Ultra high q crystalline microcavities. *Optics Communications*, 265(1):33–38, 2006.

[96] Vincent Huet, Alphonse Rasoloniaina, Pierre Guillemé, Philippe Rochard, Patrice Féron, Michel Mortier, A Levenson, Kamel Bencheikh, Alejandro Yacomotti, and Yannick Dumeige. Millisecond photon lifetime in a slow-light microcavity. *Physical review letters*, 116(13):133902, 2016.

[97] Hyeongrak Choi, Mikkel Heuck, and Dirk Englund. Self-similar nanocavity design with ultrasmall mode volume for single-photon nonlinearities. *Physical review letters*, 118(22):223605, 2017.

[98] Iman Esmaeil Zadeh, Johannes WN Los, Ronan BM Gourgues, Violette Steinmetz, Gabriele Bulgarini, Sergiy M Dobrovolskiy, Val Zwiller, and Sander N Dorenbos. Single-photon detectors combining high efficiency, high detection rates, and ultra-high timing resolution. *Apl Photonics*, 2(11):111301, 2017.

[99] VB Verma, Boris Korzh, Alexander B Walter, Adriana E Lita, Ryan M Briggs, Marco Colangelo, Yao Zhai, Emma E Wollman, Andrew D Beyer, Jason P Allmaras, et al. Single-photon detection in the mid-infrared up to 10 μ m wavelength using tungsten silicide superconducting nanowire detectors. *APL Photonics*, 6(5):056101, 2021.

[100] L Andrew Lyon, Christine D Keating, Audrey P Fox, Bonnie E Baker, Lin He, Sheila R Nicewarner, Shawn P Mulvaney, and Michael J Natan. Raman spectroscopy. *Analytical Chemistry*, 70(12):341–362, 1998.

[101] Xin Cong, Xue-Lu Liu, Miao-Ling Lin, and Ping-Heng Tan. Application of raman spectroscopy to probe fundamental properties of two-dimensional materials. *npj 2D Materials and Applications*, 4(1):1–12, 2020.

[102] WH Renninger, P Kharel, RO Behunin, and PT Rakich. Bulk crystalline optomechanics. *Nature Physics*, 14(6):601–607, 2018.

[103] RWP Drever, John L Hall, FV Kowalski, J_ Hough, GM Ford, AJ Munley, and H Ward. Laser phase and frequency stabilization using an optical resonator. *Applied Physics B*, 31(2):97–105, 1983.

[104] JL Hall. Stabilizing lasers for applications in quantum optics. In *Quantum Optics IV*, pages 273–284. Springer, 1986.

[105] Ch Salomon, D Hils, and JL Hall. Laser stabilization at the millihertz level. *JOSA B*, 5(8):1576–1587, 1988.

[106] Dominic Meiser, Jun Ye, DR Carlson, and MJ Holland. Prospects for a millihertz-linewidth laser. *Physical review letters*, 102(16):163601, 2009.

[107] Timothy Day, Eric K Gustafson, and Robert L Byer. Sub-hertz relative frequency stabilization of two-diode laser-pumped nd: Yag lasers locked to a fabry-perot interferometer. *IEEE Journal of Quantum Electronics*, 28(4):1106–1117, 1992.

[108] BC Young, FC Cruz, WM Itano, and JC Bergquist. Visible lasers with subhertz linewidths. *Physical Review Letters*, 82(19):3799, 1999.

[109] JM Taylor, CM Marcus, and MD Lukin. Long-lived memory for mesoscopic quantum bits. *Physical review letters*, 90(20):206803, 2003.

[110] DA Gangloff, Gabriel Ethier-Majcher, Constantin Lang, EV Denning, JH Bodey, DM Jackson, Edmund Clarke, Maxime Hugues, Claire Le Gall, and Mete Atatüre. Quantum interface of an electron and a nuclear ensemble. *Science*, 364(6435):62–66, 2019.

[111] Daniel M Jackson, Dorian A Gangloff, Jonathan H Bodey, Leon Zaporski, Clara Bachorz, Edmund Clarke, Maxime Hugues, Claire Le Gall, and Mete Atatüre. Quantum sensing of a coherent single spin excitation in a nuclear ensemble. *Nature Physics*, 17(5):585–590, 2021.

[112] Dorian A Gangloff, Leon Zaporski, Jonathan H Bodey, Clara Bachorz, Daniel M Jackson, Gabriel Éthier-Majcher, Constantin Lang, Edmund Clarke, Maxime Hugues, Claire Le Gall, et al. Witnessing quantum correlations in a nuclear ensemble via an electron spin qubit. *Nature Physics*, 17(11):1247–1253, 2021.

[113] S Probst, A Tkalčec, H Rotzinger, D Rieger, Jean-Michel Le Floch, Maxim Goryachev, ME Tobar, AV Ustinov, and PA Bushev. Three-dimensional cavity quantum electrodynamics with a rare-earth spin ensemble. *Physical Review B*, 90(10):100404, 2014.

[114] Hayato Goto, Satoshi Nakamura, and Kouichi Ichimura. Experimental determination of intracavity losses of monolithic fabry-perot cavities made of pr 3+: Y 2 sio 5. *Optics Express*, 18(23):23763–23775, 2010.

[115] DI Schuster, Andrew Addison Houck, JA Schreier, A Wallraff, JM Gambetta, A Blais, L Frunzio, J Majer, B Johnson, MH Devoret, et al. Resolving photon number states in a superconducting circuit. *Nature*, 445(7127):515–518, 2007.

[116] Jeremie J Viennot, Xizheng Ma, and Konrad W Lehnert. Phonon-number-sensitive electromechanics. *Physical review letters*, 121(18):183601, 2018.

[117] Patricio Arrangoiz-Arriola, E Alex Wollack, Zhaoyou Wang, Marek Pechal, Wentao Jiang, Timothy P McKenna, Jeremy D Witmer, Raphaël Van Laer, and Amir H Safavi-Naeini. Resolving the energy levels of a nanomechanical oscillator. *Nature*, 571(7766):537–540, 2019.

[118] Lucas R Sletten, Bradley A Moores, Jeremie J Viennot, and Konrad W Lehnert. Resolving phonon fock states in a multimode cavity with a double-slit qubit. *Physical Review X*, 9(2):021056, 2019.

[119] Ingrid Schuster, Alexander Kubanek, Andreas Fuhrmanek, Thomas Puppe, Pepijn WH Pinkse, Karim Murr, and Gerhard Rempe. Nonlinear spectroscopy of photons bound to one atom. *Nature Physics*, 4(5):382–385, 2008.

[120] Alexander Kubanek, Alexei Ourjoumtsev, Ingrid Schuster, Markus Koch, Pepijn WH Pinkse, Karim Murr, and Gerhard Rempe. Two-photon gateway in one-atom cavity quantum electrodynamics. *Physical Review Letters*, 101(20):203602, 2008.

[121] S Probst, H Rotzinger, S Wünsch, P Jung, M Jerger, M Siegel, AV Ustinov, and PA Bushev. Anisotropic rare-earth spin ensemble strongly coupled to a superconducting resonator. *Physical Review Letters*, 110(15):157001, 2013.

[122] MJ Collett and CW Gardiner. Squeezing of intracavity and traveling-wave light fields produced in parametric amplification. *Physical Review A*, 30(3):1386, 1984.

[123] Lewis A Williamson, Yu-Hui Chen, and Jevon J Longdell. Magneto-optic modulator with unit quantum efficiency. *Physical review letters*, 113(20):203601, 2014.

[124] Yarema Reshitnyk, Markus Jerger, and Arkady Fedorov. 3d microwave cavity with magnetic flux control and enhanced quality factor. *EPJ Quantum Technology*, 3(1):1–6, 2016.

[125] Changhao Li and Paola Cappellaro. Telecom photon interface of solid-state quantum nodes. *Journal of Physics Communications*, 3(9):095016, 2019.

[126] Christopher O'Brien, Nikolai Lauk, Susanne Blum, Giovanna Morigi, and Michael Fleischhauer. Interfacing superconducting qubits and telecom photons via a rare-earth-doped crystal. *Physical review letters*, 113(6):063603, 2014.

[127] John C Wheatley, OE Vilches, and WR Abel. Principles and methods of dilution refrigeration. *Physics Physique Fizika*, 4(1):1, 1968.

[128] Theodor W Hänsch and Arthur L Schawlow. Cooling of gases by laser radiation. *Optics Communications*, 13(1):68–69, 1975.

[129] David J Wineland, Robert E Drullinger, and Fred L Walls. Radiation-pressure cooling of bound resonant absorbers. *Physical Review Letters*, 40(25):1639, 1978.

[130] Harold J Metcalf and Peter Van der Straten. Laser cooling and trapping of neutral atoms. *The Optics Encyclopedia: Basic Foundations and Practical Applications*, 2007.

[131] Markus Aspelmeyer, Tobias J Kippenberg, and Florian Marquardt. Cavity optomechanics. *Reviews of Modern Physics*, 86(4):1391, 2014.

[132] Mansoor Sheik-Bahae and Richard I Epstein. Can laser light cool semiconductors? *Physical review letters*, 92(24):247403, 2004.

[133] Sanchar Sharma, Yaroslav M Blanter, and Gerrit EW Bauer. Optical cooling of magnons. *Physical review letters*, 121(8):087205, 2018.

[134] Sanchar Sharma, Yaroslav M Blanter, and Gerrit EW Bauer. Light scattering by magnons in whispering gallery mode cavities. *Physical Review B*, 96(9):094412, 2017.

[135] Jens M Dobrindt, I Wilson-Rae, and Tobias J Kippenberg. Parametric normal-mode splitting in cavity optomechanics. *Physical Review Letters*, 101(26):263602, 2008.

[136] I Wilson-Rae, N Nooshi, Jens Dobrindt, Tobias J Kippenberg, and W Zwerger. Cavity-assisted backaction cooling of mechanical resonators. *New Journal of Physics*, 10(9):095007, 2008.

[137] P Rabl, C Genes, K Hammerer, and M Aspelmeyer. Phase-noise induced limitations on cooling and coherent evolution in optomechanical systems. *Physical Review A*, 80(6):063819, 2009.

[138] Yong-Chun Liu, Yun-Feng Xiao, Xingsheng Luan, and Chee Wei Wong. Dynamic dissipative cooling of a mechanical resonator in strong coupling optomechanics. *Physical review letters*, 110(15):153606, 2013.

[139] J Burris and TJ McIlrath. Theoretical study relating the two-photon absorption cross section to the susceptibility controlling four-wave mixing. *JOSA B*, 2(8):1313–1317, 1985.

[140] Joel M Hales, San-Hui Chi, Taylor Allen, Sepehr Benis, Natalia Munera, Joseph W Perry, Dale McMorrow, David J Hagan, and Eric W Van Stryland. Third-order nonlinear optical coefficients of si and gaas in the near-infrared spectral region. In *CLEO: Science and Innovations*, pages JTu2A–59. Optical Society of America, 2018.

[141] Michael M Choy and Robert L Byer. Accurate second-order susceptibility measurements of visible and infrared nonlinear crystals. *Physical Review B*, 14(4):1693, 1976.

[142] Yuen-Ron Shen. Principles of nonlinear optics. 1984.

[143] Govind P Agrawal and Robert W Boyd. Contemporary nonlinear optics. *Contemporary Nonlinear Optics*, 1992.

[144] Robert W Boyd. *Nonlinear optics*. Academic press, 2020.

[145] Davorin Peceli, Peter D Olszak, Claudiu M Cirloganu, Scott Webster, Lazaro A Padilha, Trenton Ensley, Honghua Hu, Gero Nootz, David J Hagan, and Eric W Van Stryland. Three-photon absorption of gaas and other semiconductors. In *Nonlinear Optics*, pages NTu1B–6. Optica Publishing Group, 2013.

[146] M. S. Dresselhaus. Solid state physics part ii optical properties of solids.

[147] Liang Z Tan, Fan Zheng, Steve M Young, Fenggong Wang, Shi Liu, and Andrew M Rappe. Shift current bulk photovoltaic effect in polar materials-hybrid and oxide perovskites and beyond. *Npj Computational Materials*, 2(1):1–12, 2016.

[148] SY Yang, Jan Seidel, SJ Byrnes, P Shafer, C-H Yang, MD Rossell, P Yu, Y-H Chu, JF Scott, JW Ager, et al. Above-bandgap voltages from ferroelectric photovoltaic devices. *Nature nanotechnology*, 5(2):143–147, 2010.

[149] Charles Kittel. Introduction to solid state physics eighth edition. 2021.

[150] Kurt Binder and A Peter Young. Spin glasses: Experimental facts, theoretical concepts, and open questions. *Reviews of Modern physics*, 58(4):801, 1986.

[151] Anders W Sandvik. Ground states of a frustrated quantum spin chain with long-range interactions. *Physical Review Letters*, 104(13):137204, 2010.

[152] C-L Hung, Alejandro González-Tudela, J Ignacio Cirac, and HJ Kimble. Quantum spin dynamics with pairwise-tunable, long-range interactions. *Proceedings of the National Academy of Sciences*, 113(34):E4946–E4955, 2016.

[153] Lars Onsager. Crystal statistics. i. a two-dimensional model with an order-disorder transition. *Physical Review*, 65(3-4):117, 1944.

[154] Chen Ning Yang. The spontaneous magnetization of a two-dimensional ising model. *Physical Review*, 85(5):808, 1952.

[155] Christian Holm and Wolfhard Janke. Critical exponents of the classical three-dimensional heisenberg model: A single-cluster monte carlo study. *Physical Review B*, 48(2):936, 1993.

[156] Audrey Bienfait, Kevin J Satzinger, YP Zhong, H-S Chang, M-H Chou, Chris R Conner, É Dumur, Joel Grebel, Gregory A Peairs, Rhys G Povey, et al. Phonon-mediated quantum state transfer and remote qubit entanglement. *Science*, 364(6438):368–371, 2019.

[157] D Andrew Golter, Thein Oo, Mayra Amezcua, Ignas Lekavicius, Kevin A Stewart, and Hailin Wang. Coupling a surface acoustic wave to an electron spin in diamond via a dark state. *Physical Review X*, 6(4):041060, 2016.

[158] Martin V Gustafsson, Thomas Aref, Anton Frisk Kockum, Maria K Ekström, Göran Johansson, and Per Delsing. Propagating phonons coupled to an artificial atom. *Science*, 346(6206):207–211, 2014.

[159] Samuel J Whiteley, Gary Wolfowicz, Christopher P Anderson, Alexandre Bourassa, He Ma, Meng Ye, Gerwin Koolstra, Kevin J Satzinger, Martin V Holt, F Joseph Heremans, et al. Spin–phonon interactions in silicon carbide addressed by gaussian acoustics. *Nature Physics*, 15(5):490–495, 2019.

[160] Peiyao Zhang, Ting-Fung Chung, Quanwei Li, Siqi Wang, Qingjun Wang, Warren LB Huey, Sui Yang, Joshua E Goldberger, Jie Yao, and Xiang Zhang. All-optical switching of magnetization in atomically thin cri3. *Nature Materials*, pages 1–6, 2022.